Radio Sources in the COSMOS Field

Star Forming Properties of High Luminosity Radio Galaxies

Emer Brady

Supervisors:
Dr. Eva Schinnerer (MPIA, Heidelberg)
Dr. Brent Groves (ANU, Canberra)

Errata

This version of the thesis differs from that submitted to the Faculty of Natural Sciences and Mathematics on Septenber 26th 2016. Some minor typographic errors have been corrected, as well as two missing references added in Chapter 3. In Section 3.2.2 the values of the ROBUST parameter were incorrectly stated and have been changed.

Dissertation
submitted to the
Combined Faculties of Natural Sciences and Mathematics
of the Ruperto-Carola-University of Heidelberg, Germany
for the degree of
Doctor of Natural Sciences

Put forward by
Emer Brady
born in: Drogheda, Ireland.
Oral examination: 10th of November 2016

Radio Sources in the COSMOS Field

Referees:
Prof. Dr. Hans-Walter Rix (MPIA, Heidelberg)
Dr. Simon C. O. Glover (ITA, Heidelberg)

"He was determined to discover the underlying logic behind the universe. Which was going to be hard, because there wasn't one."

Terry Pratchett, Mort.

Radio wavelengths offer a dust-unobscured window to the early universe. The aim of this thesis has been to characterize the star-forming properties of the high redshift radio galaxy population. We present a preliminary catalogue of the first 610 MHz map of the COSMOS field and find that the sample properties are consistent with predictions for the low frequency radio population. Furthermore, we compare radio and IR star formation rate (SFR) tracers on a large sample of starburst galaxies and find that locally calibrated infrared (IR) and 1.4 GHz radio continuum SFR tracers produce inconsistent results for the most active starbursts. These starbursts are rare locally, but become increasingly common in the early universe. The high redshift starburst population may be more extended, and hence cooler, than local counterparts. In addition, the infrared-radio correlation, observed thus far to be linear and constant for a wide range of galaxies, may exhibit redshift or luminosity evolution. We conclude that a dedicated effort to better model the IR and radio spectral energy distributions of starbursts will be essential to accurately characterize the SFR density at higher redhifts than those considered by studies to date.

Radiowellen bieten ein Fenster in das frühe Universum, das nicht von Staub verdunkelt wird. Das Ziel dieser Arbeit war eine Charakterisierung der Sternentstehungseigenschaften der Population von Radiogalaxien bei hoher Rotverschiebung. Wir stellen einen vorläufigen Katalog der ersten 610 MHz Karte des COSMOS Feldes vor und finden, dass die Eigenschaften des Samples konsistent sind mit Vorhersagen für die Radiopopulation bei niedrigen Frequenzen. Des Weiteren vergleichen wir Indikatoren (Tracer) von Sternentstehungsraten (SFR) im Radiobereich und im Infraroten (IR) bei einem umfangreichen Sample von Starburstgalaxien und stellen fest, dass lokal kalibrierte Infrarot- und 1.4 GHz Radiokontinuumstracer der SFR inkonsistente Ergebnisse für die aktivsten Starbursts liefern. Diese Starbursts sind lokal selten, aber werden zunehmend häufig im frühen Universum. Die Starburstpopulation bei hoher Rotverschiebung ist vermutlich diffuser, und daher kälter, als lokale Gegenstücke. Zusätzlich dürfte die Infrarot-Radio-Korrelation, bisher als linear und konstant für eine groe Auswahl an Galaxien beobachtet, eine Evolution mit Rotverschiebung z oder Leuchtkraft aufweisen. Wir kommen zu dem Schluss, dass eine größere Anstrengung erforderlich ist, die spektralen Energieverteilungen von Starbursts im IR und Radio besser zu modellieren, um die SFR-Dichte bei höherer Rotverschiebung, als bislang von Studien berücksichtigt, genau zu charakterisieren.

Contents

Chapter 1

Introduction

In 1925 Edwin Hubble demonstrated that 'nebulae' were extragalactic in origin and in fact galaxies just like our own. In 1929 he discovered that galaxies were receeding away from the Milky Way at a rate proportional to their distance from it ('Hubbles Law'). Ever since these paradigm-shifting discoveries, galaxies have been a key tool for astronomers attempting to understand the cosmos. The formation of galaxies is strongly influenced by the matter and energy content of the universe. The large scale structure of the universe (the so-called 'Cosmic Web'), revealed through deep wide-field redshift surveys of galaxies (Figure 1.1), traces the distribution of the initial density perturbations seeded during the Big Bang[1]. Studies of galaxies on cosmic timescales therefore provide key insights into the formation of the largest scale structures in the Universe ($\sim$100 Mpc today) and hence constrain cosmological parameters and give insights into the nature of dark matter as well as the baryonic physics governing the formation of visible structure.

After inflation ended the evolution of the Universe proceeds according to the well known rules of general relativity, within the 'ΛCDM' framework, whereby the universe's energy-matter content is comprised of four components; radiation (including neutrinos), baryonic matter, dark matter and dark energy[2] which

[1] Our current best understanding of the workings and evolution of the Universe have it starting some 13.7 Gyr ago with a period of exponential expansion, dubbed 'inflation' whose broad effects were two fold; ensuring the current day universe is flat, isotropic and homogeneous on large scales (the 'cosmological principle') and freezing in quantum fluctuations in the initial inflation field. These became the sites of the inital dark matter density perturbations that accreted baryonic matter to form the galaxies and galaxy clusters we observe today

[2] In ΛCDM dark energy is treated as a cosmological constant (its energy density remaining fixed) and dark matter has no elecromagnetic interactions and is cold and pressureless.

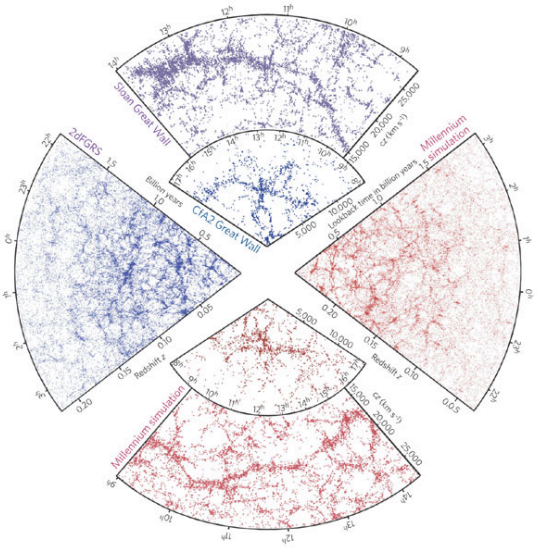

FIGURE 1.1: The redshift distribution of galaxies in the local volume. We clearly disinguish the large scale structure (LSS), or 'Cosmic Web' . The blue cone on the left shows the observations from the 2dFGRS, which includes more than 220,000 galaxies out to a distance of 2 billion light years in the southern sky, the purple cone the the SDSS surevy of 650,000 galaxies in the northern sky. The red cones are the mock catalogues constructed from the Millenium cosmological simulation. This figure is taken from Springel et al. (2006).

evolve differently. The current contributions of the four components to the energy budget are ≈0%, 5%, 26% and 96% respectively (Ade et al., 2015). The timeline of the 'ΛCDM' universe is summarized[3] in Figure 1.2. Approximately 300,000 yrs (z ≈1100) after inflation ended it had expanded and cooled down enough (T∼3000 K) to allow for protons and electrons to recombine and produce neutral hydrogen[4]. The photons which 'decoupled' then are today detected as the the 2.7 K cosmic microwave background (CMB) - temperature fluctuations in the CMB trace the distribution of matter density perturbations at that epoch. Once baryons and photons had decoupled, the baryons were free to fall into the dark matter gravitational potential wells, cool, condense and start to form stars and galaxies (White & Rees, 1978). At about 100 Myr (z ∼30) after the Big Bang the 'Dark Ages' ended when the first stars ignited, it then took around another 250 Myr for the stars to become numerous and distributed enough to appreciably heat their surrounding interstellar medium (from 100 K to 1000 K), ionizing hydrogen. The ionized hydrogen bubbles grew and overlapped until at about 800 Myr (z ∼7)

[3]We refer the reader to any cosmology textbook, such as Peacock (1999) for a more detailed summary.

[4]The baryon mass content of the universe is 73 % H and 23 %He, with the heavier elements making up the remaining 2 %.

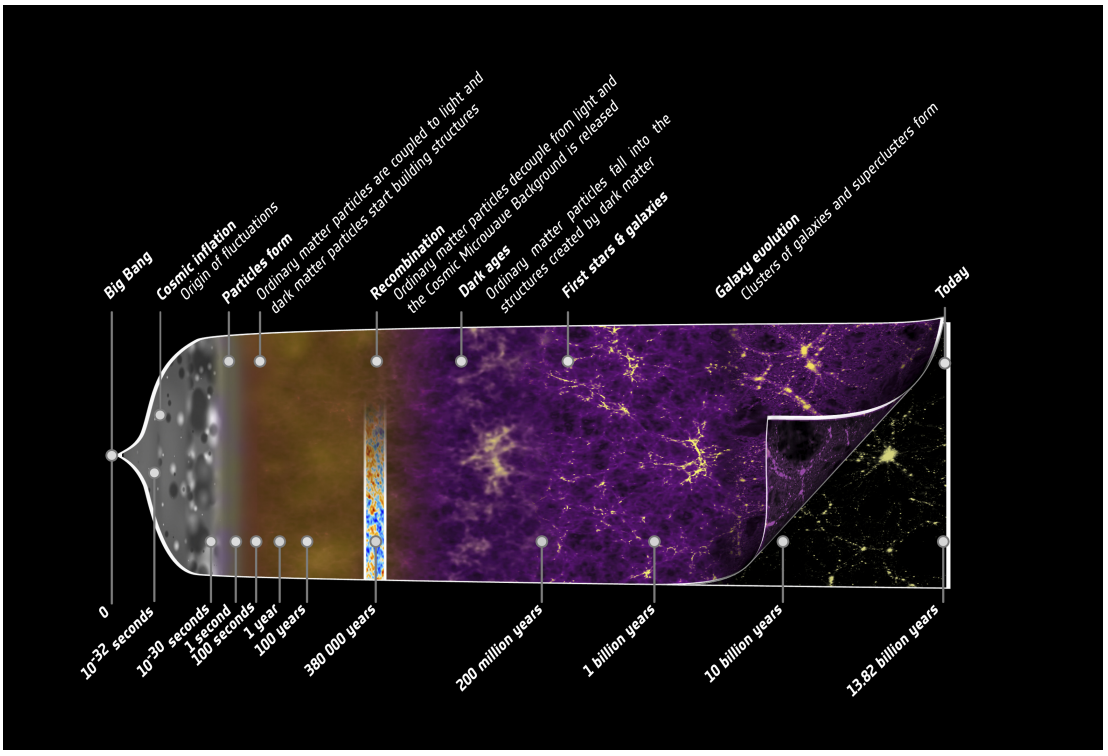

FIGURE 1.2: The timeline of the universe. Courtesy of the European Space Agency.

the Universe was once again reionized. The first galaxies formed in this epoch, including the most distant observed (spectroscopically confirmed) object to date at z=11.1 (Oesch et al., 2016), were assembled just ∼400 Myr after the Big Bang. At 1 Gyr (z ∼6) the Universe had cooled to about 19 K and the first galaxy proto-clusters started to form, with the first clusters appearing at around 3 Gyr (z ∼2) and superclusters[5] at 5 Gyr (z ∼1). At 10 Gyr (z ∼0.5), dark energy started to dominate the total energy budget of the universe and triggered the epoch of accelerated expansion, which continues to this day (13.7 Gyr, z =0 and T=2.7 K).

This picture is far from complete; we still have very little understanding of the make-up of dark-matter which is observed to interact only gravitationally, and even less so of dark energy (the vacuum energy driving the current accelerated expansion phase of the universe), not to mention an incomplete understanding of the baryonic processes which we *can* directly observe. Although ΛCDM is the current favored paradigm, it is still only one of many possible cosmological models. The dark matter distribution can be modelled with high accuracy (e.g most famously perhaps by Springel et al., 2005) but the baryonic physics proves much more complex - incorporating hydrodynamics, radiative transfer and star

[5]Groups of galaxy clusters.

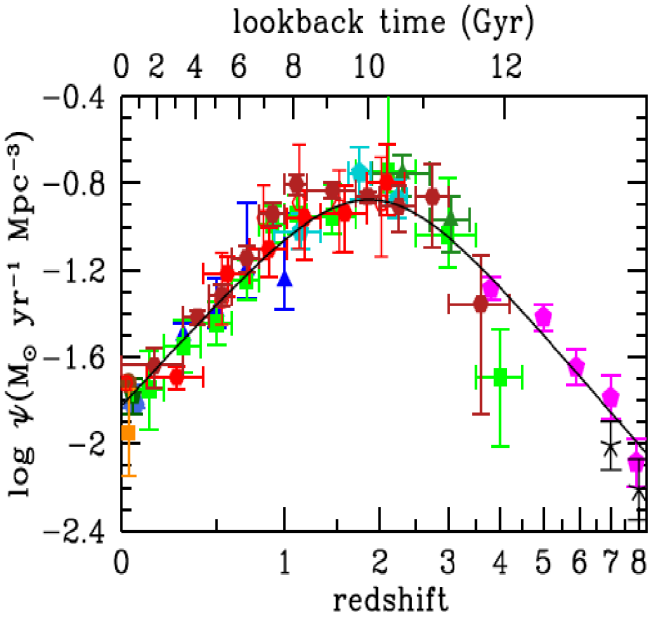

FIGURE 1.3: The cosmic SFRD from the review paper of Madau & Dickinson (2014) - we refer the reader to this paper for the full list of references and background on the datapoints presented here. The pentagons, triangles and the green squares are UV datapoints (corrected for dust attenuation), the dark orange squares and hexagons are IR measurements. Note the sparse coverage beyond the peak and the disagreements between the different surveys.

formation feedback and chemical enrichment models of the interstellar medium, to name but a few.

Measuring the rate of stellar mass build-up in galaxies over cosmic times in deep wide-field surveys (so as to counteract the effects of cosmic variance and have a statistically meaningful sample) is crucial to the understanding of the underlying processes governing galaxy formation and evolution. Hence a key tool of galactic astronomers and cosmologists is the star formation rate density (SFRD) - the rate at which stellar mass is built up per unit co-moving volume of the universe. Lilly et al. (1996) presented the first studies of the SFRD, finding that it had declined exponentially since z∼1 and since then there have been many follow-up studies at different wavelengths (see Madau & Dickinson (2014) for an overview and Figure 1.3). Many open questions remain, which these studies can offer insight into. A by-no-means-comprehensive list includes: At what epoch (if any one in particular) were most of the heavy elements and stellar mass formed? How does the rate of stellar mass build-up in a galaxy depend on environment, morphology and/or mass? Does the black hole accretion history mirror that of the star formation history? And how much of a role (if any) do supermassive black holes, or

active galactic nuclei (AGN), play in regulating star-formation via feedback and quenching? Accurate calibrations of SFR tracers at multiple wavelengths are an essential component to such studies. Although the deepest measurements available to date are generally at ultra-violet (UV) wavelengths, dust obscuration in massive actively star-forming galaxies which are increasingly common at higher redshifts and contribute significantly to the SFRD, means that these wavebands are generally highly extincted and UV-based SFRs can underestimate the true rate of star formation. Radio and infrared (IR) SFR tracers are thus essential tools for probing the star-forming history of the early universe. They have been calibrated and extensively tested on local populations of normal star-forming galaxies and it is now important to determine how well they perform on more extreme galaxies at high redshifts (Chapter 2.3).

1.1 The Evolving Galaxy Population

It is widely accepted that galaxies formed via a hierarchical 'bottom up' approach, whereby dark matter overdensities grow via gravitational instability (Peebles & Turner, 1992). Later, after photons have decoupled from baryons, they are free to fall into the potential wells of the dark matter halos, cool and form stars. Halos merge to form incereasingly more massive systems, from ultra-faint dwarf galaxies ($M_* < 10^5 \mathrm{M}_\odot$) to massive ellipticals ($M_* \sim 5 \times 10^{11} \mathrm{M}_\odot$). These galaxies group together in gravitationally bound clusters, which then arrange themselves into galaxy superclusters (which are gravitationally unbound) - the largest structures in the universe. The early universe supported much more extreme star-forming environments than today; the interstellar medium (ISM) of a typical star forming galaxy was hotter and more gas and dust enriched.

Locally, galaxy populations have been observed to be mass-divided (with the dividing stellar mass being $\sim 3 \times 10^{10}\,\mathrm{M}_\odot$) into two populations associated with distinct morphological types and exhibiting differing colors, surface mass densities and concentration trends (Kauffmann et al., 2003). The low mass population consists of the spiral (disk, or late-type) galaxies which are faint, have blue optical colors, are starforming and are rotationally supported. The higher mass galaxy population - massive ellipticals (or early-type) - are bright, red, passive (in that they show very little current star formation) and pressure supported. Figure 1.4

illustrates this bimodality. Although most of the mass of a disk galaxy is contained in the older stars, the light output of late-type galaxies is dominated by the massive young UV luminous population which is responsible for their blue optical colors[6]. In contrast, elliptical galaxies have ceased to form stars and the stellar poulations are considerably older than in the disk galaxies. Many of the elliptical galaxies have been observed to have assembled most of their stellar mass before $z = 2$. The red galaxy population has increased (in number and total stellar mass) with time since the peak of cosmic SF ($z \sim 1$), whereas the blue population has remained roughly constant (Faber et al., 2007) indicating that red passive galaxies are the end stage of the (blue) galaxy evolutionary path. The quenching of star formation in a galaxy can proceed via two channels (Schawinski et al., 2014); a major merger of two late-type galaxies which results in a rapid transition (over a few 100 Myr) from the blue to the red cloud, or the cut-off of gas inflow to a galaxy (e.g winds powered by an AGN can prevent gas inflow) whereby the galaxy continues to form stars for several Gyr until it depletes its gas supply. In the first scenario a massive elliptical galaxy is formed - its gas reservoir is destroyed either by a burst of enhanced star formation or AGN feedback processes. In the second scenario, the galaxy retains its late type morphology - a non-negligible fraction of the passive galaxies are disks (our own Milky Way is in fact a quiescent spiral galaxy).

This bimodal picture, with blue sequence galaxies following an evolutionary path that terminates in the red sequence (Figure 1.4) holds broadly true in the local universe and also at higher redshifts. Galaxies on these two sequences come in many varieties and there is a profusion of terminology in the literature grouping them in terms of their masses, star formation rates, brightness in certain bands etc. In this work the LIRG (luminous IR galaxy) and ULIRG (ultra-luminous IR galaxy), referring to galaxies with bolometric IR luminosities of $10^{11}\,\mathrm{L}_{\odot} < L_{TIR} < 10^{12}\,\mathrm{L}_{\odot}$ and $L_{TIR} \geq 10^{12}\,\mathrm{L}_{\odot}$ respectively, are perhaps the most relevant terms, as is AGN (active galactic nuclei). Nearly all galaxies host a central supermassive black hole whose evolutionary path and growth is tightly linked to that of its host galaxy (Heckman & Best, 2014). When emission from the central region of the galaxy (the accretion disk surrounding the black hole) overwhelms that coming from the rest of the galaxy, we refer to it as an AGN. AGNs are amongst the

[6]Dust absorbs at UV wavelengths and re-emits in the IR; since starforming regions are dust as well as gas rich, actively star-forming galaxies (particularly in the early universe when starforming conditions were much more extreme) can be artificially reddened.

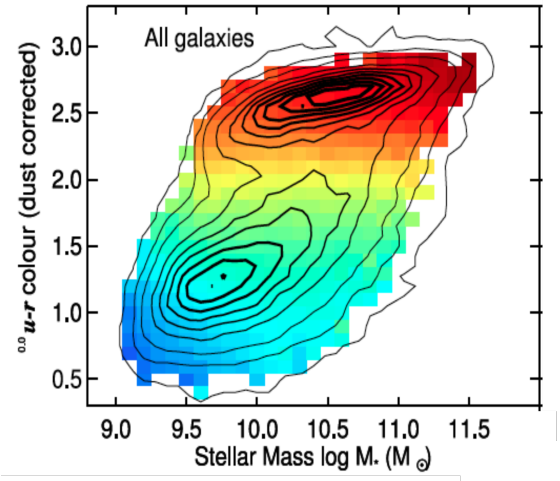

FIGURE 1.4: The dust-attenuation corrected color-mass diagram of Schawinski et al. (2014) for a local sample of galaxies. The cells are colored by the average specific SFR (sSFR=SFR/M_*). Larger values of u-r denote redder galaxies. The early-type galaxies are concentrated at the top of the panel and they tend to have higher stellar masses, redder colors and lower sSFR than the blue cloud galaxies, which are concentrated in the bottom left corner.

most luminous objects known, outshining normal star formation in galaxies by many orders of magnitude. The exact nature of the triggering of an AGN is still open to debate, as are their effects on the star formation in the host galaxy. In addition many AGNs are not detected at multiple wavelengths and the physical mechanisms responsible for this are still not fully understood[7].

1.1.1 The Star Forming Main Sequence

Star formation in most galaxies seems to follow simple (empirical) scaling laws such as the Kennicutt-Schmidt law (Kennicutt, 1998), which relates the SFR per unit surface area of a galaxy to the total (atomic plus molecular) gas mass surface density, indicating that stable secular processes such as gas infall and accretion are responsible for star formation. The scaling law of most interest to this thesis is the so called 'main sequence of star formation' (MS). The MS (Figure 1.5) is a tight empirical relation between the SFR and stellar mass (M_*) of a galaxy with a dispersion of 0.3 dex at z <1.3 (Noeske et al., 2007; Elbaz et al., 2007; Daddi et al.,

[7]The current favoured explanation, the 'unified model' of Urry & Padovani (1995) is that this is purely an observational effect - the AGN orientation relative to the observers line of sight is responsible for whether we see an IR, optical radio or X-ray AGN. For example if we view it edge on we see only the host dust torus, hence an IR AGN, at a more oblique angle we see an optical AGN and so on.

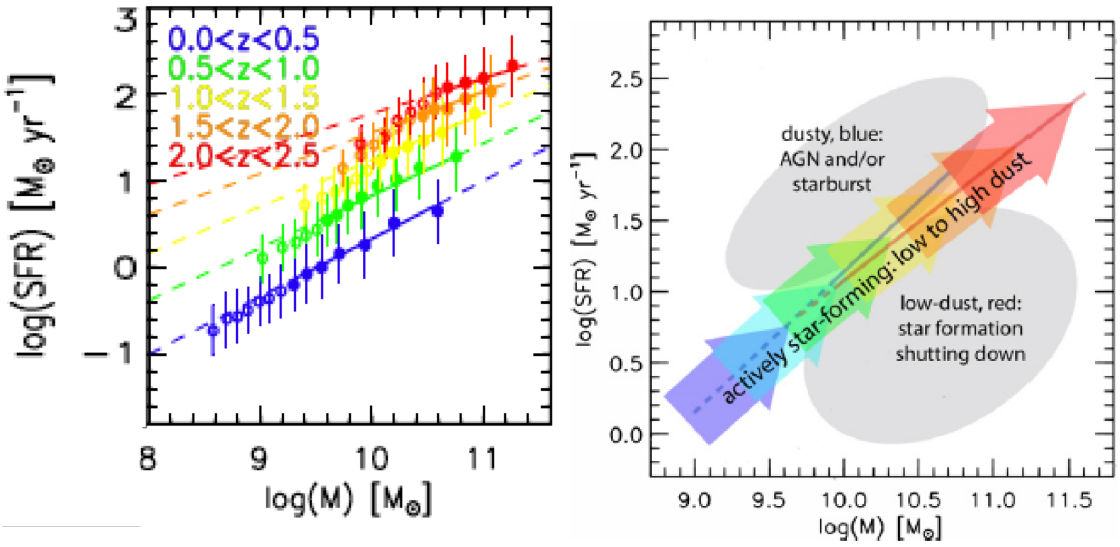

FIGURE 1.5: The main sequence of star formation from Whitaker et al. (2012). SFR vs. M_* in redshift bins of width Δz=0.5 is presented in the left panel. In the right panel a schematic diagram of how galaxies populate the log(SFR) - log(M_*) plane at any given redshift is presented.

2007; Magdis et al., 2010). It has been observed to hold out to $z \sim$7. It allows one to define a characteristic specific star formation rate (sSFR=SFR/M_*) at every epoch, with the sSFR increasing[8] from the present day out to $z \sim$2.5 (Karim et al., 2011; Whitaker et al., 2012), indicating that galaxies were more efficient at forming stars in the past. Beyond $z \sim$3 some studies have seen evidence for nearly constant sSFR (Stark et al., 2009; González et al., 2010), which could be due to observational biases, SFR tracers calibration issues, or could be indicating that there is a star-forming efficiency threshold which these galaxies have reached. In addition, the sSFR at fixed z is a declining function of M_*, which implies more massive galaxies are less efficient at forming stars. Elbaz et al. (2011) has shown out to $z \sim$2.5 that galaxies lying on this SFR $-$ M$_*$ main sequence also fall on an 'IR main sequence', that is they exhibit a constant linear slope in the $L_{8\mu m} - L_{TIR}$ relation, indicating the existence of a universal IR spectral energy distribution (SED) for main sequence star-forming galaxies that does not evolved over cosmic times (we refer the reader to Section 2.5.1 for more detail).

[8]The early universe was more gas rich and normal star formation could proceed at rates much higher than in the gas depleted galaxies in the local volume. SFR of $\sim$100s $M_\odot yr^{-1}$ were not uncommon (Daddi et al., 2005; Gruppioni et al., 2013).

1.1.1.1 Stellar Mass Build-up and the Peak of Cosmic Star Formation

Observational evidence (for example see the meta-analysis of different SFRD by Madau & Dickinson (2014) and references therein and Figure 1.3) now widely supports the idea that the SFRD peaked around z=1.9 and then declined exponentially over the 10 Gyr between then and the present day. Studies of the sSFR and its dependence on z and M_* indicate that the exponential decline in the global SFRD since z ∼2 is owing to a reduction in the cold molecular gas available for star formation (Karim et al., 2011). About 25 % of the stellar mass in the universe was formed before the peak of cosmic SFRD and a further 25 % from z =0.7 to the present day, meaning that around half of the stellar mass in the universe was assembled in and around the peak of the cosmic SFRD.

The galaxies that contribute most to the SFRD from z =0 to z ∼3 have masses of $10^{10.6\pm0.4}$M$_\odot$ (Karim et al., 2011), meaning that most of the stellar mass in the universe was assembled in normal main sequence galaxies of Milky Way mass (but of (U)LIRG IR luminosities). Since most of cosmic star formation took place in main sequence galaxies, it points to the cosmic star formation history being determined by a balance between gas accretion and feedback processes (related to galaxy mass) and that stochastic processes like mergers played a minor role.

1.1.1.2 The Star-Bursting Population

At every epoch a population of outliers above the SFR-M_* main sequence, dubbed starbursts, has been observed (e.g see the right-hand panel of Figure 1.5). These galaxies are undergoing a period of enhanced star formation, typically having SFRs ten times higher than would be expected from their projected mass densities (Daddi et al., 2010; Genzel et al., 2010). These starburst periods are transient, lasting only 100s Myr. Certainly locally, such star forming efficiency is only achieved in the extreme conditions of a gas rich (or major) merger of two galaxies - where star formation is concentrated in regions much more compact than in a normal main sequence galaxy. At higher z (∼2.5) many starburst galaxies may also be compact major mergers as evidenced by the correlation between distance off MS and the compactness of the star forming regions seen by Elbaz et al. (2011).

Starburst galaxies populate the high end of the IR and radio star-forming luminosity functions. Although they are not a major contributor to the SFRD (at

most 10-20% at the peak; Rodighiero et al. (2011); Gruppioni et al. (2013)), we cannot discount the fact that they may play a larger role at higher redshifts[9], in the denser environment of the early universe galaxy mergers are much more likely. Therefore extreme starbursts may be useful as tracers of protoclusters which are the progenitors of the most massive galaxy clusters we see in the present day universe. They may also be the best explanation of the rapid early assembly of mass (before $z \sim 2$) in the most massive quiescent galaxies observed today. In the local universe starbursts are rare, being LIRGs and ULIRGs. At higher redshifts ($z > 1$) (U)LIRGs are much more common and the majority will lie on the main sequence, that is be normal star forming galaxies - this is at the heart of why local IR SEDs for high luminosity galaxies are poor models of galaxies of similar IR luminosities at higher redshifts. So far it has been difficult to associate the high redshift starburst population with a particular class of galaxy, although a significant fraction of galaxies detected at sub-mm wavelengths (SMGs) tend to be in a starburst phase (see Lacki & Thompson (2010) and references therein). SMGs have been detected in large numbers out to $z = 6.3$ further suggesting that starbursts may play a more important role in the early universe than in the present. SMGs are also generally observed to be more extended or 'puffy' than local starbursting ULIRGs, with cosmic-ray disk scale heights of 1kpc as opposed to the 0.1kpc typically seen in local ULIRGs.

1.2 The Radio Galaxy Population

Although most of the deepest extragalactic observations to date have been conducted at UV and optical wavlengths, these regimes suffer from dust attenuation. Dust in the ISM will preferentially absorb light at UV wavelengths and re-emit in the IR. This is is a problem in particular in very actively star-forming galaxies in the early universe, where dust obscuration is high and up to 90 % of the UV/optical emission from young stars can be attenuated (Buat et al., 2005). Although methods are available to correct for this attenuation, they are usually calibrated on local, less dusty galaxies. It is therefore preferable to use dust-unaffected tracers, such as the IR and radio, to study high redshift actively star-forming galaxies.

[9]When considering SFR$>1000 M_{\odot} yr^{-1}$ sources only, which is not far above the limit that direct detections in many radio and IR surveys reach, they contribute at a level of 46 % or more to the SFRD. And, as covered in Section 1.1, the starburst phase (due to a merger) of a galaxy may be associated with its rapid transition from the blue cloud of star forming disks to the red cloud of passive ellipticals.

Radio observations are preferable over IR, given that they have higher resolutions and the surveys are often deeper. Another major advantage from the theoretical side, is that the radio SED takes a much simpler form than the IR, meaning that extrapolating for rest-frame radio luminosties from an observed band such as 1.4 GHz is relatively easy.

Radio selected samples of galaxies can be broadly divided into four sub-classes[10]; radio loud AGN, radio quiet[11] AGN, normal star-forming galaxies and starbursts. As yet there is no clear concensus on why radio AGN subdivide into these two distinct loud and quiet populations. It could be due to differences in the accretion mechanisms of the supermassive black holes, sources of synchrotron emission or geometries, as well as the influence of star formation. To date the AGN population counts are very incomplete with the deepest radio surveys only just sampling the brightest end of the radio quiet AGN distribution.

Classical radio AGN are the most luminous and dominate 1.4 GHz radio source counts above mJy flux levels. They are not necessarily radio loud, and are typically subdivided into two main Fanaroff-Riley classes. FRI AGN are relatively compact and optically thick to their own sychrotron radiation. FRII are in general more luminous than FRI AGN, they exhibit bright extended (often Mpc in scale) radio jets which are optically thin. At flux densities fainter than 1 mJy both radio quiet and radio loud AGN exist. Smolčić et al. (2008) have found that faint radio loud AGN, which are generally not detected at any other wavelengths, are preferentially hosted in red quiescent galaxies. This means that radio surveys could help shed light on the evolution of black holes in conjunction with their host galaxies.

Current radio observations, such as the (J)VLA-COSMOS surveys at 324 MHz (Smolčić et al., 2014), 1.4 GHz (Schinnerer et al., 2010) and 3 GHz (Smolčić et al. in press) are reaching (rms) depths of 500, 10 and 2.3 μJy/beam respectively. The GMRT survey of COSMOS at 610 MHz described in Chapters 3 and 4 reaches a depth of 45 μJy/beam. Below 1 mJy there is a well characterised observed upturn in the 1.4 GHz sources counts, as shown in Figure 1.6 for the Wilman et al. (2008) simulations. The upturn below 1mJy has been often attributed to star forming

[10] See Wilman et al. (2008); Smolčić et al. (2014) and references therin for more detail. Also note that there is no clear luminosity division between these classes

[11] Radio loudness is defined as the ratio of the radio flux density to the optical flux density (or the IR, depending on whether it's a Type I (visible nucleus) or II (obscured nucleus) AGN). $R' = log(F_{optical}/F_{radio})$, with R'=1 being the radio loud/quiet threshold.

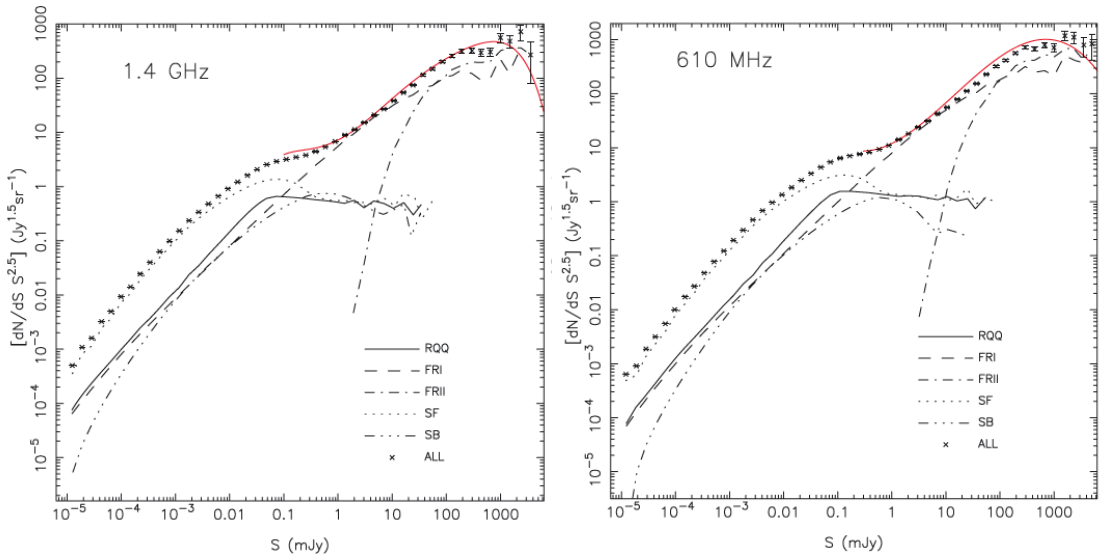

FIGURE 1.6: Source counts from the semi-empirical simulation of Wilman et al. (2008) of 400 deg^2 down to flux densities of 10 nJy and out to a redshift of z =20. The 1.4 GHz source counts are shown in the left panel and the 610 MHz in the right. The abbreviations are as follows; RQQ= radio quiet quasar, FRI and FRII are the radio loud AGN here, SF=star forming and SB = starburst. The red line represents a polynomial fit to observations.

galaxies although Smolčić et al. (2008) has shown that radio quiet AGN can contribute significantly to it (being 50-60% of the 1.4 GHz submJy population) based on an optical color selection of radio AGNs in the VLA-COSMOS 1.4 GHz survey of Schinnerer et al. (2010).

1.2.1 Origin of Radio Emission

Emission at radio frequencies in galaxies arises either as a result of (massive) star formation or AGN activity (in particular jets). The radio spectrum of galaxies is relatively well decribed by a combination of power laws; $S_\nu \propto \nu^\alpha$, where S_ν is the spectral flux density. It is usually a combination of non-thermal synchrotron emission from relativistic electrons and thermal free-free radiation with differing spectral slopes (α), as illustrated in Figure 1.7 for M82, a classic starburst galaxy. Condon (1992) has a comprehensive review of radio emission in galaxies, in the following we will briefly summarise the main points.

In the case of thermal emission, the energy distribution depends on the temperature of the emitting body/region (e.g as in the case of a black body). The term 'free-free' refers to the specific case when electrons scatter off ions. The free-free

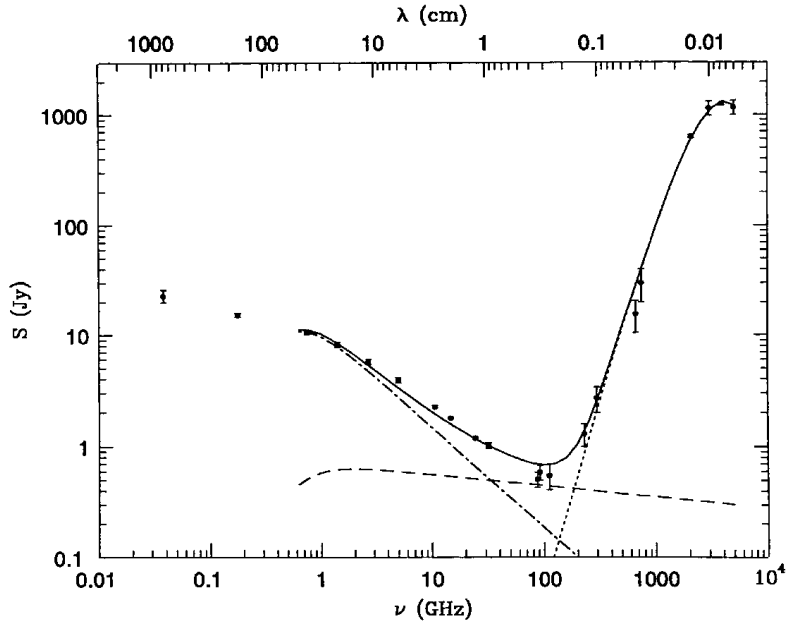

FIGURE 1.7: The classic M82 model of the radio SED of a (starburst) galaxy from Condon (1992). Synchrotron emission (dot-dashed line) dominates below 10 GHz and has a spectral slope of -0.8, free-free emission (dashed line), with a spectral slope of -0.1, is the main contributor to the total emission in the 30-100 GHz frequency range. ∼100 GHz defines the upper limit of the radio regime - above that IR emission (dotted line) from dust in the ISM dominates. The solid black line is the sum of the three components.

emission of interest here occurs in star-forming regions where electrons scatter off HII ions and has $\alpha = -0.1$. Synchrotron emission at radio wavelengths occurs when electrons follow helical orbits in magnetic fields. A key signature of synchrotron radiation is a pure power law spectrum. At lower frequencies (below the 'turn over' frequency) synchrotron self-absorption becomes important - that is the medium become optically thick to its own radiation at those frequencies - with α=2.5. It should also be noted that the synchrotron energy loss rate is proportional to ν^2 and thus at high frequencies the radio spectrum curves downward[12]. In the case of synchrotron emission due to star-formation α=-0.8 or -0.7. In AGN synchrotron emission comes from electrons accelerated in the radio jets - when the radio source is compact α=-0.2 and for more extended regions we have α=-0.7. At higher redshifts populations of ultra-steep spectrum (α <-1) sources have been observed. These AGN seems to be primarially hosted in rich galaxy clusters, where pressure confinement of their radio lobes may lead to brightening of the steepest spectrum radio emission.

[12]This is one reason why lower frequency bands are preferable for observations of non-thermal synchrotron emission in galaxies.

1.2.1.1 Radio Emission from Star Formation

The light output of young stellar populations is dominated by the most massive (O and B, for example) stars. Therefore any tracer that is sensitive to the emission of the short-lived massive stellar population should be an excellent probe of recent star formation and hence of the 'instantaneous' star formation rate.

Stars with masses $> 8\,M_\odot$ ionize their surrounding medium, creating HII regions. Free-free emission from HII regions is therefore a direct tracer of the rate of production of $> 8\,M_\odot$ stars. However, free-free emission only dominates the radio signal of a typical star forming galaxy in the 30-100 GHz frequency range (see Figure 1.7), which is sparsely observed. Above 100 GHz (wavelengths below 3000 μm) thermal IR emission from the dust in the ISM starts to dominate. Although authors such as Murphy et al. (2011) have shown (locally) that 30 GHz free-free emission is a very reliable SFR tracer, it has been impractical to use it as a SFR tracer at high z because the shallow spectral slope of the free-free component means that most normal star-forming galaxies are not bright enough to be detected at $\nu >$10 GHz[13] and free-free emission is quickly swamped by the steeper-spectrum synchrotron emission at lower frequencies. The ubiquity of lower frequency radio observations (particularly 1.4 GHz) means astronomers are usually forced to rely on the non-thermal radio emission instead.

Stars more massive than $8\,M_\odot$ typically live less than 30 Myr and end in Type II or Type Ib supernovae. The shocks from these explosions create turbulent magnetic fields in the surrounding ISM, whereby electrons are accelerated to relativistic speeds and synchrotron radiate. The lifetimes of these relativistic electrons are typically $\leq$ 100 Myr and thus radio observations probe very recent star formation [14]. Such synchrotron emission dominates the output of a star-forming galaxy at rest-frame frequencies below 30 MHz (Figure 1.7). Simulations, such as Starburst99 (Leitherer et al., 1999), are used to relate the core-collapse supernova rate of $> 8\,M_\odot$ stars to the SFR and then an empirical relation of the non-thermal radio spectral luminosity to the supernova rate yields a SFR calibration for the non-thermal radio emission (see Murphy et al. (2011); Kennicutt (1998) for more details).

[13] Although the upgraded JVLA and the SKA will be able to do so in the near future.

[14] Although we normally only observe the more extended emission from the older >10 Myr electrons.

1.2.2 Tracing Star Formation with Radio Emission

As mentioned in the previous subsection, the 1.4 GHz non-thermal continuum is one of the most popular bands used to estimate radio SFRs. The simple form of the radio SED allows one to easily K-correct[15] to the rest-frame value, by assuming a spectral slope of $\alpha = -0.8$ (we refer the reader to Section 2.3.2 where the formulas for converting the observed flux to rest-frame luminosity and SFR are outlined)[16]. The emission in the 1.4 GHz band is, as previously discussed, a superposition non-thermal synchrotron emission with a spectral index α=-0.8 and thermal free-free emission with α=-0.1. The M82 SED of Figure 1.7 is usually used to model the radio SED of a star-forming galaxy, in that it is assumed that in the rest-frame the free-free contribution to the 1.4 GHz emission is at most 10% of the total flux. Following this, certainly out to $z \sim$2, the contribution of the free-free component can be safely ignored, in that we can assume the total measured 1.4 GHz continuum flux is due to non-thermal synchrotron radiation.

Relating the rest-frame non-thermal spectral luminosity to the SFR is complicated - one needs to model the Type II and Ib supernova rate, the acceleration of electrons in the supernova remnants, the propagation of radiation through the interstellar medium and the energy losses. This involves many complicated physical processes that are not well understood. In practice, these calibrations are almost never used. Fortunately astronomers can take advantage of an observed relation between the total IR (8-1000 μm) luminosity and the 1.4GHz luminosity of star-forming galaxies, the so-called IR-radio correlation (IRRC), to empirically calibrate radio SFR tracers (Section 2.3.2).

1.2.2.1 The IR-Radio Correlation

The infrared-radio correlation (IRRC; Figure 1.8) is a tight linear empirical correlation between the bolometric IR luminosity of a star-forming galaxy and its intrinsic 1.4 GHz spectral luminosity[17] (de Jong et al., 1985; Helou et al., 1985;

[15] That is convert the observed flux of a galaxy at redshift z in a certain band to the equivalent value in the rest-frame of the galaxy (for example, for a galaxy at z=1 the 1.4 GHz band is measuring the rest-frame 3 GHz output.). This would not be necessary if one could meaure the full spectral output, but of course this is impossible in practice except in the case of a few in-depth studies of very small samples of local galaxies.

[16] $-0.7 \leq \alpha \leq -0.8$ is a typical observed value for star-forming (main sequence and starburst) galaxies, both locally and at higher z.

[17] See Equation 2.2

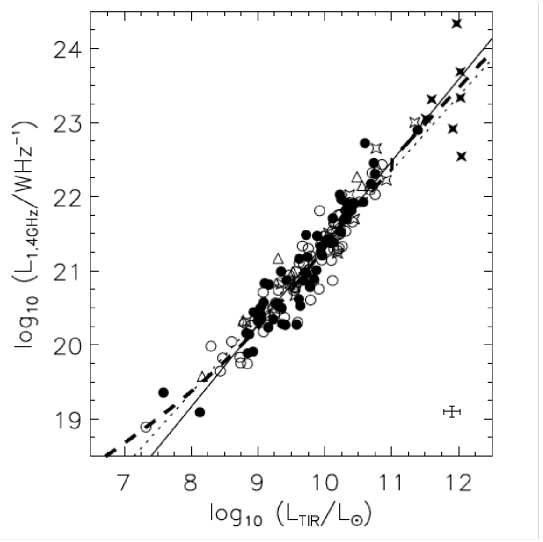

FIGURE 1.8: The infrared-radio correlation from Bell (2003). The datapoints represent a sample of 162 galaxies from several local surveys. Normal star-forming galaxies are represented by open circles, ULIRGs by filled stars, starbursts by open stars and blue compact dwarfs by open triangles. The dotted and solid lines are two different linear fits to the datapoints and the thick dashed line represents the trend predicted by the Bell (2003) SFR calibrations. Note that the relation is nearly linear and very tight (scatter of 0.26 dex).

Condon, 1992; Yun et al., 2001; Bell, 2003). The correlation holds across several orders of magnitude in luminosity and a wide range of morphologies and has been well characterised out to z∼2. It has also been observed to hold even for star-forming regions of 0.5 kpc scales within galaxies (Murphy et al., 2008; Tabatabaei et al., 2013). The IRRC has a value consistent with $q_{TIR} = 2.64 \pm 0.26$ (as in (Bell, 2003) for a set of local star-forming galaxies with total IR luminosities from $\sim 10^{7.5}\,L_\odot$ to $\sim 10^{12}\,L_\odot$).

The theoretical orgins of the IRRC are not fully understood- modelling has so far failed to agree with most of the observational constraints beyond the basic properties. Simply put, the correlation's origins lie in the shared source of the IR and radio emission. In a dusty cloud where young massive stars reside, most of their energy will be radiated at UV wavelengths which are preferentially absorbed by dust and re-radiated at MIR and FIR wavelengths. After a few Myr these massive stars will explode in a supernova which will produce synchrotron emission as electrons are accelerated in the galactic magnetic field. However, these two regimes are governed by different physics - why the correlation should remain so tight in galaxies of different luminosities (and hence different star-forming environments), on many scales and remain constant with redshift (given that conditions in the ISM

do change as a function of z and as one moves off the main sequence) is unclear. Authors such as Murphy et al. (2009); Lacki et al. (2010); Lacki & Thompson (2010) propose a 'conspiracy' between different physical processes to maintain the correlation. Yet there is still an open debate on whether the correlation holds true beyond z =2 and whether it should increase[18] or decrease[19]. Sargent et al. (2010) analysed the IRRC out to z =4 and found that many of the discrepancies in high z measurements could be explained by sample selection effects. Of late, several authors have proposed that the evolution in the IRRC is in fact real; Magnelli et al. (2015) and Delhaize et al. (subm.) have both seen evidence for a redshift evolution in the IRRC towards lower values at higher z, suggesting the local radio SFR calibration needs to be recalibrated at high redshifts. From their analysis of a sample of galaxies out to z =5, Delhaize et al. (subm.) conclude that it is an incorrect K-correction of the radio luminosities that is driving the observed redshift evolution in the IRRC, in that the contribution of the free-free emission to their radio fluxes is inconsistent with the typical M82-based radio SED model. Clearly there is still much work to be done to characterise the IRRC and the form of the radio and IR SED at high redshifts.

1.3 Surveys: COSMOS

In studies of galaxy evolution, one would ideally have deep multiwavelength observations of a wide field. Wide fields are necessary to mitigate the effects of cosmic variance. The largest structures in the local Universe are on scales of 100s Mpc. It is thus important to choose a field large enough to include a representative sample of these structures (overdensities and voids), particularly to address the crucial influence of the cosmic environment on galaxy evolution. Deep observations on large areas (several deg^2) are costly and impractical to attempt. A common compromise it to use a 'tiered wedding cake' approach, whereby the all sky coverage is complemeted by much deeper 'pencil beam' observations in small carefully selected subfields. This approach allows for in-depth investigation of an extensively covered (multiwavelength and deep) small area, to inform the interpretation of the properties of the shallower full-field surveys.

[18] A scenario preferred by Murphy et al. (2009) is that inverse Compton scattering off CMB photons reduces the synchrontron output and leads to a slight increase in q_{TIR} at higher z.

[19] Lacki & Thompson (2010) propose that actively star-forming galaxies at higher z are more extended than their local counterparts.

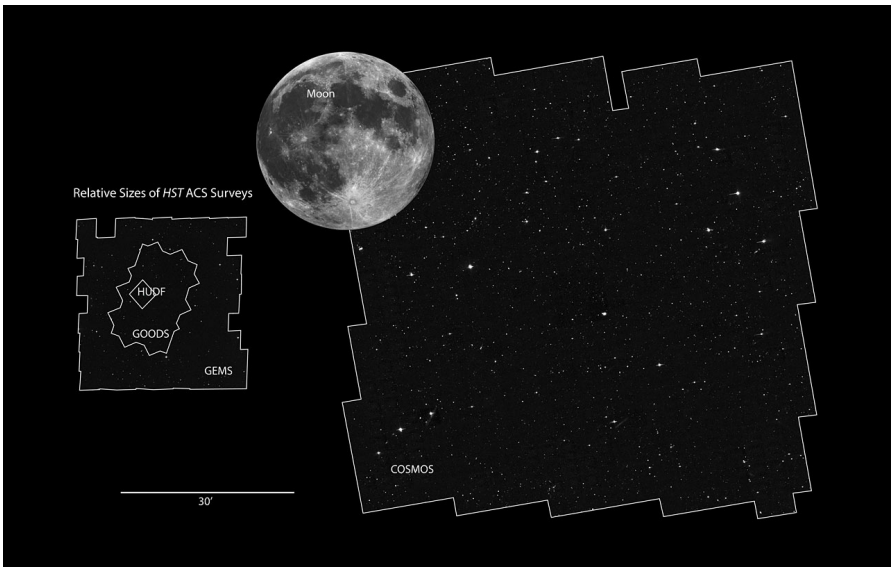

FIGURE 1.9: The Hubble Space Telecope (HST) survey of the $2deg^2$ COSMOS field. For comparison, other fields covered by HST surveys are shown, as is the full moon (0.5 deg).

COSMOS is one of the foremost fields for studies of galaxy evolution. Other surveys such as the Sloan Digital Sky Survey (SDSS York et al., 2000) cover larger areas, but lack the multiwavelength coverage and extensive ancillary datasets that COSMOS has. Perhaps only the Great Observatories Origins Deep Survey (GOODS Chatzichristou & Goods Team, 2004), which includes the Hubble Ultra Deep Field, rivals COSMOS in terms of spectral coverage, although it covers a much smaller area. COSMOS is thus uniquely equipped to address the coupled evolution of large scale structure, star formation and AGNs across large lookback times.

1.3.1 COSMOS

The Cosmic Evolution Survey (COSMOS) of Scoville et al. (2007b) has unprecedented panchromatic coverage of a 2 deg^2 equatorial field[20]. The largest scale structures at $z \sim 1$ have a similar angular extent to the COSMOS field and thus it can trace the evolution of large scale structure at $z \geq 1$ in a statistically representative manner (the field contains $\sim 2 \times 10^6$ galaxies). It includes high sensitivity imaging and spectroscopy from both ground- and space-based observatories across the X-ray, UV, optical, IR, mm, submm and radio. Photometric redshifts

[20]We refer the reader to the COSMOS ApJS special issue (September 2007, Volume 172) for a full outline and to Section 2.2 for more detail on the main surveys of interest to this thesis.

and masses are available for $> 10^6$ galaxies (Laigle et al., 2016) and spectroscopic redshifts for close to 100,000 galaxies.

1.3.2 Radio Imaging of COSMOS

The COSMOS field has been covered by radio continuum surveys in several bands with high sensitivities and spatial resolutions. The 324 MHz survey of Smolčić et al. (2014) reaches depths of 500 μJy/beam at a resolution of $8'' \times 6''$, the 1.4 GHz large and deep surveys of Schinnerer et al. (2004, 2007, 2010) reach depths of $\sim$10 μJy/beam at resolutions of $1.5''$ and $2.5''$ respectively. The 3 GHz survey of Smolčić et al. (in press) has a depth of 2.3 μJy/beam at a resolution of $0.75''$. Part of the work of this thesis has focused on producing an image and catalogue of COSMOS at 610 MHz with Giant Metrewave Radio Telescope (GMRT) data (Chapters 3 and 4). These sensitivities and spatial resolutions on such a large area means that the COSMOS field is currently unrivalled[21] as a resource for studies of the extragalactic radio population, and will be for the near future until the next generation facilities such as the upgraded VLA (Very Large Array Sky Survey Murphy et al., 2015) and Square Kilometre Array (SKA Norris et al., 2015) see first light.

1.3.3 Overview

We are now entering the era of deep wide-field IR and radio astronomy; with the JWST IR satellite due to launch in 2018 and the SKA radio interferometry array coming online in 2020. It is now timely to investigate the consistency of the IR and radio SFR tracers for very actively star forming galaxies at high redshifts, which will also necessitate testing how well local models of the spectral energy distribution of galaxies at these wavelengths can represent their high redshift counterparts. All of this work presented in this thesis is done in the COSMOS field which affords the possibility to study large statistically meaningful samples of galaxies owing to the extensive coverage across the electromagnetic spectrum and large number of spectroscopic redshifts. In Chapter 2 we compare the most popular IR and radio SFR tracers on a sample of high redshift starburst galaxies. In Chapters 3 and 4

[21] For example, FIRST, although covering a wide field at 1.4 GHz, has a depth of 150 μJy/beam and a resolution of $5''$.

we present the first image and catalogue of the COSMOS field at 610 MHz, as well as a summary of the properties of the low-frequency (610 MHz) radio population. The 610 MHz band will be one of the main bands of the SKA and our catalogue is complementary to several others within COSMOS at cm wavelengths. It will be of use in studies of the evolution of the spectral shape of the radio SED, its evolution with redshift and probing the rest-frame 1.4 GHz emission (at z$\sim$1.3 it shifts into the 610 MHz band) to better understand radio emission as a result of star formation on cosmic timescales, as well as the evolving make-up of the radio galaxy population. The scientific results and future prospects are presented in Chapter 5.

Chapter 2

A Comparison of Radio and IR SFR Tracers at High Redshifts in COSMOS

In this chapter we present an analysis of the the consistency of dust-unbiased star formation rate (SFR) tracers at high redshifts. We compare a 1.4GHz radio continuum tracer to infrared (IR) SFRs obtained from extrapolating from a single MIR or FIR band with a wide variety of publically available spectral energy distribution (SED) model templates on a sample of 649 star-forming galaxies in the COSMOS field out to $z \sim$2.3. We find that, using the $\mathrm{SFR_{1.4GHz}}$ as a benchmark, locally calibrated SED models fail to produce consistent $\mathrm{SFR_{IR}}$ for starburst galaxies. $\mathrm{SFR_{IR}}$ are very dependent on the choice of SED and normalization band and exhibit redshift evolution, with offsets of as much of a factor of 2 locally and up to 5 at $z >$1. We verify that the effects of systematics coming from AGN contamination, flux uncertainties, photometric redshifts and radio spectral slope assumptions are not the cause of the disagreement. Requiring direct 5 σ detections at 1.4 GHz and in the MIPS 24 μm and PACS 100 μm bands restricts the sample to starburst galaxies at all but the lowest redshifts. The galaxies move increasingly off the main sequence with z, leading to the sample consisting entirely of extreme ($R_{SB} > 10$) starbursts beyond $z \sim$1. Although some previous authors have found that high redshift starbursts have IR SEDs similar to that of local ones, we find that this is likely not the case for the extreme starbursts. Either the SEDs of these galaxies have weaker polycyclic aromatic hydrocarbons (PAH) and a more diffuse (cooler) ISM, or alternatively some of the disagreement in the SFR comparison could come

from the radio side - with an infrared-radio correlation (IRRC) evolving towards lower values for higher SFR systems.

This chapter will be submitted to ApJ in the early Autumn as:
A Comparison of Dust-unobscured SFR Tracers at High Redshifts in COSMOS
Brady, E., Schinnerer, E., Groves, B., et. al.

2.1 Introduction

Measuring the rate of stellar mass build-up in galaxies over cosmic times is crucial to the understanding of galaxy formation and evolution. A tracer that accurately determines the star formation rate (SFR) is a key component in that measurement.

There is a huge variety of tracers in use, both in terms of wavelength employed and specific calibration/modelling (Kennicutt, 1998; Kennicutt & Evans, 2012). Yet an underlying issue is the consistency between tracers, when several of the fundamental cosmic evolution studies have used different calibrations (see Madau & Dickinson (2014) for a review). Most tracers have been calibrated on local sample of galaxies, yet the early universe is dustier, more gas-rich and actively star-forming than the present (Daddi et al., 2005; Gruppioni et al., 2013). The evolution in these properties and others, such as the global metallicity or dust properties, make the extension of standard calibrations to high redshifts and more extreme star-forming galaxies less reliable. In fact there is already an observed large scatter and offset in different tracers locally (Murphy et al., 2009; Davies et al., 2016) suggesting large uncertainties in predicted SFRs of the high-z galaxies.

The UV is a readily accessible SFR tracer as these bands shift into optical wavelengths at high redshift. Yet the UV as a SFR tracer always requires a correction for extinction (Kennicutt, 1998). The increased dust content and IR luminosity of galaxies at increasing redshift (Caputi et al., 2007), indicate that a increasingly larger correction is necessary, making the UV determined SFRs more uncertain.

Given the rise in IR luminosities with redshift, this wavelength range is an obvious SFR tracer at high-z. The lower resolution of most surveys and incomplete IR coverage mean that usually a single IR band (such as 24 μm) is used, and then transformed to a SFR through an infrared spectral energy distribution (SED)

based on local samples of galaxies. However, there is strong evidence that the IR SED libraries used for most IR SFR calibrations are not directly representative of the high-z population (Elbaz et al., 2011; Murphy et al., 2009; Magdis et al., 2012; Papovich et al., 2007).

Conversely, other works (e.g. Elbaz et al., 2011; Magdis et al., 2012; Kirkpatrick et al., 2012) have shown that 'typical' star-forming galaxies have a tight constant linear correlation between the MIR color and bolometric IR luminosity. This points to the existence of a universal IR SED that does not evolve appreciably over cosmic times and make extrapolation to the SFR from a single IR band possible, which is often the only recourse for faint and distant galaxies with limited band coverage. These 'typical' star-forming galaxies are galaxies that follow the observed tight relation between the SFR and stellar mass, the so-called 'star-formation main sequence' (MS). This main sequence has been observed out to $z \sim 7$ (Noeske et al., 2007; Elbaz et al., 2007; Daddi et al., 2007; Magdis et al., 2010), with a roughly constant slope and an increasing specific SFRs (sSFR $=$SFR/M$_*$) with redshift (Karim et al., 2011; Whitaker et al., 2012; Pannella et al., 2015).

The radio continuum is a dust-unbiased SFR tracer, requiring no extinction correction, and with high resolution imaging possible with radio arrays such as the Jansky VLA. The radio SFR tracer calibrations rely on the empirical IR-radio correlation (IRRC), a tight linear correlation that is observed between the infrared and radio emission of galaxies across a wide range of redshifts, luminosities and morphologies (de Jong et al., 1985; Helou et al., 1985; Condon, 1992; Yun et al., 2001; Bell, 2003). Yet there is now mounting evidence that this correlation may be a conspiracy between different physical processing working in tandem to maintain the correlation (Murphy, 2009; Lacki et al., 2010; Lacki & Thompson, 2010). Magnelli et al. (2015) and Delhaize et al. (subm.) have seen evidence for a redshift evolution in the radio-IR correlation, suggesting the local radio SFR calibration cannot be blindly applied at high redshift.

To address this issue of the reliability of local calibrations of SFR tracers to high redshift, we investigate the agreement between two commonly used SFR measurements in high-z studies; the bolometric IR luminosity (8-1000 μm), extrapolated from a single band using a locally derived IR SED template and a radio SFR based on the observed 1.4 GHz radio continuum. Our sample is based on the VLA-COSMOS 'joint' catalog of Schinnerer et al. (2010), providing a deep sample of 1.4 GHz observations of star-forming galaxies out to redshift $z \sim 3$. This

is supported by the multiwavelength data of the COSMOS survey (see Scoville et al., 2007b, for an overview of this survey) for proper redshifts and diagnostics of the high-z galaxies. In particular, data from two IR surveys, the Le Floc'h et al. (2009) *Spitzer*/MIPS 24 μm catalog of the MIPS-Spitzer survey data (Sanders et al., 2007), and the 100 μm *Herschel*/PACS Evolutionary Probe survey data (PEP Lutz et al., 2011; Magnelli et al., 2013), are vital to determine the IR SFRs using two different monochromatic bands.

Using this multiwavelength dataset, we disentangle the effects of uncertainties in photometry, AGN contamination and sample selection bias (and its evolution with redshift) in order to quantify how well the different SFR tracers agree. We specifically investigate if any existing universal IR SED can be applied to a high redshift radio and IR-selected population and if the assumption of a constant (with z and L) radio-far infrared correlation is still valid.

The chapter is organised as follows: The data sets are introduced and the comparison sample selection process outlined in Section 2.2. The star formation rate recipe employed and the spectral energy distribution models for the IR luminosity calculations are detailed in Section 2.3. In Section 2.4 we present the main results of the radio and IR-based SFR comparison. A discussion of the evolution of the IR SED and/or the IRRC is presented in Section 2.5. Section 2.6 summarises our conclusions.

We use the standard ΛCDM cosmology (Ω_m=0.3, $\Omega_\Lambda = 0.7$ and $H_0 = 70$ km s$_{-1}$ Mpc^{-1}) throughout and all magnitudes are given in the AB system of Oke (1974).

2.2 Data Sets and Sample Selection

A meaningful comparison of dust-unbiased star formation rate (SFR) tracers relies on a robust sample of star forming galaxies. This study is made possible by the unique and comprehensive COSMOS survey. COSMOS is a pan-chromatic survey (for an overview, see Scoville et al., 2007b) with un-precedented coverage across the electromagnetic spectrum from X-ray to radio of a 2 deg^2 (large enough to be unaffected by cosmic variance) equatorial field centred on RA=10:00:28.6 and Dec=+0.2:12:21.0 (in J2000 coordinates). It has been imaged in depth in the X-ray by the *XMM-Newton* and *Chandra* satellites(Hasinger et al., 2007; Elvis et al., 2009), in the UV with *GALEX* (Zamojski et al., 2007), by ground-based optical

and near-infrared facilities (Taniguchi et al., 2007; Capak et al., 2007) and by the *Hubble Space Telescope* (Scoville et al., 2007a; Koekemoer et al., 2007), in the mid- to far-infrared with the *Spitzer* space telescope (Sanders et al., 2007), millimeter bolometer cameras (Bertoldi et al., 2007; Scott et al., 2008) and in the radio with the VLA (Schinnerer et al., 2007; Smolčić et al., 2014). Complementary to this are extensive optical spectroscopy catalogs obtained with the VLT/VIMOS and Magellan/IMACS instruments (Lilly et al., 2007; Trump et al., 2007)[1], with spectroscopic redshifts for a significant number of the sources as well as photometric redshifts (Ilbert et al., 2013; Laigle et al., 2016). COSMOS thus affords us the unique opportunity to pursue deep, multi-wavelength studies of galaxy evolution.

2.2.1 The Radio and IR Data

The 1.4 GHz radio data used in this analysis is from the VLA-COSMOS 'joint' catalog of Schinnerer et al. (2010). The VLA-COSMOS project (Schinnerer et al., 2004, 2007) imaged the COSMOS field to a 1σ depth of 8μJy/beam in the central $30'\times30'$ area and 12μJy/beam outside. The 'joint' image is a combination of the 'large' (Schinnerer et al., 2007) and 'deep' (Schinnerer et al., 2010) observations resulting in images with resolutions of $1.5''$and $2.5''$ respectively. Source detection and flux measurements were performed with AIPS and all source properties listed in the joint catalog were determined at the $2.5''$ resolution. The catalog contains 2864 sources with S/N$\geq$5, 5% of which are classed as multi-component sources and 14% (of all sources) are resolved. As the multi-component sources typically have morphologies consistent with radio galaxies (Schinnerer et al., 2010), we restrict the sample to the 2733 single component sources from the 'joint' catalog. More details on the sources and their derived properties are given by Schinnerer et al. (2010).

The 24 μm and 100 μm measurements used here are taken from the first PACS Evolutionary Probe (PEP) collaboration public data release[2] (Lutz et al., 2011; Magnelli et al., 2013), specifically the catalog obtained with 24 μm position priors and PSF fitting. The set of 24 μm priors for the COSMOS field are from the Le Floc'h et al. (2009) catalog of the MIPS-Spitzer survey data (Sanders et al., 2007). The MIPS sources were extracted with SExtractor and flux measurements

[1]Many of these data products are publically available on the IPAC/IRSA COSMOS archive: http://irsa.ipac.caltech.edu/Missions/cosmos.html

[2]http://www.mpe.mpg.de/ir/Research/PEP/DR1

made with a PSF of 6″ to create a prior catalog down to a 3σ depth of 45 μJy. For the extraction of the 100 μm fluxes, only those sources with $S_{24} \geq 60\,\mu$Jy were used. By masking at the positions of the 24 μm priors in the 100μm image, a good residual map for noise estimation is obtained, giving an average rms of 1.5 mJy. The 100 μm fluxes are estimated by fitting a 7.2″ PSF at the 24 μm positions. In total there are 3876 sources with S/N≥5 at both 24 μm and 100 μm that we will use. More details on the determination of sources and their properties can by found in Lutz et al. (2011) and Magnelli et al. (2013).

2.2.2 Photometry and Redshifts

Photometric redshifts, rest-frame colors and masses are taken from the photometry catalog of Laigle et al. (2016), who utilise data in 29 bands across the full COSMOS field. In the optical/UV these are the NUV band of GALEX (Zamojski et al., 2007), u^* from CFHT/MegaCam (Capak et al., 2007) and the 5 broad bands (B,V,r,i,z^{++}), 12 medium bands (IA427-IA827) and two narrow bands (NB711, NB816) of the Subaru SuprimeCam survey of Taniguchi et al. (2007)[3]. NIR YJHK$_s$ data are from the VIRCAM observations released in the UltraVISTA DR2 (McCracken et al., 2012). The mid-IR 3.6 μm, 4.5 μm, 5.8 μm and 8 μm data are from the S-COSMOS survey with the IRAC instrument of Sanders et al. (2007), updated with the Spitzer Extended Mission Deep Survey (SPLASH) of Capak et al. (in prep.). GALEX photometry is obtained from a cross match with the Capak et al. (2007) catalog. Photometry in the optical and NIR is obtained using SExtractor in "dual image" mode on a chi-squared z^{++}YJHK$_s$ image. Detections are made on the non-homogenised image and fluxes in these bands are extracted with 2″ and 3″ apertures on PSF-homogenised images. Mid-IR photometry is derived with IRACLEAN (Hsieh et al., 2012) with 1.8″×1.8″ apertures using the z^{++}YJHK$_s$ chi-squared image as a prior.

Photometric redshifts are obtained with the 3″ aperture fluxes and the LePhare χ^2 SED fitting code (Arnouts et al., 2002) as described in more detail in Ilbert et al. (2013, 2009). A set of 31 templates is used; spiral and elliptical templates (Polletta et al., 2007) and 12 young, blue, star-forming templates (Bruzual & Charlot, 2003). Extinction is left as a free parameter, with several attenuation

[3]Note that the z^+ band data described in Taniguchi et al. (2007) has since then been updated with the z^{++} used in Laigle et al. (2016).

laws considered. A large spectroscopic redshift training sample (mostly zCOSMOS bright (Lilly et al., 2007) and deep (Lilly et al. in prep) is used to characterise and estimate the precision of the $z_{\rm phot}$. The $z_{\rm phot}$ used here is the median of the likelihood distribution 'zPDF', in addition the upper and lower 68% limits $z_{\rm u68}$ and $z_{\rm l68}$ are provided. Masses and rest-frame colors are determined from the best fit template at $z_{\rm phot}$ using LePhare and Bruzual & Charlot (2003) templates, which incorporate a Chabrier initial mass function (IMF), several metallicities and combinations of exponentially declining and delayed star-forming histories (SFHs). The final catalog consists of sources detected on a $z^{++}YJHK_s$ image with 3σ AB depths ($3''$ apertures) of 25.9, 25.3, 24.9, 24.6 and 24.7, respectively. Stars (6%) are identified by including stellar templates in the fit and any objects masked in the optical bands (41%) are considered suspect and thus disregarded in our analysis.

For additional quality control of the $z_{\rm phot}$ in our radio-selected sample we use the COSMOS spectroscopic redshift compilation (M. Salvato, private communication). This is a mixture of private and public data from 2dF, 2MASS, SDSS DR12, VIMOS zCOSMOS bright and deep, IRS, FOCAS, FMOS, MMT and VUDS (Salvato et al., in prep.; zCOSMOS, Lilly et al. 2007, 2009; Trump et al. 2007; Prescott et al. 2006; Le F'evre et al. 2015; Aihara et al. 2011; Nagao et al., priv. comm.) for 97,102 sources within COSMOS. Quality flags are as described in Lilly et al. (2007) and any $z_{\rm spec}$ with a quality flag $Q_{\rm f} \geq 3.5$ (40%) is considered very secure.

2.2.3 Resources for AGN Identification

In order to identify AGN in our sample we make use of a compilation of all COSMOS AGN known by 2012 (M. Brusa, priv. comm). This catalog consists of 5630 AGN identified in the COSMOS field up to that date. In particular this list includes (with significant overlaps): 1515 X-ray AGN from Chandra (Brusa et al., 2010) and 1649 XMM sources from Civano et al. (2012), 487 narrow line AGN from Bongiorno et al. (2010) and Mignoli et al. (in prep) and 438 broad line AGN from Zamorani et al. (in prep.) from the zCOSMOS survey, 3097 infrared IRAC-detected AGN from Donley et al. (2012) and Le F'loch et al.[4] (in prep) and, finally, 729 radio AGN detected with the rest-frame color indicator as described in Smolčić et al. (2008). The Chandra COSMOS Legacy survey Civano et al. (2016) catalog is used to select X-ray AGN using a luminosity cut as described in Civano

[4]Also uses MIPS data in a 'power law' selection.

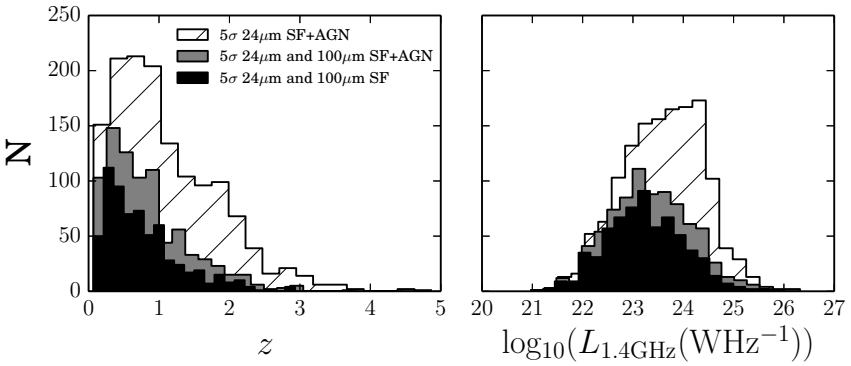

FIGURE 2.1: The photometric redshift (Laigle et al., 2016) distribution (left) and the rest-frame 1.4 GHz radio luminosity distribution (right). The full (star forming galaxies and AGNs) sample with a single radio-component, secure photo-z and 5σ 24 μm measurements (1387 galaxies; hatched), with 5σ 24 μm and 100 μm detections (822 galaxies; gray) and our final star-forming comparison sample (known AGN removed) which has 5σ 24 μm and 100 μm detections (649 galaxies; black)

et al. (2012). The catalog, which covers the entire COSMOS field area, contains 4,016 sources. 3814 of these are full band (0.2-10keV) sources, which reach a limiting depth of 8.9×10^{-16} erg cm^{-2} s^{-1}.

2.2.4 Star-Forming Sample Selection

For the purposes of this study we require a sample with good radio and IR measurements and secure photometric redshifts, whose emission can be confidently attributed to star-formation rather than AGN activity.

We matched the radio catalog and the IR catalog (as described in Section 2.2.1) using a 0.5″ search radius[5] (shown by Smolčić et al. (2008) to give reliable results) to obtain a final sample of 1011 members that are single component radio sources and have 5σ 24 μm and 100 μm detections (see Figure 2.1).

This 1011-member radio-IR sample was positionally cross matched (0.5″ search radius) with the photometry catalog of Laigle et al. (2016). After photometric redshift quality control cuts were implemented, discarding any galaxy with $(z_{\rm u68} - z_{\rm l68})/(2z_{\rm phot}) > 10\%$, a total of 824 radio-IR detected sources with reliable redshifts was left. Two of these sources with 'good' photometric redshifts were identified as

[5]which results in a maximum separation of 1″ on the sky between members of a matched pair

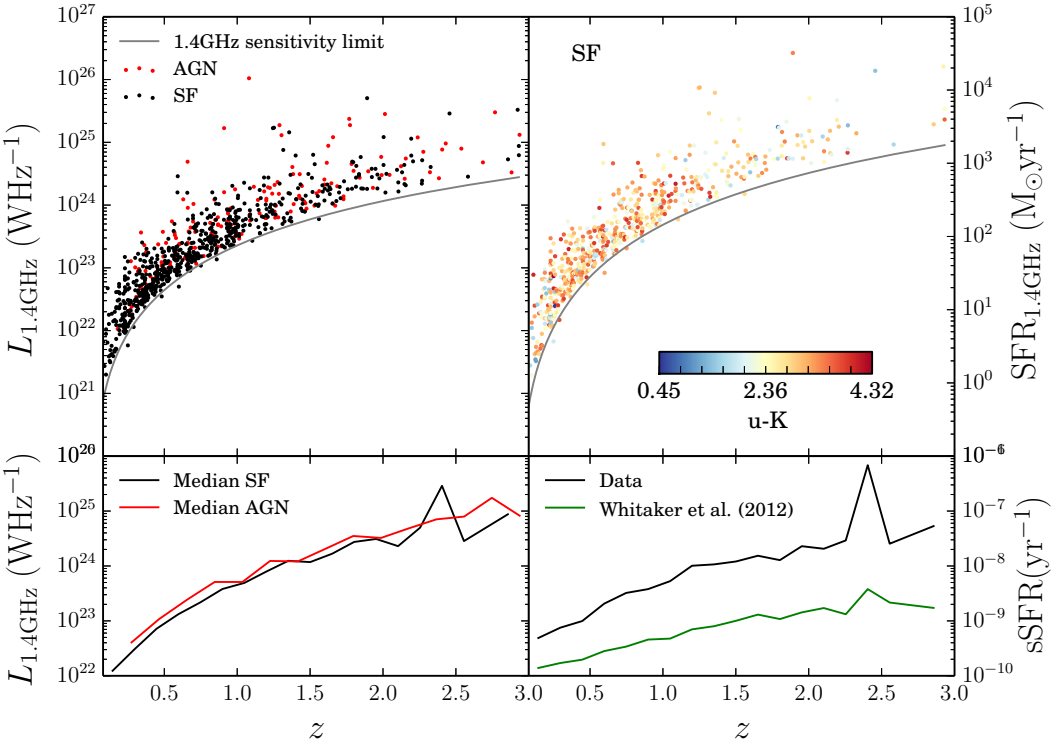

FIGURE 2.2: Left, top: The rest-frame 1.4 GHz luminosity as a function of redshift for the final comparison sample of 649 star-forming galaxies with 5σ 24 μm, 100 μm and 1.4 GHz measurements (black) and the 173 AGN rejected from this sample (red). The solid gray line representents the sensitivity limit of the Schinnerer et al. (2010) survey. The median luminosities of the star-forming and AGN samples are plotted in the bottom, left panel in redshift bins of width 0.15. Right, top: The radio star formation rate (see Section 2.3.1) for the star-forming sample colored by the rest-frame u-K color from Laigle et al. (2016). The SF/AGN break is at 2.36, where any object with a color redder than this is a potential radio AGN host (Smolčić et al., 2008; Sargent et al., 2010). The lower panel shows the median offset from the main sequence (as defined by Whitaker et al. (2012)) as a function of redshift.

catastrophic outliers ($|z_{\mathrm{phot}} - z_{\mathrm{spec}}|/(z_{\mathrm{spec}} + 1) > 0.15$) in a comparison with the available spectroscopic redshifts ($Q_f \geq 3.5$) of M. Salvato's COSMOS compilation and were dropped from the sample. Next, we identify the galaxies that likely contain an AGN.

Any AGN identified in the COSMOS field in previous works were removed; for this we utilised the COSMOS-team internal collation of all known AGN in COSMOS (as of March 2012) produced by M. Brusa (Section 2.2.3). In the final 822-member IR-radio comparison sample we identified 87 IR, 23 optical and 39 X-ray AGN, for a total of 127 known AGN once multi-wavelength detections were accounted

for. In addition, we identified a further 46 X-ray AGN using a luminosity cut of $L_X > 10^{42}\,\mathrm{erg\,s^{-1}}$ for X=0.2-10keV and a spectral index, $\Gamma = 1.4$ as in Civano et al. (2012) from the latest Civano et al. (2016) Chandra release (see Figure 2.1 for a breakdown of the subsets).

The photometry was also used to flag potential radio-only AGN using the Sargent et al. (2010) adaptation of the Smolčić et al. (2008) rest-frame optical color selection. With this color indicator ∼74% of the sample without indication of AGN activity at other wavelengths was flagged as an AGN. Since this would have resulted in a drastic reduction of the comparison sample size and the u-K threshold is a probabilistic SF/AGN selection not well tested beyond z ∼1.3, we retained these redder galaxies in our sample and verified at each analysis step that they do not bias our results. Thus, after quality controls and AGN cuts we are left with a total of 649 star-forming candidate sources that have radio, IR and optical information, shown in Figures 2.1 and 2.2.

2.3 SFR Prescriptions

The star formation rate (SFR) in galaxies is commonly determined through a wide variety of multi-wavelength diagnostics, each with their own intrinsic advantages and disadvantages. Reviews, such as Kennicutt & Evans (2012) touch upon the underlying physics of each of these tracers and describe in detail their strengths and weaknesses. Yet, as stated in the introduction, all of these diagnostics are calibrated in the local Universe. In the following subsections, we describe some of the commonly applied SFR tracers at high redshift, and in particular the radio and IR calibrations we examine in this work.

2.3.1 Tracers of Star Formation

The rest-frame ultra-violet (UV, 1250-2500 Å) is emitted predominantly by young, massive stars and so is a direct tracer of the star formation rate. The short lives of the O and B stars that emit the UV light mean that the UV traces the star formation over the past ∼ 100 Myr. Star formation can be traced on shorter timescales using recombination or forbidden emission lines such as Hα and [OII]λ3727 Å. These are indirect tracers as they arise from gas ionised by extreme ultra-violet

photons ($< 912\,\text{Å}$) emitted by the most massive stars ($> 15\text{M}_\odot$) with very short lifetimes of $< 10\,\text{Myr}$. The main drawback in the use of these UV and optical tracers is the attenuation of the emission by dust (Buat et al., 2005; Moustakas et al., 2006). Dust in the interstellar medium preferentially absorbs at UV and optical wavelengths and re-emits in the mid- to far-IR. In young dusty actively star-forming galaxies, where the majority of stars are formed during the peak of the cosmic star formation history; z ∼1-3 (Madau & Dickinson, 2014), dust extinguishes as much as ∼90% of the optical or UV emission for IR-selected galaxies (Buat et al., 2005). Typically the amount of attenuation is determined through the reddening of the spectrum, either through the UV color or the spectral slope, β, or the Balmer decrement Hα/Hβ and applying an attenuation law (Calzetti, 2001) based on this measured reddening (Reddy et al. (2015) presents high redshift corrections to these). The other commonly used method is to correct for the dust with an IR tracer that measures the amount of absorbed light through re-emission (Hao et al., 2011; Leroy et al., 2012).

A significant fraction ($> 60\%$ in a typical star forming galaxy) of the UV and optical stellar emission is absorbed by dust (Leroy et al., 2012; Hao et al., 2011; Buat et al., 2005), with younger stars being preferentially extinguished due to their proximity to the clouds from which they formed. Thus the IR luminosity is an excellent tracer of the SFR in most star forming galaxies. Possible contamination of the IR emission through dust heating by older stellar populations ($> 100 - 300\,\text{Myr}$) can lead to an overestimation of the SFR (Kennicutt & Evans, 2012; Leroy et al., 2012; Groves et al., 2012), particularly at the longer FIR wavelengths in galaxies with lower sSFRs.

Often sufficient wavelength coverage to determine the total IR luminosity is not available, particularly to sample near the peak of the IR spectral energy distribution (typically $\sim 100\,\mu m$ in the rest-frame) and the intrinsic IR luminosity of the galaxy is extrapolated from a single band. While Elbaz et al. (2010, 2011); Magdis et al. (2012); Kirkpatrick et al. (2012); Murphy et al. (2009) have shown this to be a reasonably reliable method out to at least $z \sim 1$, uncertainties remain on the variations with both redshift and luminosity. The MIPS $24\,\mu$m is the band of choice given its higher spatial resolution and sensitivity, although for galaxies lying at $z \gtrsim 1$ (particularly at $z \sim 2$ when the strongest emission feature, at $8\,\mu$m, shifts into the band) this band is affected by contamination from emission arising from

polycyclic-aromatic-hydrocarbons (PAH) which dominate the rest-frame 5-20 μm spectra of galaxies (Elbaz et al., 2011).

Another SFR tracer that is unaffected by dust attenuation is the radio continuum, a combination of thermal free-free emission arising from gas ionized by the EUV photons of young stars, and synchrotron, or non-thermal, emission arising from the interaction of cosmic rays, which originate mostly from the supernovae of massive stars, with galactic magnetic fields (Condon, 1992). This calibration, while in principle tracing young massive stars, relies mostly upon the empirical correlation between the radio continuum and the total IR emission (the infrared-radio correlation, or 'IRRC'). This well known, tight (scatter of factor 1.5) empirical relation holds over five orders of magnitude in luminosity (e.g Bell, 2003; Yun et al., 2001). This means that the radio continuum traces the same timescales of star formation as the infared. In the 1.4 GHz band, which is typically used to trace the radio continuum, synchrotron emission dominates, but as one moves to higher rest-frame frequencies, the thermal free-free emission starts to contribute significantly, dominating above ~30 GHz (Murphy et al., 2011).

2.3.2 Murphy et al. (2011) SFR Calibrations

SFR calibrations rely upon assumptions to convert the observed tracers to the mass of stars formed, such as the initial mass function (IMF) of stars (Wilman et al., 2008). To avoid issues of different assumptions between the calibrations, we use the self-consistent locally-calibrated SFR diagnostics of Murphy et al. (2011). They used the Starburst99 (Leitherer et al., 1999) stellar population synthesis code assuming a Kroupa IMF (Kroupa, 2001), solar metallicity and constant star formation over a 100 Myr timescale.

The Starbust99 UV spectrum was integrated over 912-3646 Å and was assumed to be totally absorbed by dust and re-emitted in the IR (taken to be optically thin) to obtain the relation between SFR and total IR luminosity. The TIR luminosity was obtained by fitting model IR spectral energy distributions (in the case of Murphy et al. (2011) these are the Dale & Helou (2002) models) to the available IR bands[6]. The Murphy et al. (2011) assumptions lead to;

[6]For details on the dataset used for the comparison see Murphy et al. (2011).

$$\mathrm{SFR_{IR}\,[M_\odot\,yr^{-1}]} = 3.88\ \times 10^{-37}\,L_{\mathrm{TIR}}\,[\mathrm{W}], \tag{2.1}$$

where L_{TIR} is integrated over the 8-1000 μm dust continuum.

For the 1.4 GHz radio continuum SFR, Murphy et al. (2011) made use of the IRRC (de Jong et al 1985, Helou et al. 1985);

$$q_{\mathrm{TIR}} \equiv \log \frac{L_{\mathrm{TIR}}\,[W]}{3.75 \times 10^{12}\,L_{1.4\mathrm{GHz}}\,[W\,Hz^{-1}]} \tag{2.2}$$

assuming a $q_{\mathrm{TIR}} = 2.64 \pm 0.26$ as in Bell (2003). Combining this with Equation 2.1 then leads to the following radio-SFR relation;

$$\mathrm{SFR_{1.4GHz}\,[M_\odot yr^{-1}]} = 6.35 \times 10^{-22} L_{1.4\mathrm{GHz}}\,[\mathrm{W\,Hz^{-1}}] \tag{2.3}$$

To determine the rest-frame 1.4 GHz luminosity from the observed 1.4 GHz flux we assume a power-law radio continuum $S_\nu \propto \nu^\alpha$ with a constant spectral slope α;

$$L_{1.4\mathrm{GHz}} = \frac{4\pi\,D_{\mathrm{L}}^2}{(1+z)^{1+\alpha}}\,F_{1.4\mathrm{GHz}} \tag{2.4}$$

In this work we use $\alpha = -0.8$, a commonly assumed and observed value (Condon, 1992).

Determining the rest-frame 8-1000 μm luminosity from the observed single-band IR photometry is more difficult, as it depends upon the shape of the IR spectral energy distribution, of which many models exist.

2.3.2.1 SED Fitting for L_{TIR}

When the available photometry for a particular sample is limited, it is often necessary to use templates of the IR spectral energy distribution (SED) of galaxies to extrapolate the missing flux and to create a smooth, uninterrupted spectrum, or indeed to extrapolate for the total IR from a monochromatic IR measurement. These templates are generally based on theoretical models in order to obtain a smooth and continuous spectrum and then calibrated against well sampled SEDs of nearby galaxies to pin down the values of the model parameters.

Creating a model SED relies on many assumptions to relate the shape of the IR energy distribution of a galaxy to the physical process at work within. The dust components are modelled as modified (to account for the emissivity of the dust) black bodies with the model parameters[7] being fixed by observation of local galaxy samples (Dale & Helou, 2002; Chary & Elbaz, 2001). The rest-frame near infrared (NIR), at 0.8 to 3 μm, is made up of the tail end of the stellar emission. In the mid-IR (3-40 μm), the warm (>50K) dust surrounding star-forming regions produces a continuum with polycyclic-aromatic-hydrocarbons (PAH) emission features. These PAH features, seen in the 3 μm-12 μm range, in addition to weaker features at 11 μm-15 μm can account for up to 20% of the total IR luminosity in a normal star forming galaxy (Smith et al., 2007). In addition, the hot (>100 K) dust of an AGN torus can contribute an additional continuum to the mid-IR SED at shorter wavelengths (Kirkpatrick et al., 2012) which drops off steeply at 20 μm and a 9.7 μm silicate absorption feature. The far-IR (40-850 μm) is dominated by the thermal emission of cool (∼15-20 K) dust that is being heated by the underlying galactic stellar population and typically peaks somewhere around 100 μm (Kirkpatrick et al., 2012). The cool dust component makes up the bulk of the dust mass in a normal star forming galaxy, although the warm dust can be responsible for up to half of the bolometric IR luminosity (Dale et al., 2007, 2012; da Cunha et al., 2010).

At high redshifts (beyond z ∼0.5) where there is insufficent data of high enough resolution or sensitivity on star forming regions within galaxies to develop models of the ISM, most studies rely on empirically derived templates (Kirkpatrick et al., 2012). In such cases high quality multiwavelength coverage spanning the mid-IR to beyond the peak of the far-IR is necessary.

The bulk of star formation occured at $z \sim 1-3$ in LIRGs and ULIRGs (Caputi et al., 2007; Magnelli et al., 2011), which have $10^{11}\,L_{\odot} < L_{TIR} < 10^{12}\,L_{\odot}$ and $L_{TIR} \geq 10^{12}\,L_{\odot}$ respectively. Most local examples of these galaxies are observed to be merger-triggered compact starbursts, however high redshift ULIRGs are observed to have more spatially extended star-forming regions and tend to lie on the main sequence (Elbaz et al., 2011). In fact, Rieke et al. (2009) and Elbaz et al. (2011) find that high redshift LIRGs and ULIRGs have similar SED shapes to local main-sequence galaxies of lower luminosity, in the sense that the PAHs are stronger relative to the continuum and the bulk dust component is cooler. In addition,

[7] $T_{\rm dust}$ and the normalization and emissivities for each component.

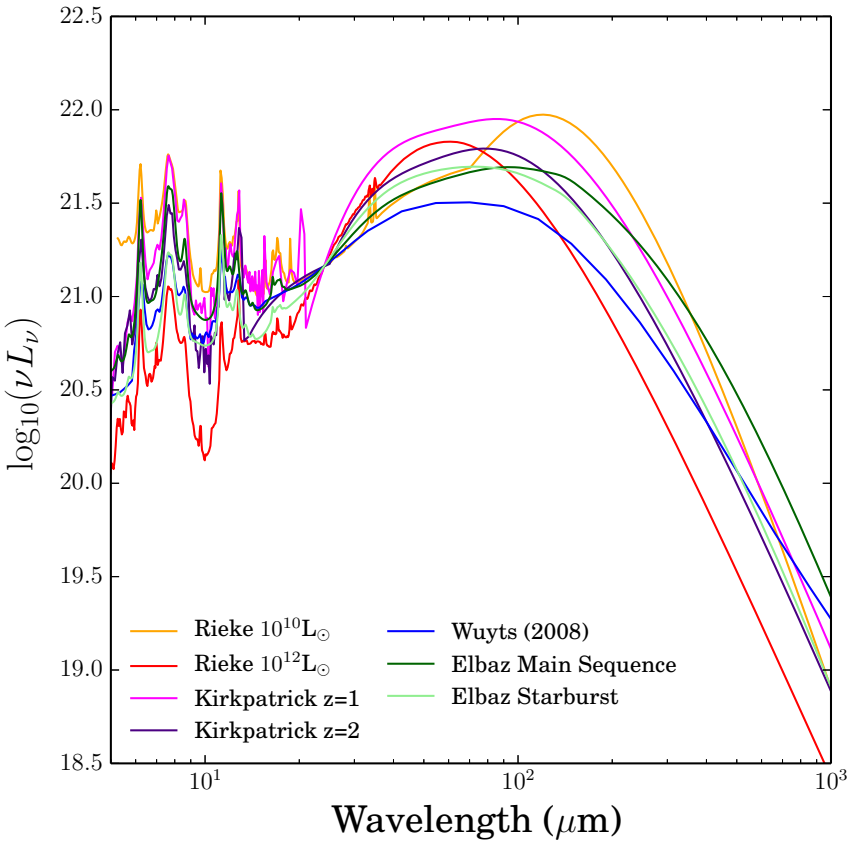

FIGURE 2.3: A cross section of some of the SEDs used in this work, from locally calibrated (Rieke et al., 2009; Wuyts et al., 2008) to empirical high-redshift templates (Kirkpatrick et al., 2012; Elbaz et al., 2011). The SEDs are normalized at 24 μm.

locally, $L_{\rm IR} > 10^{12}\,{\rm L}_\odot$ galaxies are very rare and there is significant variation in PAH features as a function of bolometric IR luminosity – it can be as much as an order of magnitude across all galaxy types and luminosities, in particular for the rest-frame 8 μm (Kennicutt et al., 2009). All these factors conspire to make it difficult to determine with a reasonable degree of accuracy the correct form of the IR SED (and hence the SFR) at high z, at least on a galaxy-by-galaxy basis.

Many of the IR SED templates currently in favour have significant overlap, in Figure 2.3 we plot a subset of these templates that represents both the most commonly used ones and the range of possible templates in the literature (see Appendix A for a full comparison of all the IR SEDs). These templates can be roughly classified into two categories; locally calibrated models (Chary & Elbaz, 2001; Dale & Helou, 2002; Rieke et al., 2009) and empirically derived high redshift templates (Kirkpatrick et al., 2012; Elbaz et al., 2011; Magdis et al., 2012). The

details of the construction of these model IR SED templates are decribed in the following:

- Dale & Helou (2002): An update of the Dale et al. (2001) models. Dale et al. (2001) used IRAS, ISOCAM and ISOPHOT data of 69 local, normal, star-forming galaxies to constrain the theoretical models of Desert et al. (1990), who assume a power law distribution of the heated dust masses with intensity $\mathrm{d}M(U) \sim U^{-\alpha}\,\mathrm{d}U$. Dale & Helou (2002) constrain the dust emissivity better beyond 100 μm with additional SCUBA, IRAS and ISOPHOT observations for 114, 228 and 15 galaxies repectively. The SEDs cover the wavelength range 3 μm-1000 μm and luminosities from $10^8\,\mathrm{L}_\odot$-$10^{12}\,\mathrm{L}_\odot$ (or α=0.0625-4).

- Rieke et al. (2009): Measurements covering 5 μm -30 cm, based upon a combination of Spitzer (IRAC, MIPS) and IRAS data for a set of 11 local LIRGs and ULIRGs were used to contruct empirical templates for the sample members; the coverage gaps in the NIR and FIR were filled by a theoretical model of Bruzual & Charlot (2003) and by fitting a single-temperature black body spectrum respectively. The 11 templates were used to investigate trends of L_{IR} with rest-frame colors. For $L_{\mathrm{TIR}} > 10^{11}\,\mathrm{L}_\odot$, the empirical SEDs were combined in weighted averages to create templates representative of the full local LIRG and ULIRG population. Below $10^{11}\,\mathrm{L}_\odot$, where monochromatic color-L_{TIR} trends broke down, they used their methodology on the templates of Dale & Helou (2002). The final set of SEDs spans $5{\times}10^9\,\mathrm{L}_\odot < L_{\mathrm{TIR}} < 1{\times}10^{13}\,\mathrm{L}_\odot$ but it should be noted that beyond $2{\times}10^{12}\,\mathrm{L}_\odot$ they are purely based upon theoretical extrapolations and have large intrinsic uncertainties.

- Chary & Elbaz (2001): Uses publically available data of 90 local galaxies to constrain four models of Silva et al.(1998) – a LIRG, ULIRG, starburst and normal star-forming galaxy. Observed mid-IR and far-IR luminosity trends (using ISOCAM, IRAS and SCUBA data) are employed to interpolate between the four model classes. Additionally, in the FIR Dale et al. (2001) models were used to diversify the range of spectral shapes. The result is a set of templates ranging from $10^{8.4}\,\mathrm{L}_\odot < L_{\mathrm{TIR}} < 10^{13.5}\,\mathrm{L}_\odot$ covering 0.1 μm-1000 μm.

- Elbaz et al. (2011): An averaged main sequence and an averaged starburst template constructed from Herschel PACS and SPIRE observations of a sample of $\sim$ 1500 galaxies out to z=2.5 in GOODS-N and GOODS-S. Galaxies with a rest frame ratio IR8 = $L_{\rm TIR}/L_{8\mu m} > 8$ were considered starbursts (around 20% of the sample) and those distributed around IR8 = 4 were classed as main sequence[8]. For each of the two subsets, galaxies were binned in sample sizes of 25±5 to calculate a sliding median after first normalising the measured SED of each indivdual galaxy to $10^{11}\,{\rm L}_{\odot}$.

- Wuyts et al. (2008): A log-average of the Dale & Helou (2002) models for $1 \leq \alpha \leq 2.5$ (as introduced in the Dale & Helou (2002) discussion). This should be representative of an average local star-forming galaxy on the main sequence.

- Polletta et al. (2007): From this study we make use of the template SEDs for the local starbursts M82 and Arp220. These were generated using the GRASIL code of Silva et al. (1998) and augmented in the MIR (5-12 μm) with ISO observations of the two galaxies.

- Kirkpatrick et al. (2012): Two main sequence empirical galaxy templates; one representative of the average $z = 0.5 - 1.5$ population and the other of the average $z = 1.5 - 2.5$ population. The $z \sim$1 template is created using a sample of 39 galaxies, the $z \sim$2 with a sample of 30. All are well sampled in the 0.3-600 μm rest-frame wavelength range with Spitzer IRAC, MIPS, as well as Herschel SPIRE data and 850 μm and 1.5 mm ground-based observations. The average template is determined by median-binning of the luminosity. Modified black bodies are fitted where appropriate to fill in any gaps in the photometry and interpolate between points.

In the following section we compare the $\rm SFR_{IR}$[9] computed from normalizations of these templates with MIPS 24 μm or PACS 100μm data to $\rm SFR_{1.4GHz}$.

[8]In the IR8 determination, the Polletta et al. (2007) M82 model was used to K-correct the nearest IRS or MIPS band to the rest-frame 8 μm and the models of Chary & Elbaz (2001) were used for $L_{\rm IR}$.

[9]Since our sample consists of highly luminous IR (and hence very dusty) sources we make the assumption that the entire output of the massive young stellar poulation is captured and re-radiated by the dust, i.e that the UV escape fraction and hence any UV-based correction to the $\rm SFR_{IR}$ is negligible. We verified that the assumption is valid for our sources. GALEX NUV and FUV meaurements are available for about half our sample out to $z \sim$1.8. At $z \sim$0.5 where the NUV band is probing the rest frame FUV, we calculated the $\rm SFR_{FUV}$ based on the Murphy et al. (2011) calibration and found it to be well below $1\,{\rm M}_{\odot}\,{\rm yr}^{-1}$.

2.4 SFR Tracer Comparison

2.4.1 IR SFR From Single-Band Normalised SEDs

In order to investigate the robustness of SFR_{IR} extrapolated from a monochromatic band using a universal IR SED on high redshift samples of radio galaxies, we compare the ratio of these SFRs to our chosen fiducial tracer, the 1.4 GHz radio continuum, out to a redshift of 2.3[10]

The TIR luminosities used in the following comparison plots are obtained by integrating the chosen representative SED from 8-1000 μm to obtain the rest-frame total value for the sample, after normalising the SED by either the 24 μm MIPS measurements or the 100 μm PACS measurements; the SFR_{IR} thus obtained are denoted $SFR_{24\mu m}$ and $SFR_{100\mu m}$ respectively.

For our test we select two families of templates that are commonly used (see Section 2.3.2.1): a) locally calibrated ones and b) empirically derived high-z ones. The locally calibrated templates, Rieke et al. (2009) and Wuyts et al. (2008) are based on local samples of (U)LIRGS and normal star forming galaxies, respectively. In the case of Rieke et al. (2009) we chose two from the library; one for 10^{10} $L_\odot$ galaxies, corresponding to our low z luminosity cut-off and a 10^{12} $L_\odot$ template representative of the high luminosities of most of our sample sources. Our considered empirical high-z templates sample main-sequence galaxies (Kirkpatrick et al., 2012) and both main sequence and starburst galaxies (Elbaz et al., 2011). The results of our analysis for all templates are shown in Appendix A.

Radio star formation rates ($SFR_{1.4GHz}$) use the Murphy et al. (2011) calibrations outlined in Section 2.3.2, assuming a constant radio-IR correlation value q_{TIR} = 2.64 and a radio spectral index of α=-0.8.

We plot the redshift evolution of the ratio of the SFR_{IR} to the $SFR_{1.4GHz}$ for our radio-selected star-forming sample in Figures 2.4 and 2.5. Each panel utilises a different 'universal' IR template to extrapolate the total IR luminosity, and hence the SFR_{IR}, from the monochromatic broad-band flux. In Figure 2.4 the MIPS 24 μm measurements are used to normalize the templates and in Figure 2.5 the PACS 100 μm ones are used.

[10]We cut off at z=2.3 since our star-forming sample is limited to 7 galaxies beyond that and since several of the compiled SEDs do not extend blueward enough to probe the observed-frame 24 μm beyond z =2.3.

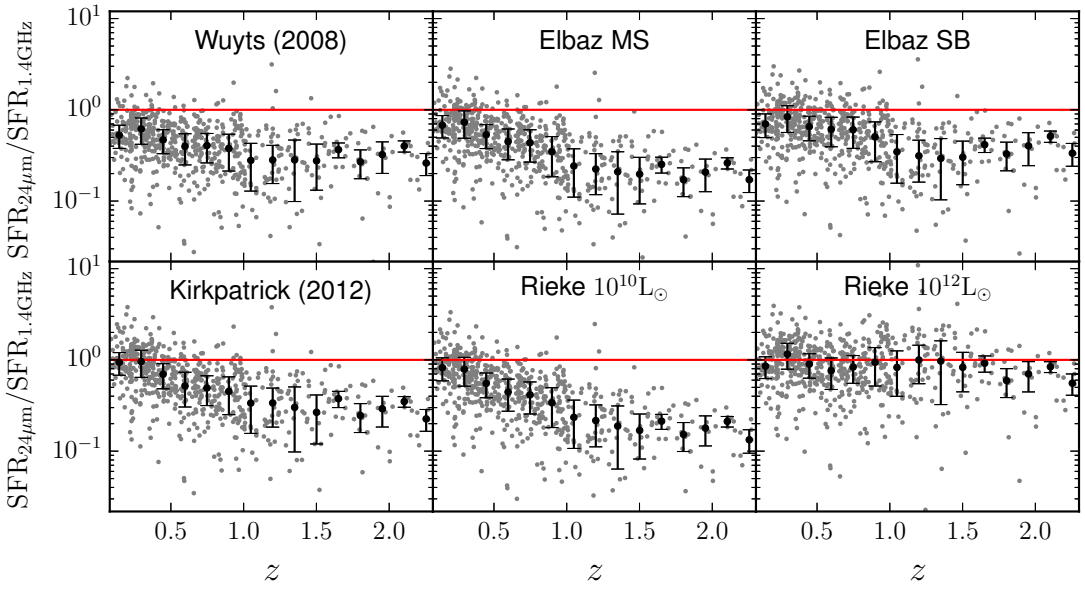

FIGURE 2.4: The ratio of the SFR_{IR} to the $SFR_{1.4GHz}$ as a function of redshift for a representative selection of SEDs normalized by the MIPS 24 μm measurements. In each panel a different SED has been used in the total IR luminosity extrapolation as labelled. The median in redshift bins of width Δz=0.15 is represented by the black points, with error bars corresponding to the absolute deviation from the median ('MAD'). The red line, included here to guide the eye, represents a 1:1 agreement between SFR measures. Regardless of SED template employed, the $SFR_{24\mu m}$ values are systematically lower than the radio ones and exhibit trends with redshift. Similarly, for each SED the scatter is also quite significant. The Rieke et al. (2012) 10^{12} $L_\odot$ template results in a SFR that most closely aligns with the SFR obtained from the 1.4 GHz measurements when the 24 μm band is used to extrapolate for the total IR luminosity.

In the SFR ratio plots of Figures 2.4 and 2.5, given good and consistent calibrations of the IR and radio SFRs, we would expect the data points to lie at a ratio of 1 with scatter consistent with the observational uncertainties. Instead, we observe a general failure of agreement between bolometric SFR_{IR} based on an extrapolation from a monochromatic band with a universal SED and a 1.4 GHz continuum SFR.

In Figure 2.4 the resulting $SFR_{24\mu m}$ from all but one of the SED templates systematically underestimate the SFR in comparison to the radio, with this offset increasing with redshift. Locally-calibrated templates still vary enough in the mid-IR at z=0 to result in differences in the IR and radio SFR medians of up to a factor of 2 (as in the case of Wuyts et al. (2008)) and as much as a factor of 5 beyond $z \sim$1, e.g as in the case of the Elbaz et al. (2011) main sequence template. The dispersion in the SFR ratio shows an SED dependence, with the Wuyts et al. (2008) and Rieke et al. (2009) 10^{10} $L_\odot$ main sequence templates generally showing

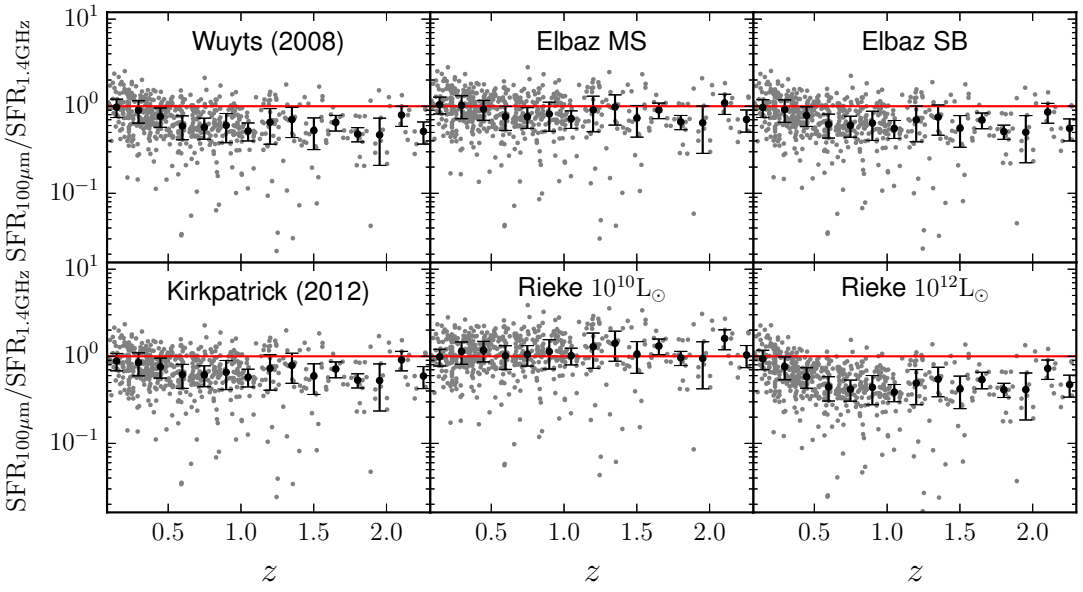

FIGURE 2.5: The ratio of the SFR_{IR} to the $SFR_{1.4GHz}$ as a function of redshift, following Figure 2.4, except normalized by the PACS 100 μm measurements. There is better agreement at low z here than the $SFR_{24\mu m}$ in Figure 4 but the $SFR_{100\mu m}$ still exhibit a redshift trend. The scatter is reduced compared to that in the 24 μm extrapolation, although still significant. Here, the Rieke et al. (2012) 10^{10} $L_\odot$ template results in a SFR that most closely aligns with the SFR obtained from the 1.4 GHz measurements across the full redshift range considered.

the tightest relation at high and low z respectively; Wuyts et al. (2008) having a scatter of about 0.15 in the SFR ratio at z <1 and the Rieke et al. (2009) having a value of ∼0.1 at z=1-1.5. Note that at higher redshifts the low sample numbers make the dispersion estimates unreliable. Interestingly the Rieke et al. (2009) 10^{12} $L_\odot$ template has the greatest dispersion by far of the SED templates, being as much as ∼0.45 and higher in the z =1-1.5 bins. The MIPS 24 μm filter probes the MIR warm-dust region of the galaxy SED where the emission is a function of the intrinsic luminosity of the galaxy and the dust composition and can be contaminated by the presence of an AGN. PAH features shift into this band and it is well known that even at a fixed luminosity there is a large spread in PAH equivalent widths (Figure 2.3), translating into a large spread in SFRs when using this band to normalize our SEDs. We can also see several clear outliers, where the $SFR_{1.4GHz}$ is significantly higher than the IR value and a smaller number of IR excess outliers, we will address these in Section 2.4.2.4. The Rieke et al. (2009) template calibrated for ULIRGs with an intrinsic luminosity of 10^{12} $L_\odot$ is the only SED that provides an $SFR_{24\mu m}$ for our sample that has $SFR_{24\mu m}/SFR_{1.4GHz} \approx 1$, although

the median dispersion can be as high as 0.5 dex. In the two lowest redshift bins the Kirkpatrick et al. (2012) SED does a comparable or better job.

In Figure 2.5, we use the PACS 100 μm band to determine the bolometric SFR_{IR} using the same templates as in Figure 2.4. Similar to $SFR_{24\mu m}$, using PACS 100 μm underestimates the SFR_{IR} as compared to the radio tracer for most SED templates, excluding Rieke et al. (2009) 10^{10} $L_{\odot}$. However this disagreement is smaller (only a factor of 2 for the worst performing SED model, Rieke et al. (2009) 10^{12} $L_{\odot}$ at z >1), and appears constant beyond $z \sim 0.5$. The scatter is model dependent, as in Figure 2.4, with the better fitting SEDs exhibiting larger scatter - as much as 0.3 at z <1 for the Rieke et al. (2009) 10^{10} $L_{\odot}$ and Elbaz et al. (2011) main sequence templates and 0.5 at z ∼1. The improved agreement at 100 μm is expected as the variation between galaxies is less extreme at the longer IR wavelengths probed by the 100 μm band. The variations that do occur are mostly owing to small differences in the dust peak location and height, as is clear in Figure 2.3. The Rieke et al. (2009) 10^{10} $L_{\odot}$ model returns $SFR_{100\mu m}$ that are on average closest in agreement with the $SFR_{1.4GHz}$ across all z, although the Elbaz et al. (2011) main sequence template is also a close match and outperforms this Rieke et al. (2009) template in the z=1-1.5 region. As in Figure 2.4, we are affected by low number statistics and significant outliers in the higher redshift bins.

For our radio selected sample of star-forming galaxies we cannot find a single universal SED template that will produce SFR_{IR} that are consistent with $SFR_{1.4GHz}$ for both the 24 μm and 100 μm photometry across our redshift range. Although for each of the two IR bands we can find a template that gives a SFR_{IR} that agrees on average with the fiducial $SFR_{1.4GHz}$, this SED is not the best for all redshifts. Neither will a chosen template fare particularly well for individual galaxies, given the large scatter about the median we observe in both IR bands for all templates. Whether this scatter is due to flux mesurement errors or is an intrinsic feature of the star-forming sample will be discussed in further detail in Section 2.4.2.2

The redshift evolution of the offsets of the median of the $SFR_{IR}/SFR_{1.4GHz}$ present fundamental challenges to comparisons of the star-forming properties of galaxies at different epochs. A simple global rescaling will not correct the SFR_{IR} calibration and will in fact be model and normalization-band dependent. However, there may be either systematics within our sample or physical effects that we can account for that may ameliorate the observed offsets, scatter and redshift evolution, which we investigate in Section 2.4.2.

2.4.2 Investigating the Offset: Systematics

2.4.2.1 The Radio K-Correction

Figures 2.4 and 2.5 clearly demonstrate that SFRs extrapolated from a monchromatic IR flux assuming the existence of a universal IR SED are very uncertain, and depend not only on the choice of template, but also normalization band. However, it is also possible that the denominator, the SFR determined from the 1.4GHz radio continuum, may suffer systematics that affect the observed offsets and scatter. Here, we consider some factors that may influence the calibration of this benchmark tracer.

Two main assumptions are incorporated into the observed 1.4 GHz flux to SFR conversion: Firstly, that the radio continuum can be modelled by a power law, $S_\nu \propto \nu^\alpha$, with a universal slope for all the galaxies in the sample, which is constant across our considered redshift range. Here, the theoretical value of $\alpha = -0.8$ is utilised to K-correct the observed 1.4 GHz luminosities to the rest-frame value (Equation 2.4). The second assumption is that the empirical IR-radio correlation (IRRC) is linear and constant out to high redshifts with a value of $q_{\rm TIR} = 2.64$, as in Murphy et al. (2011). With this assumption, the radio SFR is simply a q-rescaled version of the bolometric $\rm SFR_{IR}$ (see Equation 2.1 and Equation 2.2). We discuss some of the implications of a deviation from this value of $q_{\rm TIR}$ in Section 2.5, but address here the reliability of the radio K-correction.

To determine the reliability of our assumption of a constant index power-law, we cross-matched our sample with the catalog of Smolčić et al. (in press) using a search radius of 0.5″ (reasonable given the 0.75″ resolution of the 3GHz data). 95% of our star-forming galaxy sample had counterparts in the catalog. The spectral index was determined using the observed 1.4 GHz and 3 GHz fluxes for each galaxy and plotted as a function of photometric redshift in Figure 2.6. The median slope is consistent with a value of $\alpha_{1.4GHz}^{3GHz}$=-0.8 and shows no redshift evolution. This result is in agreement with the finding of Smolčić et al. (in press) who determined the slope for a matched 1.4 GHz-3 GHz sample with direct detections after de-selecting multi-component 1.4 GHz sources (Schinnerer et al., 2010). After applying 'survival analysis' to their much larger 1.4 GHz flux-limited matched sample[11], Smolčić

[11]The 3 GHz catalog is significantly deeper than the 1.4 GHz Joint JVLA of Schinnerer et al. (2010) with a mean rms of 2.3μJy/beam.

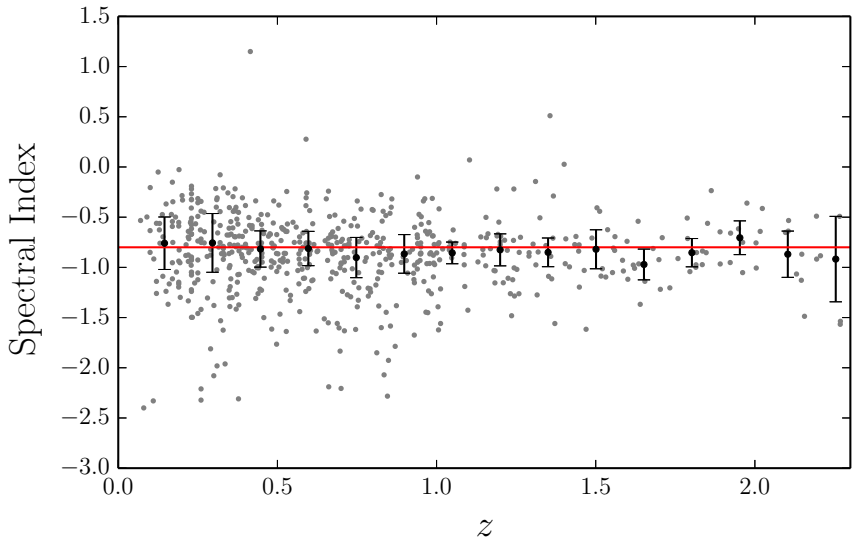

FIGURE 2.6: The radio spectral index (the slope in the 1.4 GHz-3 GHz observed frame regime) as a function of photometric redshift. The 3 GHz flux measurements for our sample are from the catalog of Smolčić et al. (in press). The black points represent the median for these and the error bars the absolute deviation from the median within the bins (of width Δz=0.15). The red line represents the commonly used theoretical value of $\alpha = -0.8$.

et al. (in press) determined a median value -0.73, with a standard deviation of σ=-0.35, which is in good agreement with typical observed values, e.g, as found by Condon (1992).

Using an α value of -0.7 in the calculation of $SFR_{1.4GHz}$ would result in a decrease in the $SFR_{1.4GHz}$ of only $\sim 10\%$ compared with α =-0.8 over most of our redshift range, with a maximum decrease of 15% at the upper end of our redshift range, $z \approx 2.5$. Applying the $\alpha = -1.2$, the $SFR_{1.4GHz}$ would increase by a maximum of a factor of 2 at $z \sim 2$. At the lower end, for the flatter $\alpha = -0.5$ sources, the $SFR_{1.4GHz}$ would decrease by a maximum factor of 2 at $z \sim 2$ in relation to the value obtained with $\alpha = -0.8$.

We have confirmed that the most extreme outliers in our IR-radio SFR comparison are also α outliers. For these outliers we redetermined the radio SFR using the measured $\alpha_{1.4GHz}^{3GHz}$ and found little difference in the overall results. Altogether this indicates that the K-correction of the radio continuum is not a dominant contribution to the disagreement between SFR_{IR} and $SFR_{1.4GHz}$.

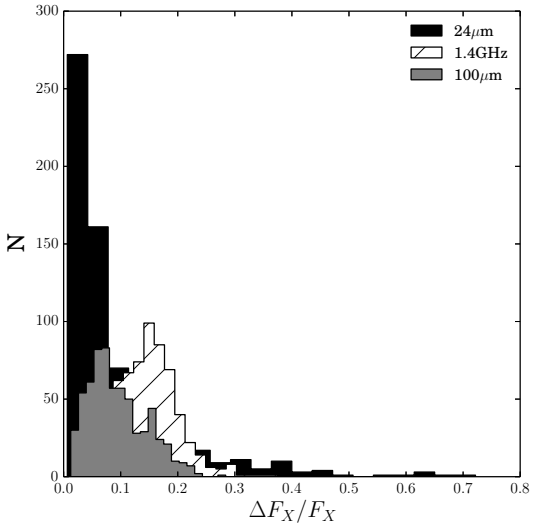

FIGURE 2.7: The distribution of the flux measurement errors for our sample for the three bands of interest in this study; the 1.4 GHz (white hatched), the 24 μm (black) and the 100 μm (gray).

2.4.2.2 IR Colours

In Figure 2.4 an obvious trend with redshift was present in the $SFR_{24\mu m}/SFR_{1.4GHz}$ for most of the SED templates considered. This can be attributed to the fact that at $z = 0.5$ PAH emission features start to shift into the 24 μm band and the SED templates we consider here do not sufficently capture the PAH behaviour of our sample; in fact most of the SEDs are calibrated on main sequence galaxies which have stronger PAH emission (Chary & Elbaz, 2001; Dale & Helou, 2002; Elbaz et al., 2011) than the Rieke et al. (2009) 10^{12} $L_\odot$ ULIRG template that best fits our datapoints. PAH emission is complex to model and emission can vary by an order of magnitude or more between local galaxies (Chary & Elbaz, 2001; Dale & Helou, 2002). In the $SFR_{100\mu m}/SFR_{1.4GHz}$ evolution with redshift was much less noticeable, merely down to differences in the location and width of the emission peak of the cool bulk of the ISM dust between model templates - this generally only leads to differences of a factor of 2 in L_{TIR} estimates from a monochromtaic FIR band. In both cases we saw significant scatter in the $SFR_{IR}/SFR_{1.4GHz}$, here we address this scatter and whether it can be attributed to flux measurement errors, or is an intrinsic property of our galaxy sample.

In Figures 2.4 and 2.5 we saw a large dispersion in the SFR ratios, even at the lower redshifts. We wish to confirm that inaccurate radio flux measurements are not reponsible for the scatter, we present in Figure 2.7 a histogram of the flux

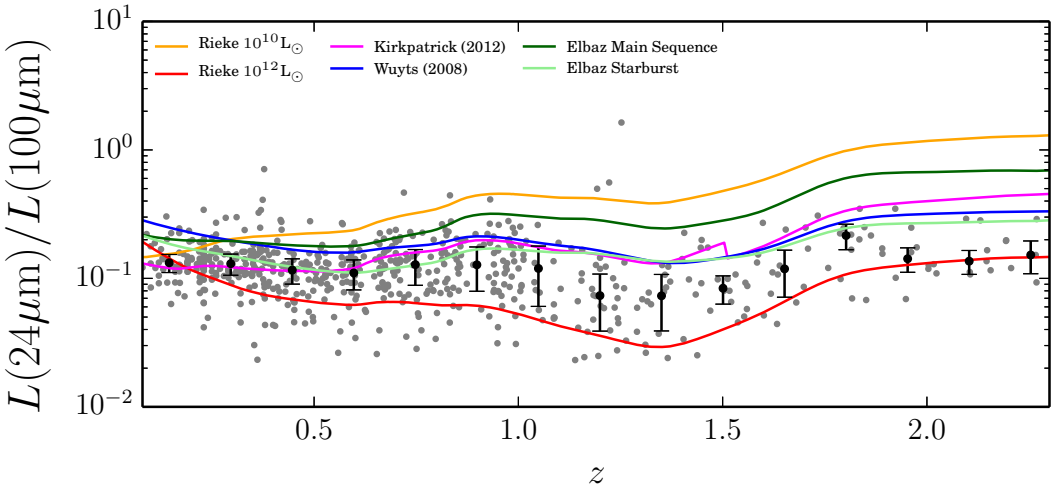

FIGURE 2.8: The 24 μm-100 μm color ratio: The gray points are the ratio of the measured νL_ν at 24 μm and 100 μm; $L(24\,\mu\text{m})$ and $L(100\,\mu\text{m})$ respectively, for our star-forming sample (with the median and MAD in black). The colored lines represent the ratios from the SED models considered.

measurent errors for both IR bands and the 1.4GHz band. The 1.4GHz mean errors are greater than that of the two IR bands, but the MIPS 24μm does have a long tail towards high values. It should be noted that it is only the 100 μm band whose errors show any real z-dependence- they tend toward higher average values with z (note that in the case of the 24 μm all the largest uncertanties are in fact at the lower redshifts). We investigated the errors on the $\text{SFR}_{\text{IR}}/\text{SFR}_{1.4\text{GHz}}$ due to flux measurement errors for individual galaxies in our sample and found that for the vast majority of our star-forming galaxies, the errors are less than the dispersion, most by a factor of two or more, meaning that there is a significant intrinsic component to the scatter about the medians.

In Figure 2.8 we plot the $L(24\,\mu\text{m})/L(100\,\mu\text{m})$ measured as a function of z and compare it to the values obtained from the IR templates, thus we can remove the radio calibration and any uncertainties therein from the analysis and check how much an intrinsic dispersion in the MIR and FIR colours of the star-forming population will affect the extrapolation of the SFR_{IR} from a single monochromtaic band. This figure demonstrates how well the shape of the SEDs considered here match that which would be needed for our sample. Our galaxy population exhibits a large scatter in IR colors at fixed z, ranging from a dispersion of 0.02 at z =0.1 to 0.035 at z ~1-1.5. The IR flux measurement errors are significantly smaller than the dispersion for most of the sample, confirming that the scatter is intrinsic.

Although the extent of the scatter is spanned by our chosen template set, no one template reproduces the redshift trend; at low redshifts (z <0.4), where the most luminous ULIRG galaxies are not dominating the population and we are relatively close to the main sequence and PAH features have yet to shift into the 24 μm band, the Kirkpatrick et al. (2012) main sequence template has the color most similar to our sample, beyond that out to z ~1 the Elbaz et al. (2011) starburst reproduces the colors best. At the higher redshifts the Rieke et al. (2009) $10^{11.74}$ $L_{\odot}$ SED performs relatively well, as does the Polletta et al. (2007) M82 SED (see Appendix A). Note that the dip at z ~1.3 is where the 9.7 μm silicate absorption feature shifts into the 24 μm band. This feature is enhanced towards obscured AGN and compact nuclear starburst regions where the dust opacity is extremely high. Both AGN and nuclear starbursts are likely the cause of the Elbaz et al. (2011) starburst template's failure to fit in this region, given that the flux limitation at high redshifts biases the sample to very luminous starbursts (Section 2.4.2.5) and possibly hosting obscured AGN (Section 2.4.2.4).

Since the method of extrapolating the SFR of a population of galaxies with a single SED hinges upon the assumption that there is not too much spread in the instrinsic properties of the (locally-selected) sample, it is clear that no universal SED can perform well for individual members of this population of high redshift radio galaxies. In addition, since the comparison in Figure 2.8 is independent of any of the assumptions inherent in the calibration of the SFR tracers, the fact that no SED can reproduce the average colors either is suggesting that our sample make-up consists of an atypical population of galaxies when compared to that used in the determination of the existing models.

2.4.2.3 Redshift Misclassification

In Section 2.4.2.2 we accounted for the contribution of (flux) measurement errors to the SFR disagreements, but disregarded the contribution of the photometric redshift uncertainties. Photo-z calculations depend on the set of SED templates used, the accuracy of the flux measurements used in the fitting, the internal workings of the χ^2 fitting code and the chosen spectral-z comparison set, among others. Systematics are often introduced into photo-z determinations; Laigle et al. (2016) found it necessary to apply an overall i^+ band magnitude-dependent correction to

their photo-z, to correct for systematics possibly introduced by their SED template set choice.

To account for any possible contribution of photo-z systematic uncertainties to the SFR offsets seen in Figures 2.4 and 2.5 we reproduced the IR-radio SFR tracers analysis of Section 2.4.1 using the subset of our final star-forming sample with high quality spectroscopic redshifts ($Q_f \geq 3.5$ as discussed in Section 2.2.2). This limits our sample to 275 galaxies. This subsample still shows both the offset and significant scatter, although the spec-z sample is very limited beyond $z \approx 1$ (only 7% of our spec-z subsample). This suggests that the photometric redshifts and uncertainty are not the major contribution to the observed offset and scatter in the SFR tracer ratio.

2.4.2.4 AGN Contamination

Radio and IR wavelengths are unaffected by dust attenuation, thus in the absence of AGN activity, they should both be unbiased tracers of the SFR (as outlined in Section 2.3.1). In Section 2.2.4 we removed all AGN classifed through the multiwavelength analysis of the COSMOS data. These included AGN hosts selected on the basis of their X-ray or IR luminosity and optical lines. We also used the latest Chandra Legacy catalog (Civano et al., 2016) to update the X-ray AGN candidates and cut the classical high-power radio AGN from our sample (those with $L_{1.4\mathrm{GHz}} > 10^{26}\,\mathrm{W\,Hz^{-1}}$, which only amounted to one galaxy in our sample). We are most concerned here with IR and radio AGN, since if they contribute significantly to the galaxy emission at these wavelengths we can mistakenly attribute this emission to star formation and thus bias SFRs towards higher values.

There is very little overlap between the radio AGN and IR-selected AGN populations, with radio AGN residing more in luminous red sequence (early-type) galaxies and IR AGNs preferentally hosted in less luminous blue or green galaxies (Hickox et al., 2009). Smolčić et al. (2008) used such evidence to develop a rest-frame optical color statistical selection for radio AGN hosts at lower luminosities and intermediate redshifts ($z \leq$1.3). This work was done with the VLA-COSMOS Large Project source catalog (Schinnerer et al., 2007) and found that roughly 30-40% of the sub-mJy (below $S_{1.4\mathrm{GHz}}$ =1 mJy) 1.4 GHz radio population could be classed as star forming, 50-60% as AGNs and some minor contribution from QSOs. Here we use the Sargent et al. (2010) version of this 'P1' color selection adapted to u and K

bands, which better suits a sample that is selected in the radio and IR, and should be less likely to confuse dust-reddened star-forming galaxies with red early-type AGN hosts. In the Sargent et al. (2010) work galaxies with rest-frame (u-K)>2.36 are AGN hosts and those with (u-K)≤2.36 are star forming; see Figure 2.2 for their distribution in redshift and radio luminosity.

As mentioned in Section 2.2.4 we chose not to cut these optically selected AGN hosts due to the statistical nature of the selection. Here we check that including the redder (u-K) galaxies in our sample does not bias our results by separating our sample into the 'radio AGN', those with (u-K)>2.36, which amounts to 479 galaxies and a cleanest star-forming sample of 170 galaxies with (u-K)≤2.36. We repeated the IR and radio SFR comparison of Section 2.4.1 with the latter sample and found little evidence of AGN contamination biasing our results. The best fit in the 100 μm normalization case is less clear, but can be attributed to the fact that the difference between the SFR_{IR} from different SEDs when normalising with this band is smaller than when using the 24 μm band (this is quite clear in the presentation in Appendix A). Although the sample numbers are low for our 'cleanest' star forming sample the scatter in the IR colors remains large and points to the fact that a diverse range of IR SEDs is still needed. We can also reasonably speculate that any extreme outliers in Figures 2.4 and 2.5 plots are AGN that slipped though the detection net, based on their (u-K) colors and spectral indices.

We have focused here on radio AGN, since we have, to the best of our knowledge removed all the IR AGN. However Elbaz et al. (2010) have found that a majority of IR AGNs at z<1.5 show similar dust temperatures and IR properties to purely star forming galaxies of similar luminosities, and host significant star formation (10-100s $M_{\odot}\,yr^{-1}$) which dominates the total IR emission. Any AGN contribution to the IR will most affect the shorter wavelengths, we can see that Figure 2.4 has more outliers above 1:1 than Figure 2.5, these are thus likely to be galaxies hosting IR AGN missed in our earlier AGN-deselection.

2.4.2.5 Sample Selection Bias

The robustness of the single-band extrapolation to the total IR luminosity using a single SED, is predicated upon the idea that a single 'universal' SED can sufficently represent all members of an appropriately selected galaxy sample at all redshifts. This was indeed found to be the case locally by Wuyts et al. (2008) and out to

higher redshifts by Elbaz et al. (2011), Kirkpatrick et al. (2012) and Magdis et al. (2012) for SFR − M_* main sequence galaxies and even for starbursting galaxies, although with much higher uncertainties. Our radio-selected sample, with 5σ detections at 20cm and in two IR bands, is severely flux-limited. The fact that we require two IR detections impacts our color range as a function of z and the 50 μJy depth of the Schinnerer et al. (2010) JVLA-COSMOS survey ensures that at all but the lowest redshift bins of our sample are dominated by ULIRGs[12], as can be seen clearly in Figure 2.2, and thus that our sample consists of extreme star-forming systems which are not common locally (Le Floc'h et al., 2005; Smolčić et al., 2008). However, we are generally less concerned with the average luminosity (or SFR) of our sample increasing with redshift (as we move towards the peak of cosmic star-formation density) than we should be with the evolving population makeup, i.e, that we move further off the main sequence of star forming galaxies with z; Figure 2.9.

The flux limitations of our sample thus introduce two biases which need to be addressed. The first is that we are biased to higher luminosity galaxies at higher redshifts. This could be an issue given that Elbaz et al. (2011) have shown that high redshift ULIRGs are dissimilar to their local counterparts. The second bias is linked to the first - the high luminosity bias results in an evolution off the star-formation main sequence with redshift. Elbaz et al. (2011); Magdis et al. (2012); Kirkpatrick et al. (2012) found evidence that main sequence galaxies and star-bursting galaxies can be represented by universal SEDs across a wide redshift range, however, here the relative contributions of these two classes to our sample evolves with redshift.

We address the flux-limitation bias by considering a larger sample of 1044 galaxies with 5σ 1.4 GHz and 24 μm measurements, but no restrictions on the shallower 100μm band. We reproduced the SFR_{IR} and $SFR_{1.4GHz}$ comparisons for this deeper sample and found little difference in the results. This was not unexpected given that it is the 1.4 GHz band that is the shallowest of the three.

To consider the effects of the increasing deviation from the main sequence with redshift, we defined $R_{SB} = sSFR/sSFR_{MS}$ and plot this as a function of redshift in Figure 2.9. We calculate the sSFR for the sample using the $SFR_{1.4GHz}$. The $sSFR_{MS}$ is based on the Whitaker et al. (2012) formulation which incorporates

[12] We are LIRG dominated at z <1 (66%), at higher redshifts the entire population is $> 10^{12}$ $L_\odot$

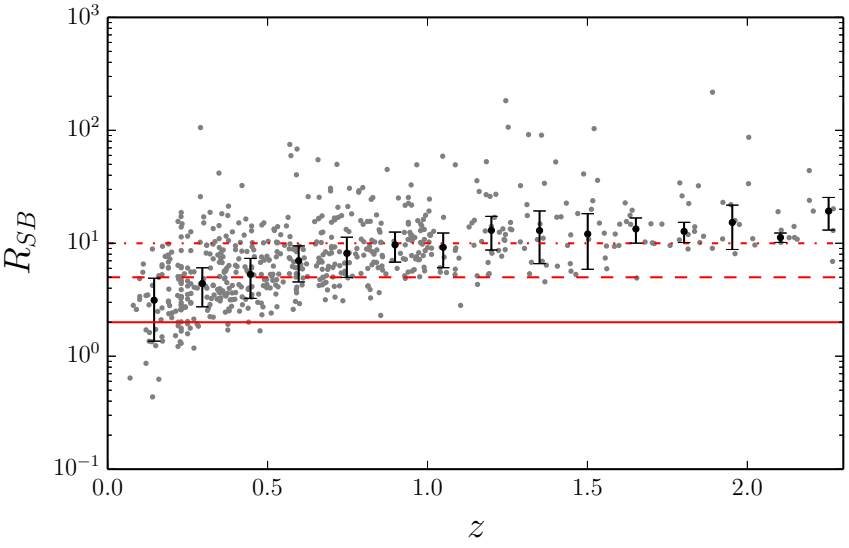

FIGURE 2.9: The starbursting parameter R_{SB} = sSFR/sSFR$_{\rm MS}$ for our sample of galaxies as a function of redshift. The solid red line marks the R_{SB} = 2 boundary above which galaxies are considered starbursts, only 28 galaxies are main sequence here. The dashed and the dash-dotted lines mark the R_{SB}=5 and 10 boundaries respectively. The sSFR for our galaxies was calculated using the SFR$_{\rm 1.4GHz}$ and the sSFR$_{\rm MS}$ using the Whitaker et al. (2012) definition. Stellar masses are from the Laigle et al. (2016) catalog.

mass and redshift evolution[13]. Following Elbaz et al. (2011) $R_{SB} > 2$ is considered a starburst.

We split our sample into three subsets based on their offset from the main sequence; $2 < R_{SB} \leq 5$, $5 < R_{SB} \leq 10$ and $R_{SB} > 10$ (159, 232 and 230 galaxies respectively), that is mild-starburst, medium-starburst, and extreme-starburst galaxies[14]. We then repeated the analysis of Section 2.4.1 for each subset. Yet even when the sample is broken up into these three classes, we find systematic offsets of the SFR$_{\rm IR}$/SFR$_{\rm 1.4GHz}$, which is both dependent upon redshift and the normalization band. Although the sample numbers are now quite low, and in the case of the mild-starburst sample we are mostly limited to $z < 1$, the best performing templates for the two IR bands are often as before - the Rieke et al. (2009) $10^{12}\,L_\odot$ template for SFR$_{24\mu\rm m}$ and the $10^{10}\,L_\odot$ or the Elbaz et al. (2011) main sequence template for SFR$_{100\mu\rm m}$ - with offsets similar to those seen in Section 2.4.1 for the other SED templates.

[13]The masses of our sample are consistent with the charcteristic masses of star-forming galaxies $10^{10.6\pm0.4}\,M_\odot$ (Karim et al., 2011)

[14]Only 28 galaxies in the sample were main sequence, $R_{SB} \leq 2$, and they were concentrated at $z < 0.5$, where they made up at most 11% of the population in that redshift bin

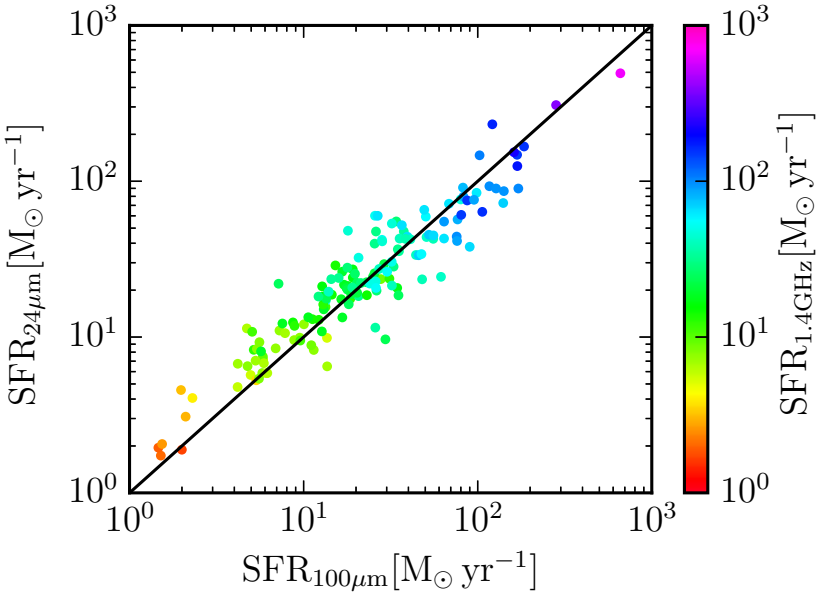

FIGURE 2.10: $\mathrm{SFR}_{24\mu\mathrm{m}}$ vs. $\mathrm{SFR}_{100\mu\mathrm{m}}$ for the 159 galaxies with $2 < R_{SB} < 5$, where the Elbaz et al. (2011) starburst SED has been used to calculate these SFR. The colorscale is the $\mathrm{SFR}_{1.4\mathrm{GHz}}$. All SFR units are in $\mathrm{M}_\odot\mathrm{yr}^{-1}$.

However there are some interesting caveats: In the case of the $R_{SB} \leq 5$ subsample, which extends to z =1.5, the Elbaz et al. (2011) starburst template does produce $\mathrm{SFR}_{\mathrm{IR}}$ that are broadly consistent for the two IR bands and in agreement with the $\mathrm{SFR}_{1.4\mathrm{GHz}}$ as seen in Figure 2.10[15]. The success of the Elbaz et al. (2011) starburst template for the mild starbursts stems from the fact that they had created their starburst IR SED with a Herschel-based sample of galaxies with a similar cut in R_{SB} (note that this template is similar in form to the Chary & Elbaz (2001) $6 \times 10^{11}\,\mathrm{L}_\odot$ template). In the case of the most extreme starbursts ($R_{SB} > 10$), although the Rieke et al. (2009) $10^{12}\,\mathrm{L}_\odot$ lies the closest to $\mathrm{SFR}_{24\mu\mathrm{m}}/\mathrm{SFR}_{1.4\mathrm{GHz}}$=1 and is the only one to show a redshift independent median[16], it is now offset to a value of $\approx 0.62 \pm 0.25$, indicating that these galaxies could have lower PAH than a local $10^{12}\,\mathrm{L}_\odot$ ULIRG or that the $\mathrm{SFR}_{1.4\mathrm{GHz}}$ calibration is incorrect for this subpopulation.

Our flux limit results in a sample of star forming galaxies that is increasingly

[15] We did test the Elbaz et al. (2011) starburst SED on a sample with $R_{SB} < 7$ (amounting to 304 galaxies) but found that the inclusion of the extra, more extreme, objects skewed the sample on average towards higher values of $\mathrm{SFR}_{1.4\mathrm{GHz}}$.

[16] Note that for $\mathrm{SFR}_{100\mu\mathrm{m}}/\mathrm{SFR}_{1.4\mathrm{GHz}}$, although Rieke et al. (2009) $10^{12}\,\mathrm{L}_\odot$ is the worst peformer, its median is flat (unlike in Figure 2.5 for the full sample) and taking a value of $\approx 0.42 \pm 0.16$.

offset from the main sequence with redshift. Our additional requirement of a direct 1.4GHz detection restricts us to extreme starburst galaxies. The IR SEDs of these extreme starburst galaxies do not seem to be well represented by currently available SED template libraries.

2.5 Discussion

It is clear from this analysis that the limited depth of the IR and radio bands results in our galaxy sample to evolve increasingly off the main sequence with redshift. Most of the locally calibrated SED templates currently available do not seem to capture the physics of a high-redshift starbursting population - they cannot produce $\mathrm{SFR_{IR}}$ from MIR or FIR bands that are consisitent with each other or a $\mathrm{SFR_{1.4GHz}}$. We have seen that in addition even an SED template for starbursting galaxies (Elbaz et al., 2011) does not solve the inconsistencies for our full sample since it is dominated by much more extreme starbursts. In Section 2.5.1 we will address the form of the IR SED that our radio-excess starbursts seem to prefer and in Section 2.5.2 summarise some of the current literature regarding a possible evolution in the q_{TIR} with z, which may, when using the $SFR_{1.4GHz}$ as a benchmark in assessing the reliability of SFR_{IR}, lead one to erroneously conclude that IR SEDs evolve with z.

2.5.1 The IR SED Models

In the absence of IR measurements in multiple bands for high redshift galaxy sample it becomes necessary to extrapolate the L_{TIR} from a single monochromatic band using a universal SED template. Chary & Elbaz (2001); Elbaz et al. (2010); Rieke et al. (2009) found galaxies have tight correlations between their MIR and FIR colours and bolometric IR luminosity - particularly for galaxies lying on the SFR-$\mathrm{M_*}$ main sequence. Out to higher redshifts, galaxies have been observed to obey a tight $L_{8\mu m} - L_{TIR}$ in particular (Elbaz et al., 2010, 2011) - an 'IR main sequence'. The early universe was significantly dustier than today, with large gas mass fractions in galaxies that made extended periods of high ($> 100\,\mathrm{M_\odot yr^{-1}}$) SFR possible. In the local low-z Universe, typical galaxies have lower gas and dust mass fractions, with high SFRs only occurring transiently in major mergers. Elbaz et al. (2010) found that at z ~1-2 LIRG and ULIRGs luminosity galaxies have cool dust

temperatures anywhere between 10-20 % cooler than their local counterparts. This result, coupled with the MIR excess problem[17], whereby L_{TIR} for z >1.5 ULIRGs extrapolated from 24 μm in particular were observed to overestimate when using local SEDs Daddi et al. (2007); Papovich et al. (2007); Magnelli et al. (2011), indicated convincingly that high redshift main sequence galaxies are scaled-up versions of local main sequence galaxies (undergoing star formation governed by secular processes) - L_{TIR} for high z ULIRGs can be accurately determined on average with SEDs of local less luminous galaxies.

The results presented in Figures 2.4 and 2.5 would suggest that the high-z starburst population is different to local starburst galaxies. For consistent $SFR_{24\mu m}$ and $SFR_{100\mu m}$ we would require an SED with the MIR shape of a local ULIRG such as the Rieke et al. (2009) 10^{12} $L_{\odot}$, but the FIR shape of a local main sequence galaxy such as the Elbaz et al. (2011) or Rieke et al. (2009) 10^{10} $L_{\odot}$. This is unlike any local SED template; main sequence galaxies tend to have strong PAH and a broad dust continuum peak (Chary & Elbaz, 2001; Dale & Helou, 2002; Rieke et al., 2009) whereas starbursts exhibit weak PAH emission (but often a strong silicate absorption feature at 9.7 μm) and a narrower IR continuum peak at shorter wavelengths. In addition the SFR surface densities in starbursts are typically an order of magnitude greater than would be expected from their projected gas surface densities (Daddi et al., 2010; Genzel et al., 2010), indicating that the star formation region in these galaxies is much more compact than the main sequence case.

Starburst galaxies are quite rare locally and thus poorly modelled, and seem to be associated with interacting or merging systems. At high redshifts it has so far been difficult to associate them with a particular class of galaxies. Given that starburst galaxies are outliers, elevated above both the $SFR - M_*$ and $L_{8\mu m} - L_{TIR}$ (or IR8) main sequences, Elbaz et al. (2011) created a universal starburst IR SED for these galaxies. This was motivated by the fact that they also displayed a $L_{8\mu m} - L_{TIR}$ correlation (although with large scatter) and that IR8 was observed to correlate with compactness of the star-forming region[18]. The success of the Elbaz et al. (2011) starburst SED, which is very similar to a Chary & Elbaz (2001) 6×10^{11} $L_{\odot}$

[17]The MIR excess problem stemmed from the fact that locally ULIRGs are compact major mergers, at high z they are more likely to lie on the main sequence and have much more extended starforming regions, and hence cooler diffuse ISM and stronger PAH emission (Desai et al., 2007) than local ULIRGs.

[18]Indicating that for their GOODS-Herschel sample of galaxies, starbursts at all redshifts are compact major-mergers.

for the milder starbursts (Section 2.4.2.5) template would indicate that this holds true to some extent, but that a significant fraction of the starbursts in our sample are not simply scaled-up versions of local starbursts - if this were the case we would expect one of the local ULIRG templates, such as the Rieke et al. (2009) $10^{12}\,L_{\odot}$ to accurately represent the R_{SB} >5 galaxies. Lacki et al. (2010); Magnelli et al. (2015) advanced the idea that although locally the starburst population consists of compact major-mergers, at z ∼2 the population make-up has evolved to consist of a mixture of 'puffy' starbursts (with cosmic ray scale heights of 1 kpc as opposed to scale heights of 0.1 kpc for 'normal' starburst galaxies of the same luminosity, which are typically submm galaxies, or SMGs) and a non-negligible fraction of 'normal' starbursts. In particular Magnelli et al. (2015) invoked this scenario to explain their observed evolution in the IRRC towards lower values at high redshifts. If our sample is dominated by 'puffy' starbursts, this would result in a more diffuse and possibly cooler bulk ISM and could explain the results of Figures 2.4 and 2.5 and even lead to a evolution of the IRRC towards lower values at higher redshifts.

2.5.2 IR-Radio Correlation

As mentioned in Section 2.3 there is a tight empirical relation between the IR and 1.4 GHz luminosity of a galaxy which persists over five orders of magnitude in luminosity and for many galaxy types. This infrared-radio correlation (IRRC) was historically found to be linear and have values consistent with $q_{TIR} = 2.64 \pm 0.26$ (as in (Bell, 2003) for a set of galaxies with total IR luminosities from $\sim 10^{7.5}\,L_{\odot}$ to $\sim 10^{12}\,L_{\odot}$) for samples of local star-forming galaxies. However recent works by Delhaize et al. (subm.), Magnelli et al. (2015) and Basu et al. (2015) have found evidence of q_{TIR} evolving with redshift. Radio SFR tracers are empirically calibrated: the local L_{TIR}-SFR relation in conjuntion with the IRRC is used to produce a calibration of the $\mathrm{SFR}_{1.4\mathrm{GHz}}$. We have several issues here: the physical mechanisms governing the IRRC are not fully understood and although the L_{TIR}-SFR is investigated in great detail at low z - at high z we lack the IR bands and SED modelling for fully reliable SFR tracer calibrations. Recent observations of q_{TIR} decreasing with increasing redshift means that the $SFR_{1.4GHz}$ will be lower at high z than predicted by the local value of the IRRC.

Delhaize et al. (subm.) examines the IRRC out to $z \sim 5$ on a joint sample of radio-selected and IR-selected star-forming galaxies in COSMOS using new sensitive 3 GHz JVLA observations Smolčić et al. (in press) and Herschel PACS and SPIRE bands. They find q_{TIR} is a decreasing function of redshift $q_{TIR}(z) = (2.90 \pm 0.03)(1+z)^{-0.19\pm0.01}$, with the z =0 value consistent with Bell (2003) and the redshift evolution consistent with Magnelli et al. (2014) and Basu et al. (2015) within the quoted error margins. From their analysis Delhaize et al. (subm.) conclude that the radio spectral index α affects the normalization (moving from a value of -0.7 to -0.8 lowers the normlisation and steepens the z trend) and that it is an incomplete understanding of the radio SED, usually based on M82[19], that is driving the redshift evolution.

We recalibrated our $\mathrm{SFR_{1.4GHz}}$ using this evolving $q_{TIR(z)}$ and found that the normalization is too high for the lowest redshifts; $q_{TIR}(z=0)$=2.9 as compared to the $q_{TIR}(z=0)$= 2.64 in Section 2.4.1. This higher normalization leads to a reduction in the $\mathrm{SFR_{IR}/SFR_{1.4GHz}}$ of ≈ 2. The evolving $q_{TIR}(z)$ can resolve some of the deviations we observe of the lower values of $\mathrm{SFR_{24\mu m}/SFR_{1.4GHz}}$ with increasing redshift. However, an evolving $q_{TIR}(z)$ cannot address the differences between $\mathrm{SFR_{24\mu m}}$ and $\mathrm{SFR_{100\mu m}}$ which arises from the evolution and scatter in the IR colors seen in Figure 2.8. This mismatch between the evolution in IR colors and the SED templates demonstrates that a single template cannot reproduce all galaxy IR SEDs, as well as being affected by the evolving sample make-up (towards more extreme starburst modes at high z). In Figure 2.8 it is clear that the SED template that best reproduces the $L(24\,\mu\mathrm{m})/L(100\,\mu\mathrm{m})$ is dependent upon redshift, which when we consider Figure 2.9, is in turn dependent on the main sequence offset. We saw in Figure 2.10 the Elbaz et al. (2011) starburst template could produce $\mathrm{SFR_{24\mu m}}$ and $\mathrm{SFR_{100\mu m}}$ broadly consistent with $\mathrm{SFR_{1.4GHz}}$, but that for the most extreme starbursts ($R_{SB} > 10$) a local starburst SED (Rieke et al. (2009) $10^{12}\,\mathrm{L_\odot}$) returns $\mathrm{SFR_{24\mu m}/SFR_{1.4GHz}}$ ≈0.62 (and $\mathrm{SFR_{100\mu m}/SFR_{1.4GHz}}$ ≈0.42).

An evolution in the IRRC with SFR could explain this offset and perhaps bring the $\mathrm{SFR_{IR}}$ and $\mathrm{SFR_{1.4GHz}}$ into agreement for the extreme starbursts; q_{TIR} =2.36 would shift the $\mathrm{SFR_{IR}/SFR_{1.4GHz}}$ ratios upwards to bring all three tracers into agreement within the quoted errors for a Rieke et al. (2009) $10^{12}\,\mathrm{L_\odot}$ for these $R_{SB} > 10$

[19]This assumes that the radio spectrum is a combination of two power laws of the form $S_\nu \propto \nu^\alpha$ representing the non-thermal syncrotron emission and the thermal free-free emission with $\alpha_{NT} = -0.8$ and $\alpha_T = -0.1$ respectively. The thermal component is normalized so that it contributes 10% of the rest-frame 1.4 GHz flux

galaxies, although we would caution that the sample numbers are low and this result is fairly speculative. It is however supported by the fact that Tabatabaei et al. (subm.). suggest that the non-thermal (i.e 1.4GHz) IRRC evolves with SFR, rather than z. They use observations of the KINGFISH sample of nearby galaxies to determine that the thermal IRRC[20] will decrease as a function of SFR owing to the amplification of turbulent magnetic fields in star-forming regions (Pannella et al., 2015), which dominate the non-thermal radio emission, affecting the relative IR and radio contributions to the overall energy density and thus manifest as an apparent z evolution in flux-limited samples. Our galaxy sample consists of high $\mathrm{SFR}_{1.4\mathrm{GHz}}$ galaxies even at $z = 0$ and are likely outliers in the Delhaize et al. (subm.) one and hence more sensitive to evolution in luminosity (SFR) rather than z.

2.6 Summary and Conclusions

Different studies determining the evolution of the SFR density over cosmic times have employed a range of SFR tracers. Yet many of these commonly used tracers are calibrated on local samples of galaxies, and the underlying processes may evolve with cosmic time. In order to test the reliability of dust-unbiased SFR tracers we compared two popular methods; the total IR extrapolated from a single MIR or FIR band using a model SED and the 1.4 GHz non-thermal radio continuum. This work was performed on a sample of galaxies in COSMOS out to $z = 2.3$ with $>5\sigma$ 1.4GHz, MIPS 24 μm and PACS 100 μm detections and high quality photometric redshifts using the self-consistent calibrations of Murphy et al. (2011). Importantly, we explore several commonly used IR SED templates to determine the $\mathrm{SFR}_{\mathrm{IR}}$ for this high redshift flux-limited sample. Overall we find a discrepancy between the SFR determined from monochromatic IR observations and that determined from the radio. This discrepancy grows larger with increasing redshift, which corresponds to larger luminosities (where starburst galaxies dominate) in our flux-limited sample.

Individually our findings can be summarized as follows:

[20] They find no apparent evolution in the thermal IRRC with SFR

- For our full, flux-limited sample the SFR_{IR} obtained by normalising SEDs with MIR or FIR measurements are very dependent on the choice of normalization band and template and evolving with redshift, we see offsets of 2 even at $z = 0$ between the SFR_{IR} and the $SFR_{1.4GHz}$ (Section 2.4.1). Therefore we find that the choice of SED and nomalisation band is critical, especially when working with samples of such locally rare galaxies.

- Systematics were found not to be main drivers of the disagreement: The assumed radio spectral index value of $\alpha = -0.8$ for the $SFR_{1.4GHz}$ calibration is consistent with the α_{610MHz}^{3GHz} calculated from a cross match with the 3GHz catalog of Smolčić et al. (in press) - Section 2.4.2.1. The use of photometric instead of spectroscopic redshifts (since many more were available) did not introduce any systematic offsets either (Section 2.4.2.3). In addition, radio AGN contamination was found not to significantly affect the results (Section 2.4.2.4) - although 74 % of our star-forming galaxies are potential radio AGN hosts based on their u-K colors, the 1.4 GHz band used in the radio SFR determination seems to be dominated by emission from star formation.

- As soon as PAH emission features start to shift into the 24μm band at $z \sim$0.5 main sequence SEDs fail to reproduce the IR colors of this sample (Figure 2.8). At higher redshifts, e.g. at $z \sim$1.3 where the 9.7 μm silicate absorption feature shifts into the 24 μm band and the flux limit of the IR and radio catalogs ensures that we are probing extremely IR luminous and dusty galaxies, the SED colors are best represented by the SED of a local compact starburst galaxy such as the Rieke et al. (2009) $10^{11.74}$ $L_{\odot}$ template.

- Requiring 5σ detections in two IR bands and at 1.4GHz limited us to a very extreme subset of starbursting galaxies (Section 2.4.2.5) with a significant intrinsic spread in PAH values (i.e, not dominated by flux measurement errors). This implies that for any universal IR SED that could be constructed for these high-z starbursts, the SFR_{IR} will still be very unreliable for individual galaxies.

- None of the available SED templates had the necessary MIR-FIR shape to return SFR_{IR} consistent with $SFR_{1.4GHz}$, irrespective of IR band used in the L_{TIR} extrapolation. Based on the best matches in Figures 2.4 and 2.5 and SED with the weak PAH emission features of a local starburst galaxy (Rieke et al. (2009) 10^{12} $L_{\odot}$) and the broad FIR peak (and cooler T_{dust}) of a main

sequence galaxy (Elbaz et al. (2011) or Rieke et al. (2009) $10^{10}\,L_{\odot}$). This is in contrast to Elbaz et al. (2011) whose starburst SED was similar in form to a Chary & Elbaz (2001) L_{TIR}= $6 \times 10^{11}\,L_{\odot}$ local starburst model (i.e, it had a narrower continuum peak and hotter T_{dust}^{eff} than we would require here).

- The limited depth of the radio and IR bands ensures that the galaxies in our sample are moving further off the star-forming main sequence with redshift, with the population being dominated by extreme starbursts (R_{SB} >10) at z >1. The starbursts lying closer to the main sequence (R_{SB} ≤5) have an IR SED that is well represented by the Elbaz et al. (2011) starburst template - this produces SFR_{IR} that agree with the 1.4GHz values (Figure 2.10).

- We find that for the extreme starbursts, which given current radio survey depth limits will dominate the $z > 1$ galaxy population unless stacking is employed, no existing SED can represent the MIR-FIR behaviour when we treat $SFR_{1.4GHz}$ as the benchmark SFR tracer (Section 2.4.2.5). However, given that in Figure 2.8 we could find a local ULIRG SED to approximately reproduce $L(24\,\mu m)/L(100\,\mu m)$ at z >1 and the offset in $SFR_{24\mu m}/SFR_{1.4GHz}$ calculated using the Rieke et al. (2009) $10^{12}\,L_{\odot}$ for these extreme starbursts, we would postulate that the $SFR_{1.4GHz}$ calibration needs to be adjusted at high redshift. Delhaize et al. (subm.), Magnelli et al. (2015) and Basu et al. (2015) have presented evidence for an IRRC that evolved with redshift towards lower values, which means that the true $SFR_{1.4GHz}$ for our galaxies would be lower. As discussed in Section 2.5.2 an evolution of the IRRC with SFR rather than z seems more likely here.

We conclude that to obtain reliable SFR values in high-redshift samples of IR and radio bright galaxies one needs to be careful to select by distance from the main sequence; this will influence the choice of the best IR SED for SFR_{IR}. The existing Elbaz et al. (2011) starburst SED will work for those galaxies lying at $R_{SB} \leq 5$ from the main sequence. In any case the SFR values will only be reliable on average, the spread in IR colors, radio spectral indices etc. of these high-z galaxies ensures offsets commonly of 0.5dex, but of as much as 1 dex or more even with the 'best' choice of SED and parameters for individual galaxies.

Although previous authors have found evidence that main sequence SEDs do not evolve appreciably with redshift (Kirkpatrick et al., 2012; Magdis et al., 2012; Elbaz

et al., 2011), and weaker indications that neither do starburst ones (Elbaz et al., 2011), we see evidence that this does not hold true for more extreme radio-selected starbursts. A dedicated effort is needed to understand the dust properties of these high redshift starburst galaxies which dominate the high end of the IR luminosity function. Fully sampled IR SEDs of high z galaxies and hence SED libraries and better understanding of dust properties both on the main sequence and off-main-sequence beyond $z = 1$ along with deeper observations and stacking analyses would help in determining whether there is a z evolution in the ISM properties, or rather whether it is the evolution with SFR that is more important. High-z IR SED libraries will help inform more accuarate SFR for IR selected galaxies, which will be increasingly important when the JWST comes online. Given that radio observations are often deeper and have better spatial resolution than IR and MeerKAT/SKA will find many more of these extreme systems at high redshifts in the near future, it is important to determine the exact nature of the evolution in the IRRC and understand the physical effects driving it, to inform better calibrations of the $\mathrm{SFR}_{1.4\mathrm{GHz}}$. Deep radio observations in multiple bands, so as to capture the rest-frame 1.4 GHz emission and remove the effects of incomplete knowledge of slope of the radio SEDs, as is possible with LOFAR and will be with SKA, will have the potential to determine whether or not q_{TIR} is truly evolving with redshift or with SFR.

Chapter 3

610MHz Continuum Observations of the COSMOS Field with the GMRT

In this chapter the work done towards a 610 MHz image mosaic and catalog of the COSMOS field is presented. This is currently the only survey of COSMOS in this band and will complement the already available 324 MHz, 1.4 GHz and 3 GHz images and catalogs. We present a catalog of 220 5σ sources for the central 1.4 $\deg^2$ of the COSMOS field. Of the 220 sources, 18 have multiple components. The observations were taken with the GMRT array in 2007 and reduced with a pipeline developed by Hans-Rainer Kloeckner[1]. The average rms is 45 μJy/beam with an angular resolution of $8.8'' \times 6.4''$.

The image and catalog for the full mosaic is still being tested and will be made available to the COSMOS collaboration in late Autumn, and a companion paper will be submitted in parallel:
GMRT 610 MHz continuum observations of COSMOS Brady, E., Klöckner, H. R., Schinnerer, E., Karim, A., et al.

[1]This AIPS-based pipeline was specifically developed by HRK to reduce GMRT data for HI stacking on the central deepest pointing of COSMOS. We use it to create a uniform map of the full field for studies of the extragalactic radio population.

3.1 Giant Meter Radio Telescope (GMRT) Observations

The GMRT located in Pune, India consists of 30 fixed-position dishes with diameters of 45 m, giving it three times the collecting area of the VLA and higher sensitivity. It covers a frequency range from 150 MHz to 1.4 GHz. Fourteen antennas are randomly dispersed in a 1 km square central core, with the remaining sixteen arranged in a Y configuration, which has a maximum baseline of 25 km (Swarup et al., 1991) and thus, at best, 4″ resolution at 610 MHz.

The observations of the COSMOS field presented here were taken as part of the projects 10HRK01 and 11HRK01 (PI H.R Klöckner)[2], "Hunting down the cluster population" which had 86 hours allocated over the course of four days in 2006, and eight days in February and March of 2007. The full field was covered by 19 pointings, each being observed for a total of two hours except in the case of the centre-most pointing (referred to a COS01, or P1 throughout this chapter) which was targeted for more than four hours. The phase calibrator chosen for the 2006 observing run was not optimal and thus all those pointings were then revisited during the 2007 run, sacrificing fully uniform coverage of the whole COSMOS field in favour of more homogenous imaging.

3.1.1 Coverage of the COSMOS Field

The COSMOS field is a 2 deg^2 equatorial field centred on R.A.=$10^h00^m28.6^s$ and Dec=+0.2°12′21.0″ (in J2000 coordinates). The primary beam of a single GMRT antenna[3] at 610 MHz has a FWHM of 43′ ± 3′ , thus in order to fully cover the 2 deg^2 COSMOS field with an uniform sensitivity a 19 pointing-mosaic is required.

The pointing centres are arranged in a hexagonal pattern with a 0.405 deg separation, which is approximately 0.56 times the FWHM of the primary beam, as seen in Figure 3.1, for optimally uniform coverage of the field. A detailed discussion on the advantages of this pointing layout is presented in Condon et al. (1998).

[2]The data are publically available on the GMRT archive at https://naps.ncra.tifr.res.in/goa/mt/search/basicSearch

[3]According to the GMRT observer's manual, available at *http* : *//www.gmrt.ncra.tifr.res.in/gmrt$_h$page/Users/doc/obs$_m$anual.pdf* (version 15 January 2015).

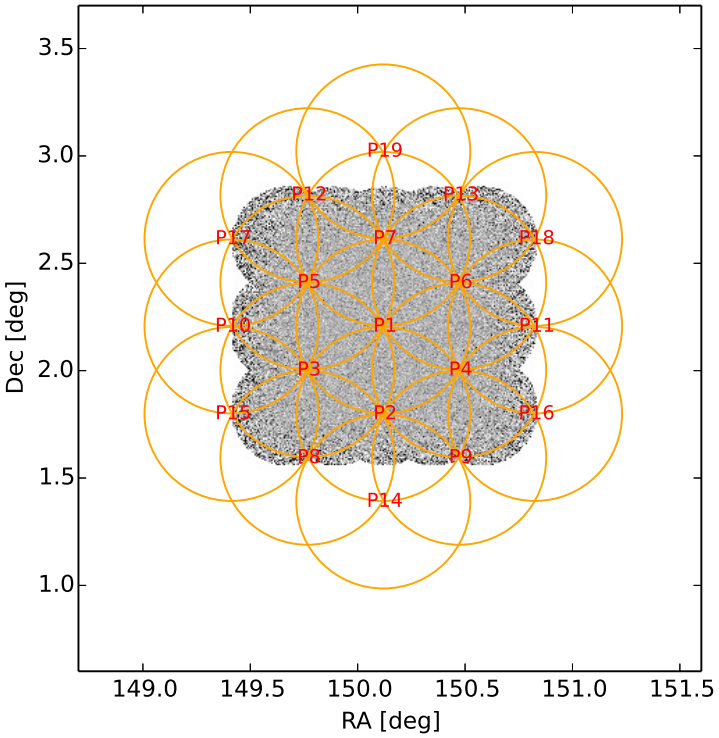

FIGURE 3.1: Pointing lay-out of GMRT observations at 610 MHz. The 1.4 GHz map of the full 2deg^2 COSMOS field is shown in the background.

3.1.2 Observing Strategy

The data was taken in spectral line mode (to limit bandwidth smearing) centred on a frequency of 608 MHz and with two polarizations. The two sidebands; the upper side band (USB) covering the 608-624 MHz range and the lower side band (LSB) spanning 592-608 MHz, were each split into 128 channels of width 125 kHz. The USB was of a much higher quality than the LSB, and so we opted only to use the USB data for our image. The source 3C147 (flux of 38.3Jy at 610 MHz), was used for amplitude and flux calibration and observed for rougly 10 minutes at the start of each observing run (but 30 minutes on 22 February). 3C237, although being 5.62 deg from the centre of the COSMOS field[4], was the closest bright (12.9Jy), unresolved source suitable for phase and bandpass calibration. 3C237 and the pointings were targeted in an alternating pattern of scans lasting 5 and 20 minutes respectively during the course of the observation runs. Over the course of the four days each target was visited six times, for a total integration

[4]Separations of more than 2deg between phase calibrator and target sources are not ideal, as the ionosphere can vary significantly on such scales.

time of 2 hours per target, except in the case of the central pointing (COS01), which accumulated 4.3 hours (13 scans). We used only the COS01 data from March 2 in order to have uniform coverage of the field. The observing schedule is summarised in Table 3.2.

TABLE 3.1

Source	RA(J2000)	Dec(J2000)	Comments
3C147	05:42:36.1298	49:51:07.164	38.9Jy, Amplitude and flux calibrator
3C237	10:08:00.0042	07:30:15.777	12.9Jy, Phase and bandpass calibrator
COS01	10:00:28.6041	02:12:20.977	Centre of COSMOS

TABLE 3.2: Observing strategy: The numbers of scans (lasting 20 minutes) for each pointing per day.

Date	P1	P2	P3	P4	P5	P6	P7	Antennas down	Duration
22.02.2007	4	4	2	3	–	–	5	A11	13:54–23:53
23.02.2007	3	–	4	–	6	6	–	A11	14:13–23:29
24.02.2007	–	2	–	3	–	–	1	A11 and A16	13:51–23:38
02.03.2007	6	–	–	–	–	–	–	A11 and A3	14:14–20:33

3.2 GMRT Data Reduction and Imaging

An AIPS (Greisen, 2003), python and Parseltongue (Kettenis & Sipior, 2012)-based pipeline, developed specifically to automate the calibration, imaging and cataloguing steps for GMRT observations, was used to reduce and image the data. It is built on the AIPSlite pipeline of Bourke et al. (2013) and will be described in detail in Kloeckner et al. (in prep). In the following we briefly outline the major steps.

3.2.1 Data Reduction

Since the phase calibrator (3C237) is a bright source detected on all baselines, the flagging and calibration proceedures were first performed on this source and then those correction tables were applied to the targets. After that, a more careful flagging of the targets was performed to help improve the rms in the final image, before performing a deep clean and mosaicing. The proceedure is as follows:

Before running any automated flagging or performing a delay correction to the data, the amplitudes on each baseline of 3C237 were inspected manually and any baselines or scans with obvious problems were manually flagged using the task 'UVFLG'. Only the most obvious radio frequency interference (RFI; likely solar and ionosphere interference, hardware issues and local manmade interference from overhead aircraft, cellphones etc.) and 'dead' antennas (hardware issues) were cut at this stage[5]. Antenna 11 was offline for all of the 2007 dates, in addition we lost antenna 16 on the 24 February and antenna 3 on the 22 February. On top of that we lost around four whole baselines on any given day. We also cut the first and last 10 channels of the datasets, which tended to be the noisiest.

Next, an automated flagging procedure was applied, in brief, it involved removing fitting a background model to each baseline and cutting those visibilities lying more than 3σ from the background-subtracted mean (more details in Kloeckner et al. in prep.). An antenna-based delay correction (to account for recent changes to the hardware setup) was determined using the AIPS task FRING and the delay corrected data was auto-flagged once more. An amplitude calibration was then performed on 3C237 using the input from SETJY, CALIB was run (on channel 60) to determine phase correction solutions and the task BPASS was used to determine the bandpass calibration. All these calibration corrections were also applied to the targets and the delay correction per antenna, UV distance and amplitude vs. channel plots were then inspected to deduce the efficacy of the calibration and flagging procedures. We generally found a lot of strong RFI on the shortest baselines and thus clipped the phase calibrator at 17Jy using UVFLG (this always resulted in a visibility loss of less than 1%).

A phase and amplitude self-calibration[6] of 3C237 was performed after we determined that it was close enough to the field that the phases would not be corrupted by the ionosphere. Sel calibration time intervals used averages from a maximum of 60 minutes to a minimum of 1 minute for the phase, and a maximum of 15 minutes and minimum of 5 minutes for the amplitude were used. IMAGR was used to produce the clean image during each integration. Due to the large w-term it was necessary to divide the pointing into sub-facets using the task SETFC. The number of clean components in each self calibration pass started at 200 and increased

[5]The delay calibration routine is generally robust with respect to bad data.

[6]This helps to improve the dynamic range. It's analogous to focusing in optical astronomy.

in steps of 200. Local sky model entries were determined by fitting Gaussians using the task JMFIT to the $> 3\sigma$ clean components.

A final baseline-based closure correction[7] and channel-based bandpass correction were determined on 3C237 using AIPS tasks UVFIX, CALIB, BLCAL, and CPASS. The delay spectra for each baseline were inspected and problematic scans were removed in combination with a 5σ outlier clipping of the visibilites.

Before applying the self-calibration and baseline-based closure corrections determined on 3C237 to the targets we deleted all the UV visibilities from the target datasets correspoding to the ones that were flagged in the phase calibrator[8]. After that, self calibration and baseline-based solutions determined on the phase reference source were then applied to the target pointings in a baseline-based calibration run. The target data were carefully inspected, flagged and clipped (an absolute cut off at 2 Jy and then 5σ outliers) to improve the rms in the final image.

In the case of pointings 2-4 and 7, it was necessary to combine observations taken during runs on different days. To do so, the target UV visibility amplitudes needed to be rescaled. The scale factors were determined on the 3C237 visibilites by calculating the ratio of the mean amplitude of all the visibilities for the appropriate day to the mean for all the days that the pointing in question was observed. After that the target datasets were merged.

3.2.2 Imaging

CLEAN was run on the final calibrated combined pointings with a Briggs robust parameter of 3 to produce a naturally-weighted image. This ROBUST setting was the best compromise[9] between the resolution and the rms. We set clean boxes around the sources to minimize sidelobes and used 41,000 iterations of CLEAN. In order to produce a map with as much uniformity in sensitivity and resolution as possible across the full extent, we perform a second imaging run for all seven pointings fixing the clean resolution beam - we choose a circular beam with a FWHM taking the value of the major axis of the clean beam of the pointing with

[7]This helps to correct for offsets in the correlator, pointing errors on very extended sources and mis-matched bandpasses etc.

[8]In Figure 3.4 we plot the UV coverage for the Stokes LL polarization of the central pointing after all flagging has been completed.

[9]ROBUST=5 for pure natural weighting, which optimises point source sensitvity. ROBUST=-5 for pure uniform weighting, which minimises sidelobes.

the lowest resolution. We then split these final pointing images into 42 facets and combined the pointings facet-wise with FLATN, weighting the facets according to their distance from the centre of the pointings (to account for increasing noise at the pointing edges), to produce the 2 $\deg^2$ mosaic of the full field.

3.3 Image Properties and Catalog

The final imaging procedure for the full mosaic ($\approx$ 3$\deg^2$ and covering the full COSMOS field) is in development and will be published near the end of 2016. In this section and the following ones we present the preliminary results from an image of the central pointing only, which covers an area of 1.4 $\deg^2$ of the COSMOS field. The image was produced by Hans-Rainer Kloeckner.

3.3.1 Image Properties

Applying the calibration and imaging procedure decribed in Sections 3.2.1 and 3.2.2 results in an image o the central 1.4 $\deg^2$ of the COSMOS field (Figure 3.2) with an average rms of 45 μJy /beam[10]and angular resolution of $8.8'' \times 6.4''$. This image is based on two hours of integration time from observations taken on 02.03.2007, when two antennas were down (Table 3.2). The UV coverage (for the Stokes LL polarization) is presented in Figure 3.4. Note that there is generally less coverage on longer baselines and hence some flux will be lost on small scales. SETJY set a value of 12.23 Jy for 3C237 meaning that the absolute flux calibration was off by 5 %.

In Figure 3.3 we present a noise map of the central pointing (the proccedure to create it is described in Section 3.3.2.1), which also includes models of the brightest 100 σ sources. The average noise in the centre-most area was quite good (in line with the $\sim$45 μJy/beam expected from the exposure time calculator) although much higher near sources and increases rapidly towards the pointing edges (Figure 3.5). The global dynamic range[11] was 176, reduced to 68 around

[10]The rms distribution peaks at 45 μJy/beam and this is the average rms in the central 0.3 $\deg^2$, the average across most of the map is 100 μJy/beam.

[11]The ratio of the peak image intensity to the brightest spurious feature in the image - this is reduced in the case of poor UV coverage, i.e when the full range of spatial scales of the sources is not adequately covered.

bright $5\,\sigma$ sources. In Figure 3.5, the rms vs. cumulative area is plotted along with the noise distribution for the pixels in Figure 3.3. Typically a Gaussian rms distribution is to be expected, here, the significant long tail is owing to the inclusion of the bright sources in the rms map - they were modelled and extracted from the image in order to aid source detection near those bright objects.

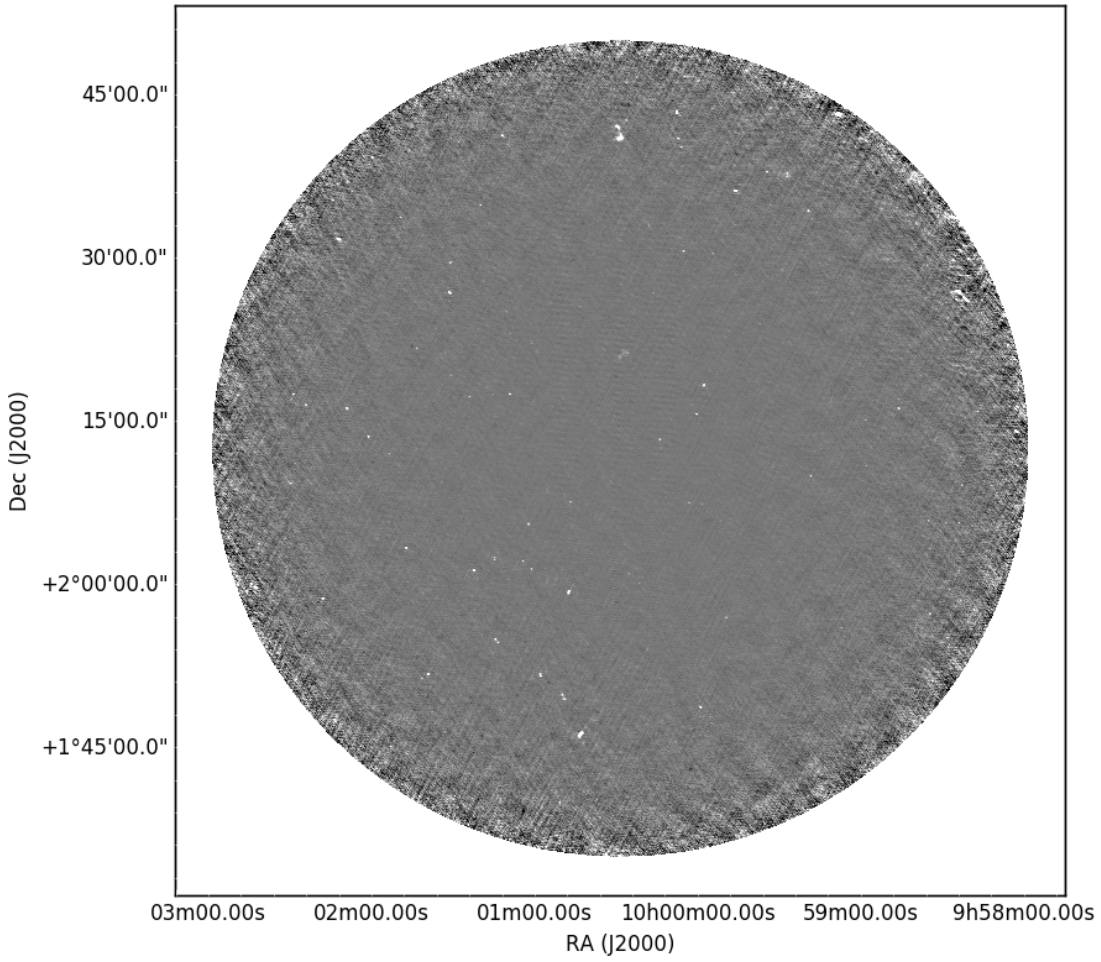

FIGURE 3.2: Map of the central pointing. The colorscale is such that lighter shades represent higher flux densities.

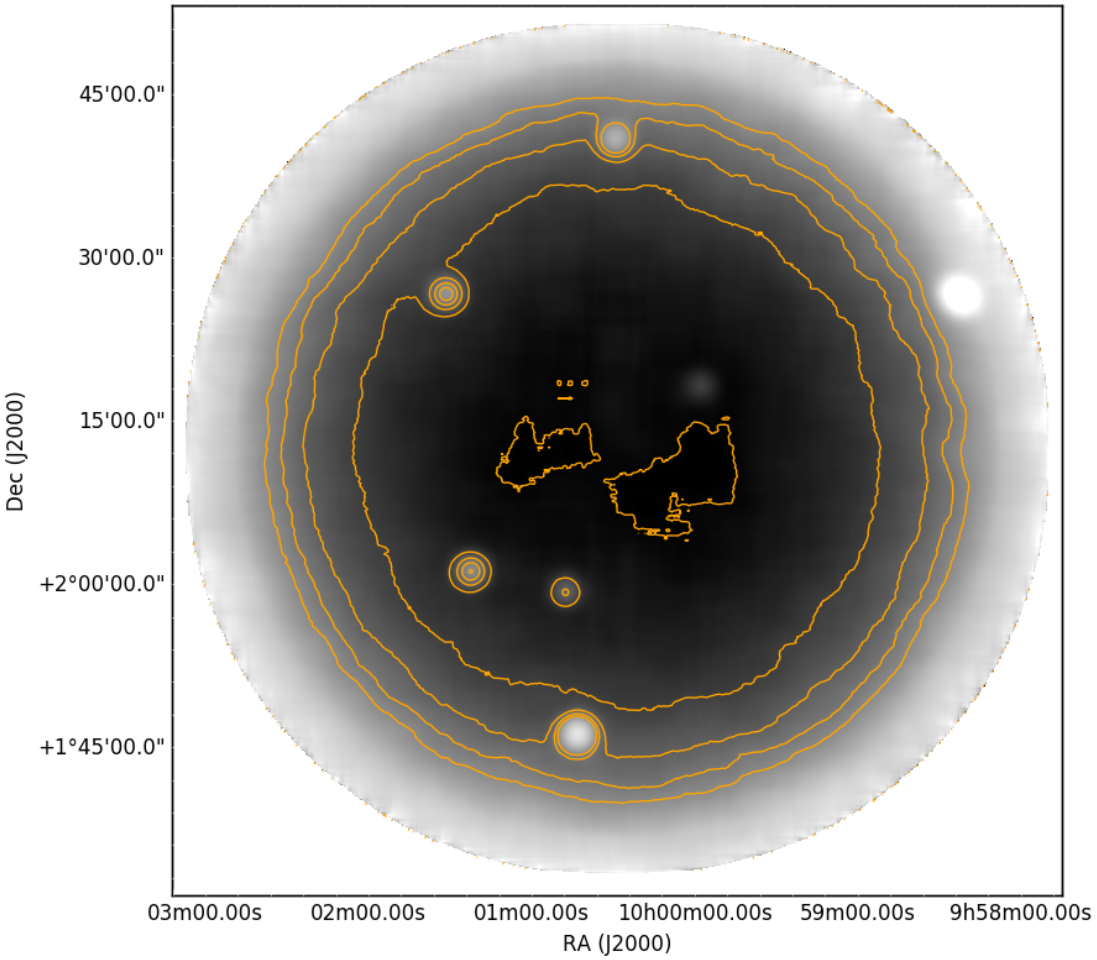

FIGURE 3.3: Noise map of the central pointing. Note that also included here are the $100\sigma_{\text{global}}$ sources - modelled as Gaussians. A log color scale is employed, where lighter shades represent higher flux densities. The orange contours are rms levels of $50\,\mu$Jy/beam, $100\,\mu$Jy/beam, $150\,\mu$Jy/beam, $200\,\mu$Jy/beam and $250\,\mu$Jy/beam.

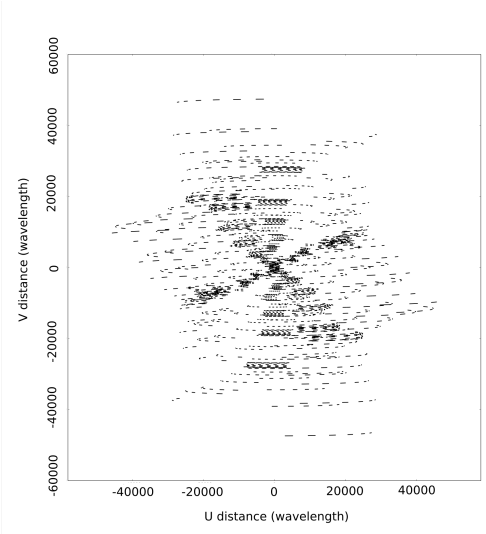

FIGURE 3.4: The UV coverage of the central pointing (P1) for the Stokes LL polarization from the 2 hours of observations on 02.02.2007 after all manual and automated flagging has been applied The coverage for the Stokes RR is similar.

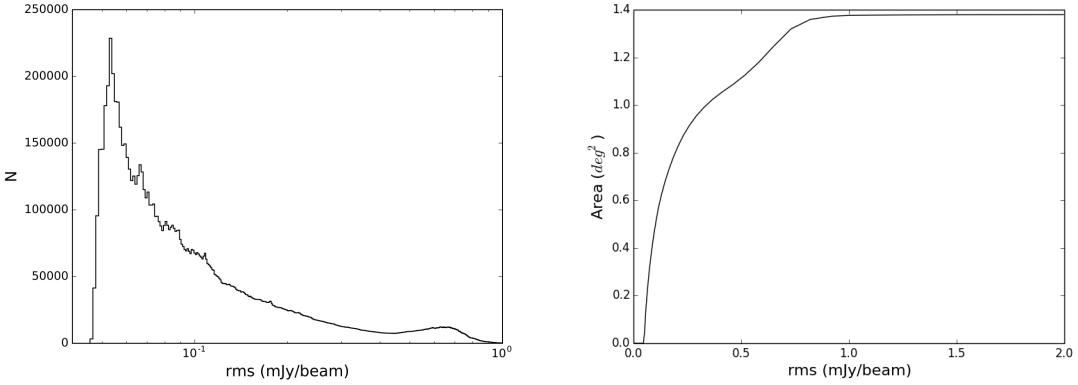

FIGURE 3.5: Distribution of the noise per pixel in Figure 3.3 (left panel) and rms vs. cumulative area (right panel). Note that the long tail towards high values in the pixel noise distribution is owing to bright 100 σ sources.

3.3.2 The COSMOS GMRT 610 MHz Catalog

Sources were detected and properties extracted from the final image using the cataloguing routine of Mauch et al. (2013).

3.3.2.1 Source Extraction

The cataloging routine first determines a global rms noise ($\sigma_{\rm global}$) from the central region of the image (amounting to 50% of the total image area). This is done with IMEAN by fitting the noise part of the pixel flux distribution. This step is iterated until the rms changes by less than 1% between the iterations.

$100\sigma_{\rm global}$ are identified using SAD. Artifacts and noise peaks close to these bright sources are identified by determining the radius at which the density of $3\sigma_{\rm global}$ sources around the bright source becomes equal to that the global density value (r_{source}). Then, to prevent true sources from being rejected, a local dynamic range around bright sources is computed. It is taken to be the median of all the individual dynamic ranges for the bright sources (which are defined as the ratio of the flux densities of the $100\sigma_{\rm global}$ to that of the brightest $3\sigma_{\rm global}$ source in its zone of influence). RMSD is used to produce a local rms ($\sigma_{\rm local}$) map by calculating the rms in boxes of $5\times$ the major axis of the restoring beam. This is iterated 30 times with the $> 3\sigma$ wings being clipped from the rms distribution at each step. In addition, a local mean map is constructed via a similar proceedure. Gaussians of width r_{source} and peaks determined by the median local dynamic range are added to the rms map at the positions of the $100\sigma_{\rm global}$ peaks (Figure 3.3).

The mean map is subtracted from the input image and the result is then divided by the rms model. Source detection with SAD is performed on the resulting image to find the positions and sizes of the $5\sigma_{\rm local}$ peaks. The peak and total flux densities of these sources are then determined on the original input image by fitting elliptical Gaussians using JMFIT at the source positions and leaving the peak flux as a free parameter. The 'true' uncertainties of the source properties are determined with the (Condon, 1997) equations and adding an additional 5% 'calibration uncertainty' in quadrature. Total flux densities are computed from the peak fluxes, $\mathrm{S_{total}} = \mathrm{S_{peak}} \times \mathrm{Area_{source}}/\mathrm{Area_{beam}}$. For any source whose size is within $2.33\,\sigma$ of the beam size, the cataloger sets $\mathrm{S_{total}} = \mathrm{S_{peak}}$, that is the source is considered to be an unresolved point source.

3.3.2.2 The Final Catalog

The cataloging routine returns a component catalog. However, the field contains several sources that are significantly extended and the cataloger does not attempt to detect such sources, but splits them into multiple components. Multiple component sources were identified and their total fluxes computed by Marco Bondi, who also did similar work for the 3 GHz and 324 MHz COSMOS catalogs. The methodology is as follows: Possible multi-component sources were selected from the list of multi-component sources in the 1.4 GHz catalog of Schinnerer et al. (2010). Components in the 610 MHz image that were separated by less than $1''$

were identified and visually inspected in order to select very extended sources that are not detected at 1.4 GHz. The total flux of the sources identified as being multi-component was determined by integrating the flux down to $2\,\sigma_{av}$ (where σ_{av} is the average of the σ around single components).

In addition to the catalog, the routine performs some consistency checks of the fluxes and astrometry by comparing them to those in other surveys. The fluxes were compared to those of the National Radio Astronomy Observatory Very Large Array (VLA) Sky Survey (NVSS Condon, 1992) and the astrometry to that of the Faint Images of the Radio Sky at Twenty-cm (FIRST Becker et al., 1995) survey. The GMRT-FIRST[12] RA and Dec median offsets (for the 136 sources that are also detected in FIRST) were 2.5″ and 3″, respectively. Positional offsets can be introduced by errors in the amplitude self calibration and antenna pointing issues. The radio spectrum at cm wavelengths takes a simple power law form, with the spectral flux density $S_\nu = \nu^\alpha$. A value of $\alpha = -0.7$ was assumed for the spectral index to extrapolate 610 MHz values from the NVSS 1.4 GHz fluxes to compare to ours to check for flux offsets. 87 members of our component catalog are also detected in NVSS. We found that for the cross-matched sources NVSS fluxes are on average a factor of ≈1.8 greater than the GMRT ones. The NVSS resolution is 45″ and it is very likely that we have missed extended flux components[13]. Since we are not doing a direct flux comparison, but rather having to assume a spectral index value[14], this will introduce apparent offsets too.

[12]The FIRST beam is $6.4'' \times 5.4''$

[13]In general underestimation of fluxes can be down to several effects working in tandem, these include: Missing flux, i.e poor UV coverage, whereby shorter baselines have been flagged thus reducing the flux densities of the sources on large scales. An incorrect absolute flux calibration, whereby SETJY uses an incorrect value of the amplitude and phase calibrator flux densities. Cleaning too deep, particularly when sidelobes are present - these get subtracted and the source flux density is thus underestimated. And an incorrect primary beam correction -particularly for the sources furthest from the phase centre.

[14]Note that we could be detecting many steep spectrum ($\alpha < -1$) radio sources, particularly at z∼1 and higher.

3.3.3 Catalog

The catalog returned by the Mauch et al. (2013) routine detected 249 components down to 5σ. M. Bondi identified 18 multiple-component sources, for a total of 202 single component sources and 18 multiple component sources which are presented in Tables 3.4 and 3.3 in order of right ascension.

In the case of the entries in Table 3.3 16 of them were detected in the 3 GHz of Smolčić et al. (in press) which has excellent resolution (0.75″) and astrometry, hence the coordinates reported are from that catalog, for the remaining two sources the Schinnerer et al. (2010) 1.4 GHz coordinates are reported. At the end of this chapter we show cutouts of the 18 sources.

The entries of Table 3.4 are described in Sections 3.3.2.1 and 3.3.2.2. 18 % of the 202 single component sources are unresolved. We just show a portion of the total number of sources to give the reader an idea of the content - a catalog of the full mosaic will be publically available early next year.

The Table 3.3 columns are as follows:
Column(1): 3 GHz source name
Column(2): Right ascension (J2000)
Column(3): Declination (J2000)
Column(4): Integrated flux density

TABLE 3.3: Multiple-component sources. Courtesy of M. Bondi.

Name	R.A. (deg)	Dec. (deg)	S_{total} (mJy)
COSMOSVLA3 J095823.31+022628.4	149.597130105	2.441242546	220.1
COSMOSVLA3 J095908.31+024309.6	149.784663358	2.719339119	110.2
COSMOSVLA3 J095927.25+023729.3	149.863546055	2.624820767	10.5
COSMOSVLA3 J095959.61+024608.9	149.99838851	2.76914121	3.88
COSMOSVLA3 J100007.91+024315.3	150.032959	2.720943	17.0
COSMOSVLA3 J100027.43+022123.3	150.114328929	2.356472694	10.3
COSMOSVLA3 J100028.28+024103.3	150.117853976	2.6842711	102.9
COSMOSVLA3 J100043.19+014607.8	150.179959242	1.768857009	83.6
COSMOSVLA J100047.60+015910.3	150.198349	1.9862083	19.6
COSMOSVLA3 J100049.59+014923.7	150.206627	1.823253	9.7
COSMOSVLA J100058.05+015129.0	150.2418823	1.8580667	13.5
COSMOSVLA3 J100101.98+020511.4	150.258263	2.086516	3.52
COSMOSVLA3 J100114.13+015444.1	150.308884	1.912264	8.8
COSMOSVLA3 J100114.85+020208.6	150.311909	2.035737	3.72
COSMOSVLA3 J100140.13+015129.6	150.417214	1.858246	10.7
COSMOSVLA3 J100212.06+023135.0	150.550262	2.526394	29.8
COSMOSVLA3 J100230.19+020913.2	150.625809	2.153692	7.12
COSMOSVLA3 J100243.20+015943.4	150.680038	1.995399	98.5

The Table 3.4 columns are as follows:
Column(1): Right ascension (J2000)
Column(2): Declination (J2000)
Column(3): Uncertainty in right ascension
Column(4): Uncertainty in declination
Column(5): Peak flux density (fitted)
Column(6): Statistical error of peak flux density
Column(7): Integrated flux density
Column(8): Statistical error of integrated flux density
Column(9): Convolved source size major axis
Column(10): Convolved source size minor axis
Column(11): Convolved source position angle (East of North)
Column(12): Statistical error of major axis
Column(13): Statistical error of minor axis
Column(14): Statistical error of position angle
Column(15): Local rms at source position
Column(12): Flag for resolved (1) and unresolved (0) sources

TABLE 3.4: Single component sources.

R.A. (deg)	Dec. (deg)	ΔR.A. (″)	ΔDec (″)	S_{peak} (mJy/beam)	ΔS_{peak} (mJy/beam)	S_{total} (mJy/beam)	ΔS_{total} (mJy/beam)	θ_{maj} (″)	θ_{min} (″)	P.A. (deg)	$\Delta\theta_{maj}$ (″)	$\Delta\theta_{min}$ (″)	ΔP.A. (deg)	rms mJy/beam	Res
149.5092	2.29539	6.11425E-4	4.4479E-4	3.98964	0.119691	3.98964	0.135829	8.78292	6.37596	61.5	0.175665	0.17566	0.0	0.621412	0
149.50962	2.08266	9.85918E-4	8.32663E-4	3.20554	0.0961684	5.88291	0.132908	10.91	9.42	66.5	0.218213	0.218208	0.0	0.617542	1
149.51308	2.23242	6.64964E-5	4.96502E-5	35.7515	1.07254	38.3064	1.2524	9.05	6.63	60.7	0.181	0.181	0.0	0.58491	1
149.52391	2.03181	0.00120536	7.1027E-4	2.21577	0.0664759	2.21577	0.0754421	8.78292	6.37596	74.5	0.175683	0.175665	0.0	0.638604	0
149.54662	2.02107	0.00104549	6.63567E-4	2.52187	0.0756581	2.91154	0.101816	10.14	6.37596	63.3	0.202818	0.202803	0.0	0.545343	1
149.57215	2.26261	8.9025E-4	3.64375E-4	1.86264	0.0558798	2.31798	0.0824773	10.93	6.37596	78.9	0.21861	0.218601	0.0	0.28758	1
149.58566	2.49569	5.89999E-4	8.51751E-4	4.57796	0.13734	8.74395	0.245096	13.32	8.03	29.8	0.266409	0.266402	0.0	0.621339	1
149.5964	2.14968	3.66242E-4	2.51771E-4	2.36327	0.0708985	2.53853	0.0800834	8.82	6.82	70.1	0.176402	0.176401	0.0	0.211128	1
149.5987	2.5471	5.02888E-4	3.94224E-4	6.98718	0.209617	10.1612	0.260574	9.8	8.31	72.6	0.196004	0.196002	0.0	0.756949	1
149.60018	2.09171	3.29347E-4	2.14262E-4	2.80286	0.0840862	2.80286	0.0954221	8.78292	6.37596	67.9	0.17566	0.175659	0.0	0.226863	0
149.60626	2.55959	4.82821E-4	4.27694E-4	5.77546	0.173265	6.05629	0.207812	9.21	6.37596	50.6	0.184205	0.184201	0.0	0.726506	1
149.60812	2.55859	9.22563E-4	5.83865E-4	6.00153	0.180047	11.4915	0.434517	16.1	6.66	59.1	0.32201	0.322	0.0	0.71681	1
149.61544	1.99072	8.03536E-4	7.11606E-4	1.39976	0.0419938	1.69921	0.0469996	8.84	7.69	121.1	0.176811	0.176807	0.0	0.287119	1
149.61887	1.91621	3.7709E-4	2.83522E-4	4.1177	0.123532	4.33343	0.139164	8.78292	6.71	62.4	0.175661	0.175659	0.0	0.394342	1
149.62081	2.09188	5.14972E-4	4.40846E-4	1.47443	0.0442334	1.54445	0.0529855	9.2	6.37596	52.2	0.184006	0.184001	0.0	0.195172	1
149.62162	2.55962	9.97489E-4	0.00100009	3.80169	0.114052	8.86665	0.241198	15.42	8.47	44.9	0.308416	0.308402	0.0	0.622562	1
149.64508	2.05324	4.91219E-4	3.32779E-4	1.44894	0.0434687	1.44894	0.0493291	8.78292	6.37596	65.5	0.175663	0.17566	0.0	0.177099	0
149.64547	1.95274	3.22214E-4	2.23E-4	3.25395	0.097619	3.41422	0.110016	8.78292	6.69	67.9	0.17566	0.175659	0.0	0.259072	1
149.6474	2.09532	3.12396E-4	1.97651E-4	2.31185	0.0693557	2.61548	0.0852358	9.47	6.69	68.4	0.189402	0.1894	0.0	0.15994	1
149.65397	2.59646	9.02754E-4	5.99328E-4	3.60831	0.108251	5.19184	0.172399	11.78	6.84	60.4	0.235612	0.235602	0.0	0.57801	1
149.66702	2.62319	0.00108661	8.36731E-4	3.74871	0.112463	10.8423	0.240632	16.1	10.06	57.3	0.322013	0.322003	0.0	0.579003	1

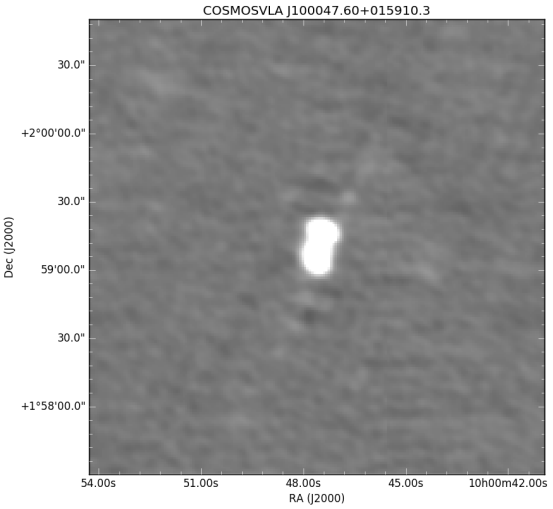
COSMOSVLA J100047.60+015910.3
30.0"
+2°00'00.0"
30.0"
59'00.0"
30.0"
+1°58'00.0"
Dec (J2000)
54.00s
51.00s
48.00s
45.00s
10h00m42.00s
RA (J2000)

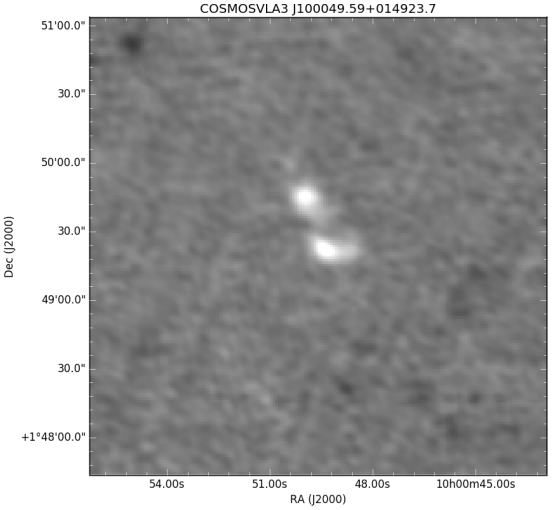
COSMOSVLA3 J100049.59+014923.7
51'00.0"
30.0"
50'00.0"
30.0"
49'00.0"
30.0"
+1°48'00.0"
Dec (J2000)
54.00s
51.00s
48.00s
10h00m45.00s
RA (J2000)

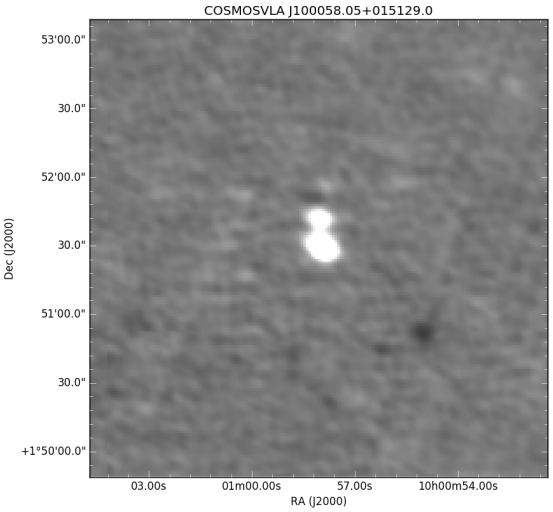
COSMOSVLA J100058.05+015129.0
53'00.0"
30.0"
52'00.0"
30.0"
51'00.0"
30.0"
+1°50'00.0"
Dec (J2000)
03.00s
01m00.00s
57.00s
10h00m54.00s
RA (J2000)

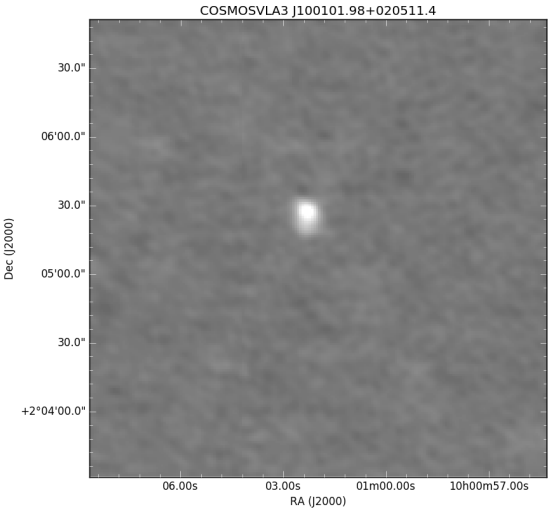
COSMOSVLA3 J100101.98+020511.4
30.0"
06'00.0"
30.0"
05'00.0"
30.0"
+2°04'00.0"
Dec (J2000)
06.00s
03.00s
01m00.00s
10h00m57.00s
RA (J2000)

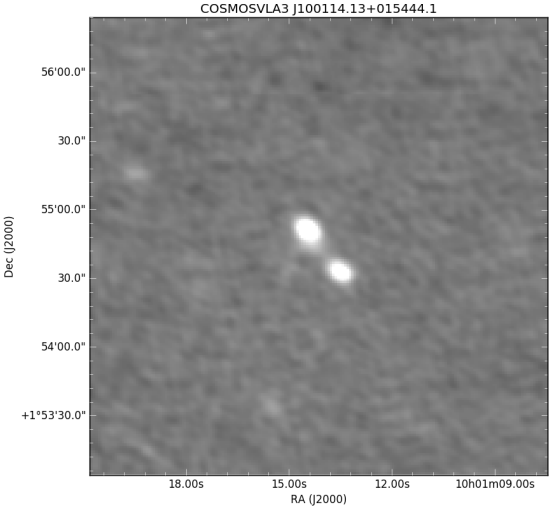
COSMOSVLA3 J100114.13+015444.1
56'00.0"
30.0"
55'00.0"
30.0"
54'00.0"
+1°53'30.0"
Dec (J2000)
18.00s
15.00s
12.00s
10h01m09.00s
RA (J2000)

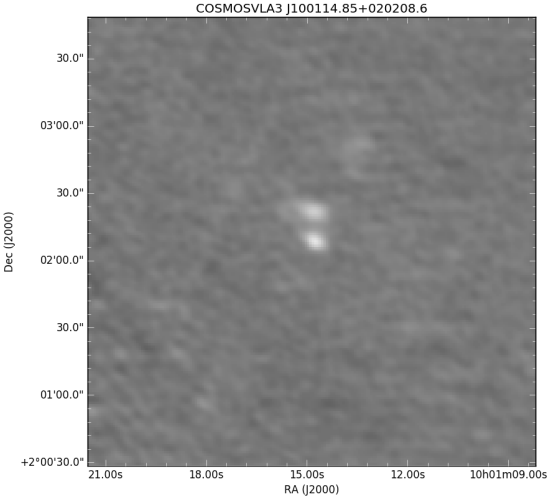
COSMOSVLA3 J100114.85+020208.6
30.0"
03'00.0"
30.0"
02'00.0"
30.0"
01'00.0"
+2°00'30.0"
Dec (J2000)
21.00s
18.00s
15.00s
12.00s
10h01m09.00s
RA (J2000)

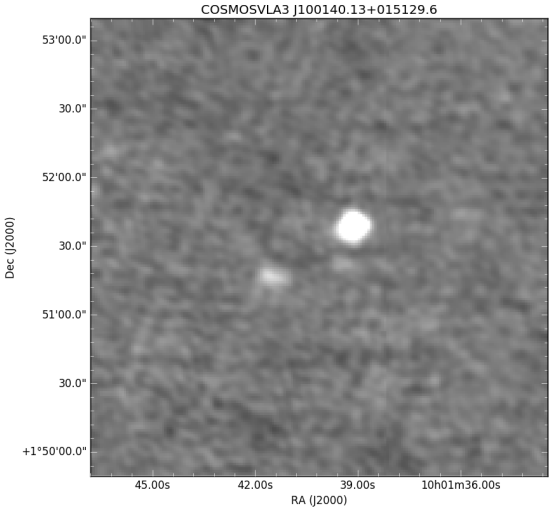
COSMOSVLA3 J100140.13+015129.6
53'00.0"
30.0"
52'00.0"
30.0"
51'00.0"
30.0"
+1°50'00.0"
Dec (J2000)
45.00s
42.00s
39.00s
10h01m36.00s
RA (J2000)

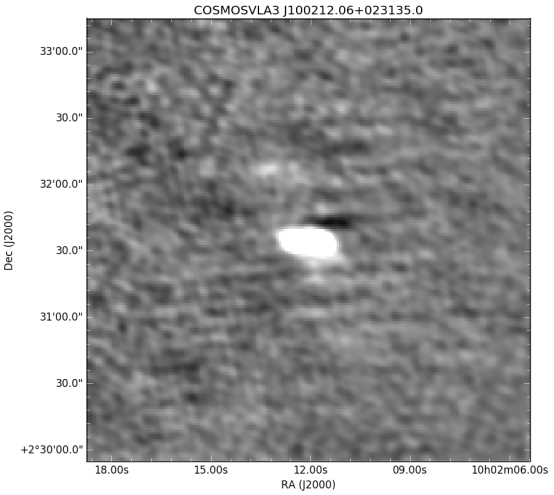
COSMOSVLA3 J100212.06+023135.0
33'00.0"
30.0"
32'00.0"
30.0"
31'00.0"
30.0"
+2°30'00.0"
Dec (J2000)
18.00s
15.00s
12.00s
09.00s
10h02m06.00s
RA (J2000)

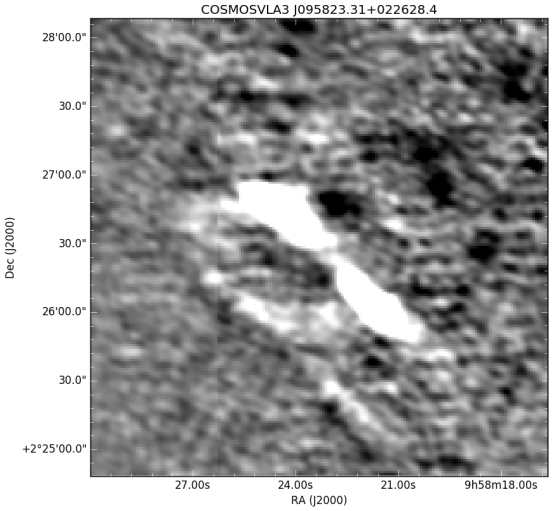
COSMOSVLA3 J095823.31+022628.4
28'00.0"
30.0"
27'00.0"
30.0"
26'00.0"
30.0"
+2°25'00.0"
Dec (J2000)
27.00s
24.00s
21.00s
9h58m18.00s
RA (J2000)

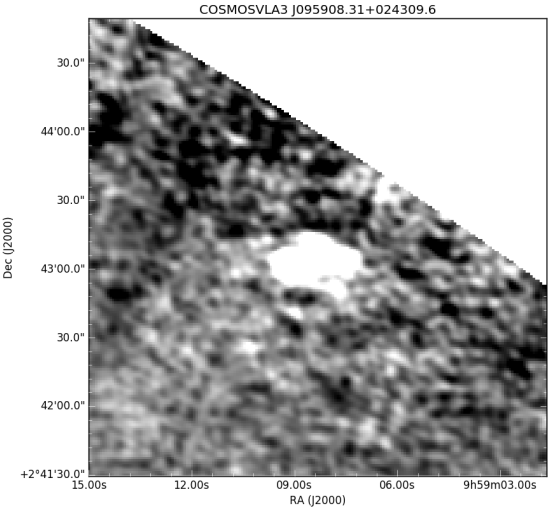
COSMOSVLA3 J095908.31+024309.6
30.0"
44'00.0"
30.0"
43'00.0"
30.0"
42'00.0"
+2°41'30.0"
Dec (J2000)
15.00s
12.00s
09.00s
06.00s
9h59m03.00s
RA (J2000)

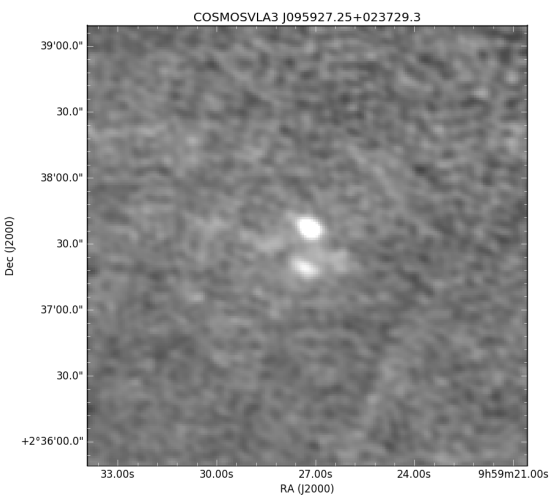
COSMOSVLA3 J095927.25+023729.3
39'00.0"
30.0"
38'00.0"
30.0"
37'00.0"
30.0"
+2°36'00.0"
Dec (J2000)
33.00s
30.00s
27.00s
24.00s
9h59m21.00s
RA (J2000)

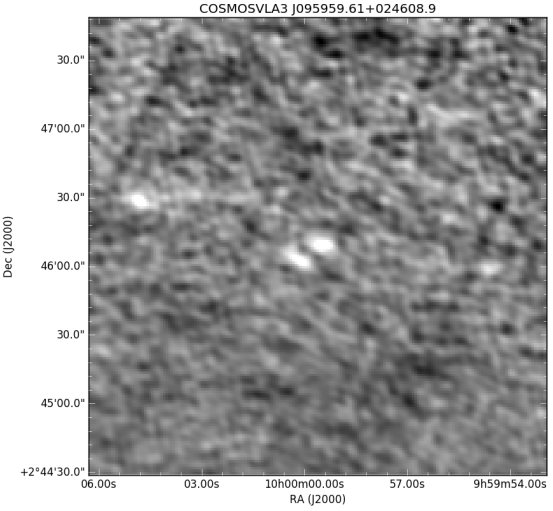
COSMOSVLA3 J095959.61+024608.9
30.0"
47'00.0"
30.0"
46'00.0"
30.0"
45'00.0"
+2°44'30.0"
Dec (J2000)
06.00s
03.00s
10h00m00.00s
57.00s
9h59m54.00s
RA (J2000)

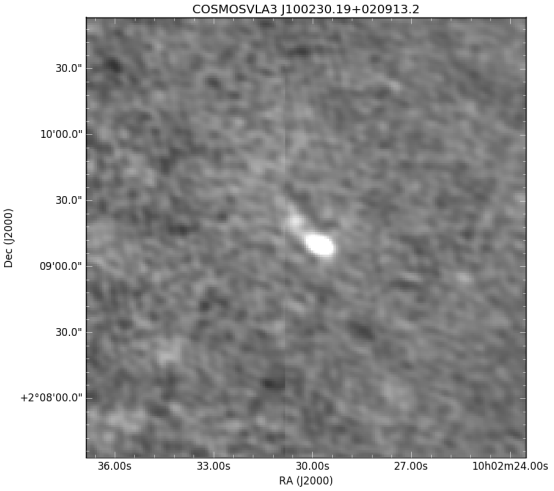
COSMOSVLA3 J100230.19+020913.2
30.0"
10'00.0"
30.0"
09'00.0"
30.0"
+2°08'00.0"
Dec (J2000)
36.00s
33.00s
30.00s
27.00s
10h02m24.00s
RA (J2000)

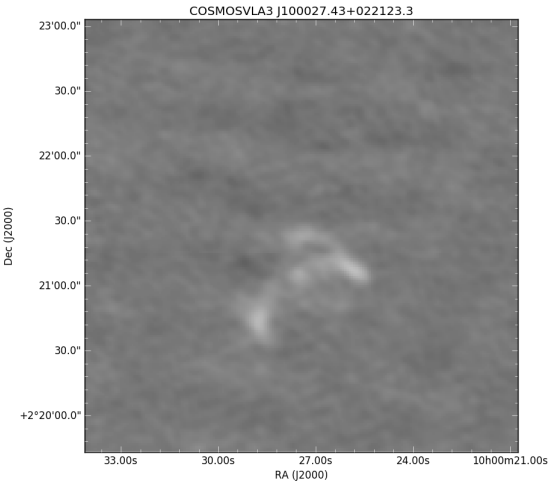
COSMOSVLA3 J100027.43+022123.3
23'00.0"
30.0"
22'00.0"
30.0"
21'00.0"
30.0"
+2°20'00.0"
Dec (J2000)
33.00s
30.00s
27.00s
24.00s
10h00m21.00s
RA (J2000)

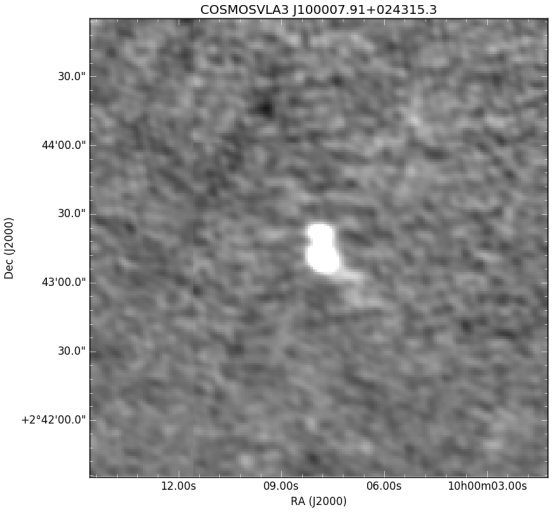
COSMOSVLA3 J100007.91+024315.3
30.0"
44'00.0"
30.0"
43'00.0"
30.0"
+2°42'00.0"
Dec (J2000)
12.00s
09.00s
06.00s
10h00m03.00s
RA (J2000)

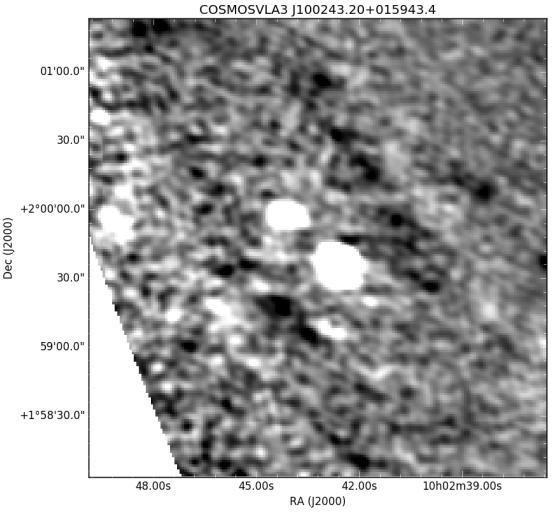
COSMOSVLA3 J100243.20+015943.4
01'00.0"
30.0"
+2°00'00.0"
30.0"
59'00.0"
+1°58'30.0"
Dec (J2000)
48.00s
45.00s
42.00s
10h02m39.00s
RA (J2000)

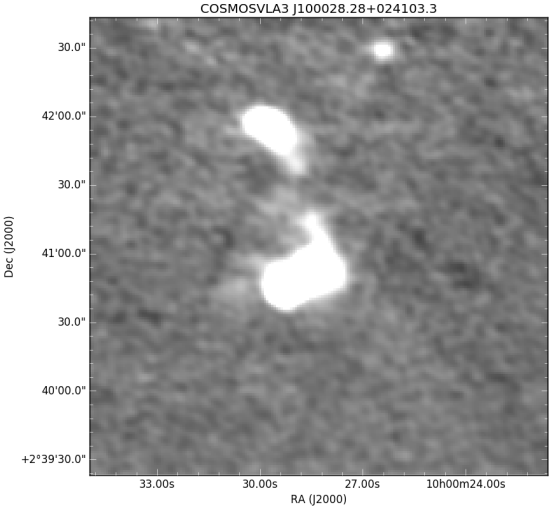
COSMOSVLA3 J100028.28+024103.3
30.0"
42'00.0"
30.0"
41'00.0"
30.0"
40'00.0"
+2°39'30.0"
Dec (J2000)
33.00s
30.00s
27.00s
10h00m24.00s
RA (J2000)

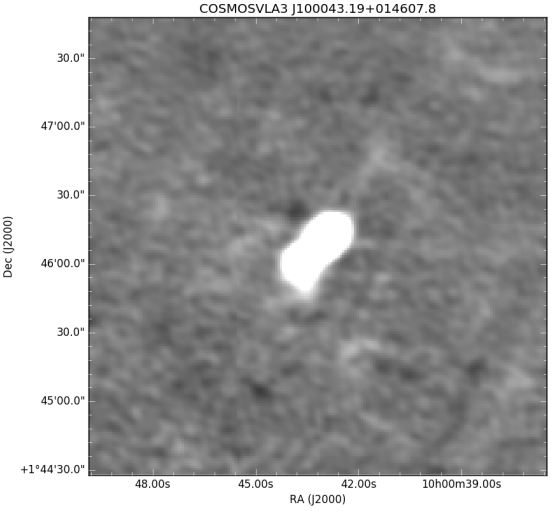
COSMOSVLA3 J100043.19+014607.8
30.0"
47'00.0"
30.0"
46'00.0"
30.0"
45'00.0"
+1°44'30.0"
Dec (J2000)
48.00s
45.00s
42.00s
10h00m39.00s
RA (J2000)

Chapter 4

Properties of 610MHz Sources in COSMOS

In the previous chapter the data reduction and imaging proceedure was presented for the full field, along with a preliminary image and catalog of the central pointing. In this chapter we present the properties of the 220 sources down to 5σ detected in this image (1.4 $\deg^2$ central area of COSMOS) which has an rms of 45μJy/beam and a resolution of $8.8'' \times 6.4''$.

4.1 Introduction

The radio regime provides unique insight into dust-unbiased star formation and AGN physics. Although UV and optical surveys are generally deeper, these wavelengths are often severely dust-extincted. Radio synchrotron emission is an important tool to fully understand the mechanisms driving AGN activity and AGN feedback. In particular there are significant populations of radio selected AGN ('faint radio loud' AGN or 'low-excitation' AGN) that are not identified as AGNs at any other wavelengths, and which seem to increase in number relative to star-forming galaxies at faint radio fluxes (e.g Smolčić et al., 2008; Wilman et al., 2008).

To study the nature of radio sources and take full advantage of the available catalogs we need to study the radio spectral energy distribution over as large a frequency range as possible. This offers insight into the synchrotron and non-thermal

contributions to the radio outputs as a function of redshift and radio luminosity. Lately Delhaize et. al (subm.) has postulated that the M82 model of the non-thermal and free-free relative contributions typically used may be incorrect. This may be responsible for their observed redshift evolution in the infrared-radio correlation (which has also been seen by Magnelli et al., 2015). In addition, having spectral indices of galaxies allows one to select radio galaxies[1] at high redshifts. They are the likely precursors of the most massive ellipticals in the local universe. Spectral index values should steepen with redshift as the effect of inverse Compton scattering of radio photons off the cosmic microwave background becomes more important (Krolik & Chen, 1991; De Breuck et al., 2000). Thus ultra-steep (α <-1.3) spectral indices could be a good proxy for selecting radio galaxies at intermediate redshifts (z ∼1) of which optical detection is unlikely.

Currently, most radio surveys have been conducted at 1.4 GHz. However lower frequencies suffer less from synchrotron losses (since it's $\propto \nu^{-}2$). Several 610 MHz surveys with the GMRT reaching similar depths to ours and on ∼deg^2 fields have been conducted (Bondi et al., 2007; Tasse et al., 2007; Garn et al., 2008; Ibar et al., 2009; Ainsworth et al., 2016). However none of these surveys had the large anicilliary datasets available that COSMOS provides (see Section 1.3), nor the radio band coverage. COSMOS has been observed with the Very Large Array (VLA) at 324 MHz (Smolčić et al., 2014), 1.4GHz (Schinnerer et al., 2004, 2007, 2010) and 3 GHz (Smolčić et al. in press). 610 MHz will be one of the key bands of the Square Kilometer Array (SKA Norris et al., 2015), and in the meantime this catalog helps bridge the gap between the higher frequency COSMOS surveys and the lower frequency (10-240 MHz) bands of the Low Frequency Array (LOFAR).

4.2 Source Fluxes and Number Counts

In the 610 MHz map of the central 1.4 deg^2 area of the COSMOS field described in Chapter 3 we have identified 220 sources. 18 of these are very extended, i.e have multiple components and 18 % of the sources are unresolved. In Figure 4.1 we present the distribution of the integrated fluxes of the sources.

[1]AGN and starbursts, both of which are preferentially hosted in massive red ellipticals (Smolčić et al., 2008).

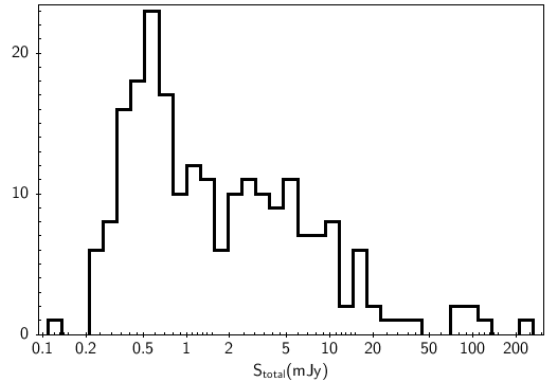

FIGURE 4.1: S_{total} in mJy for the 220 sources. 45% of them have S_{total} <1mJy.

In Figure 4.2 we present the uncorrected normalized differential source counts as a function of total flux density. The source number counts have been corrected to account for the effects of noise variation across the image on source detection. We compare to the corrected number counts from the Bondi et al. (2007) GMRT observations and to the compilation of multiple suveys from de Zotti et al. (2010). It is clear that our survey is incomplete at sub-milliJansky flux levels. It is likely, particularly given that a large fraction of our sources were reported as extended by the Mauch et al. (2013) cataloger, that resolution bias is an issue here. The AIPS task SAD searches for $5\sigma_{local}$ density peaks and thus will miss extended sources whose S_{peak} is below that threshold, but whose S_{total} would be above it, i.e 'smeared' sources. This is furthermore clear in a comparison with VLA surveys at other wavelengths, as we will see in the next subsection.

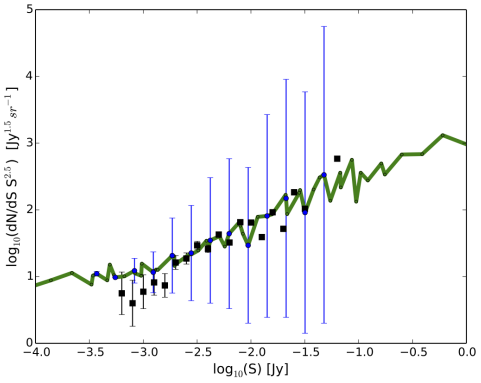

FIGURE 4.2: The differential 610 MHz source counts for our GMRT-COSMOS sources (black). Also shown are the source counts at 610 MHz from the Bondi et al. (2007) GMRT survey of the VVDS-VLA field (blue) and a compilation from de Zotti et al. (2010) in green.

4.2.1 Comparison with Other COMOS Surveys: Spectral Indices

We cross matched our catalog with the VLA-COSMOS surveys at 324 MHz (Smolčić et al., 2014), 1.4 GHz (Schinnerer et al., 2010) and 3 GHz (Smolčić et al. in press)

which have 5σ detection thresholds of 2.5 mJy/beam, 50 μJy/beam and 11.5 μJy/beam respectively. The 1.4 GHz and the 3 GHz are relatively deeper than our catalog, but the 324 MHz is shallower. 125 of the 324 MHz sources have counterparts in the 1.4 GHz survey, and we seem to detect only 72 of these[2]. In addition only 60 % of our sources have 3GHz counterparts[3]. In Figure 4.3 we plot the distribution of the spectral indices for the 72 galaxies which have 324 MHz and 1.4 GHz counterparts. It is clear that, not only are we missing sources, but the ones we do detect have under-reported fluxes and (unsurprisingly) the cross match is biased towards steeper spectrum sources than usual[4]. On average our fluxes seem to be underestimated by close to a factor of two, which would lead the estimates of the α_{3GHz}^{610MHz} to be shallower (+0.3) than expected (Figure 4.3)[5] based on the results of Smolčić et al. (2014) and Smolčić et al. in press.

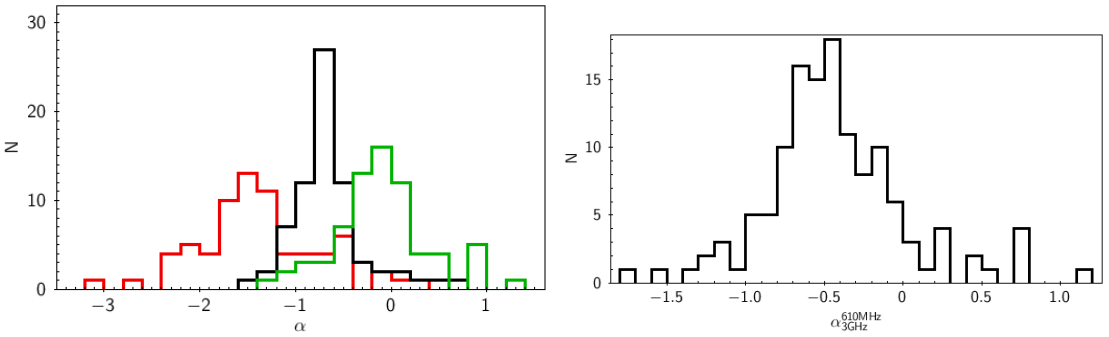

FIGURE 4.3: The spectral indices for the 71 sources with 1.4 GHz and 324 MHz counteparts (left). α_{324MHz}^{610MHz} in red, $\alpha_{1.4GHz}^{610MHz}$ in green and $\alpha_{324MHz}^{1.4GHz}$ in black. Note that the cross-matched sample is biased towards steep spectrum sources and that the 610 MHz fluxes are under-reported in our catalog. This is also clear in the right panel, where α_{3GHz}^{610MHz} peaks at a value of -0.5.

4.3 Source Properties

60 % of our sources have 3 GHz (Smolčić et al. in press) counterparts. This survey is deep (2.3 μJy/beam), high resolution (0.75″) and has astrometry accurate to

[2]Unsurprisingly, the sources which drop out have lower signal to noise and peak fluxes than the ones that have counterparts.

[3]The dropouts could be steep spectrum sources, but given the depth of the 3 GHz survey they would have to be very faint at 610 MHz and have $\alpha \sim$-2, which seems unlikely. We cannot discount the fact that we have spurious sources or astrometry issues.

[4]In general, star forming radio galaxy samples have α values that cluster around -0.7.

[5]Note that there is very little overlap between the samples plotted in the left and right panels, given that the fainter steep spectrum sources with 324 MHz and 1.4 GHz detections will fall below the 3 GHz detection threshold.

within 0.1″. For this reason we choose to work with the 3 GHz cross-matched sample to analyze the redshift distributions, optical properties and star-forming galaxy make-up of our sample.

The 3 GHz survey has been cross matched with the Laigle et al. (2016) photometry catalog and the reliability of the z_{phot} assessed (replaced with z_{spec} where available), in addition to classifying the 3 GHz sources as star-forming or AGN based on their optical properties, X-ray, IR and radio emission etc. (Baran et. al. in prep.). In the left panel of Figure 4.4 we show the redshift distribution of the 129 sources with 3 GHz counterparts. The redshift distribution peaks at $z \sim 1$ and extends to $z \sim 4$. More than half our sample is at $z > 1$.

The catalog we produced is sensitive to sources of 0.225 mJy down to 5σ (Figure 4.1). Based on the works of Smolčić et al. (2008); Wilman et al. (2008); Padovani et al. (2015) at 1.4 GHz, the radio population is expected to be a roughly 50/50 mix of star forming galaxies (SF) and AGN in the submJy regime, with radio loud AGN comprimising most of the >1 mJy sources. We thus expect that we are mostly probing the radio AGN population here, with a roughly 30% incidence of SF galaxies. This does in fact turn out to be the case. In Figure 4.4 we plot the SF/AGN breakdown for the 3 GHz cross-matched sample - only 26 % of this sample are classed as star-forming. At 3 GHz sub-mJy flux levels, the SF/AGN breakdown is roughly 50/50. In addition, in Figure 4.5 we plot the 610 MHz luminosity as a function of redshift (assuming a spectral index of α=-0.7). Even with our underestimated fluxes, it is clear that our sample is AGN dominated and includes a significant fraction of powerful radio AGN.

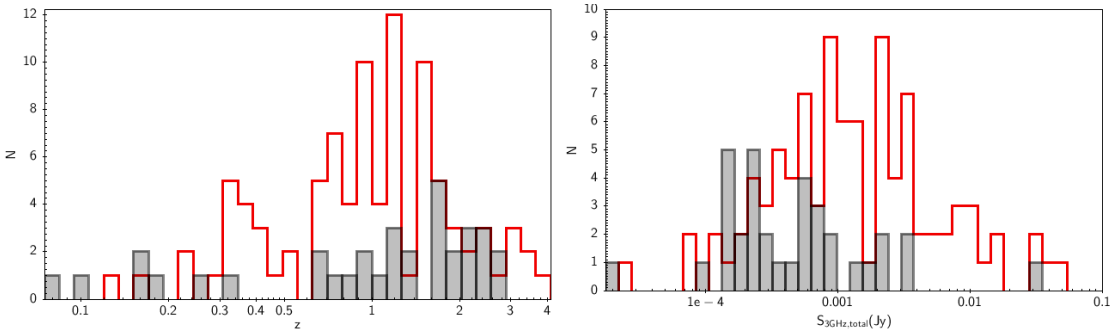

FIGURE 4.4: The star-forming (black)-AGN (red) breakdown by redshift (left) and 3 GHz flux (right).

In Figure 4.6 we show the intrinsic optical color distributions for our galaxies from a cross match with the Laigle et al. (2016) photometry catalog. It is clear that our sample has redder optical colors. This is again in keeping with previous works,

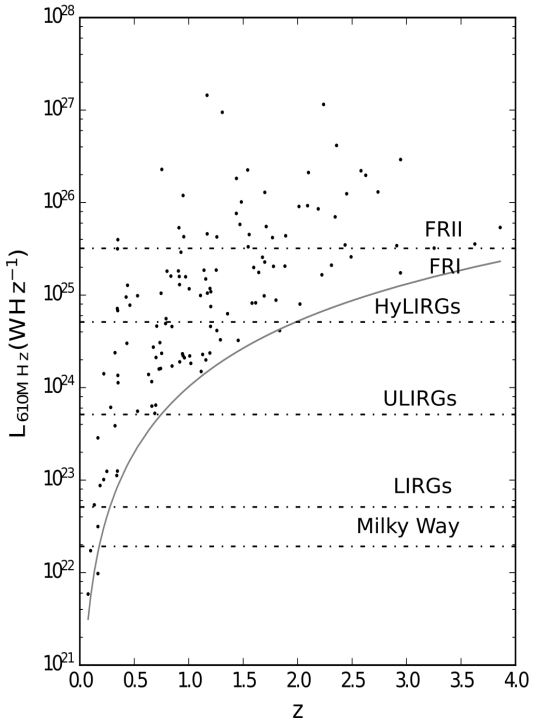

FIGURE 4.5: The 610 MHz luminosity as a function of redshift. Note that these luminosities are underestimated by up to a factor of ≈2 in this preliminary catalog. We use FRII as a shorthand for high-powered radio AGN and FRI for low power radio AGN. For reference we show where different classes of IR luminous star-forming galaxies would lie. We assume SFRs of 4, 10, 100 and 1000 $M_{\odot}yr^{-1}$, respectively for the Milky Way, LIRGs, ULIRGs and HyLIRGs.

whereby Smolčić et al. (2008) find that radio AGN galaxies are preferentially hosted in red ellipticals. Note though that Ivezić et al. (2002) suggest that the dominace of red radio galaxies in flux limited radio samples is merely a result of selection effects.

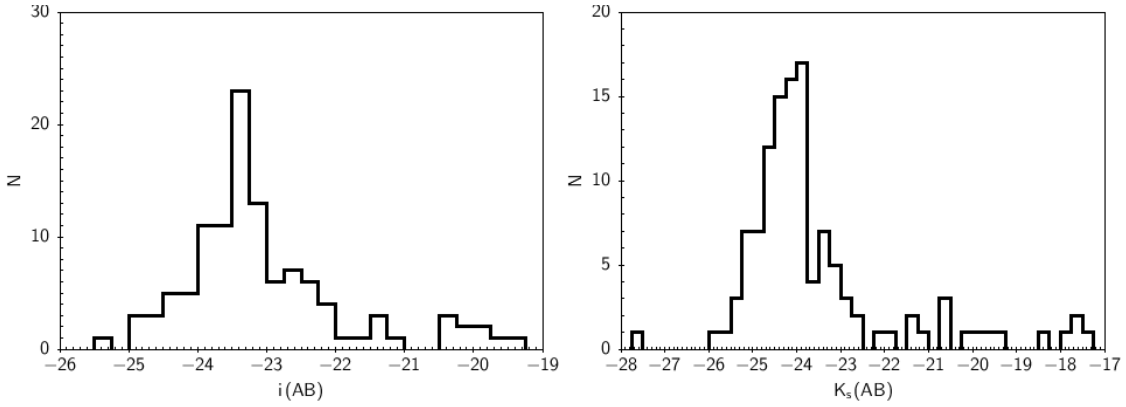

FIGURE 4.6: The i and K_s band magnitudes of our galaxies (Laigle et al. (2016) photometry).

4.4 Summary and Conclusions

We have presented the properties of a preliminary catalog at 610 MHz of the COSMOS field from GMRT data (described in detail in Chapter 3), which will be one of the primary bands of the SKA instrument. This is the first survey of COSMOS at 610 MHz released. COSMOS has a large ancillary dataset (Scoville et al., 2007b; Laigle et al., 2016), as well as deep, high resolution VLA radio imaging at 324 MHz (Smolčić et al., 2014), 1.4 GHz Schinnerer et al. (2010) and 3 GHz (Smolčić et al. in press). This affords us the opportunity to investigate the redshift distribution, optical colors and AGN fraction at 610 MHz[6]. We find that the redshift distributions and AGN fractions, as well as optical colors are in agreement with those seen in the other VLA radio surveys and with the predictions of Smolčić et al. (2008); Wilman et al. (2008); Padovani et al. (2015).

However, based on a comparison of spectral indices, the fluxes in this early release catalog seem to be underestimated (Section 4.2.1). This is in keeping with what we saw in Chapter 3, whereby our fluxes were smaller by a factor of 2 in comparison to the NVSS ones (although this comparison necessitated assuming $\alpha = -0.7$). The properties of our image will of course depend on the calibration method employed, however these flux offsets (although slightly smaller) have also been seen for the sources detected in an image produced with a different calibration method[7] to ours (H. Intema, private communication. We did an antenna based delay correction, H. Intema calibrated the data assuming that the delay offsets were due to ionospheric effects.) on the same GMRT dataset. In the calibration process we observed that point sources were being smeared and attempted to correct for that. However it would seem that these corrections have not been sufficient and source fluxes are still being smeared out to an extent that S_{peak} is being significantly reduced. In addition our low number counts point to many sources falling below the $5\sigma_{local}$ detection threshold we set for SAD. Setting a lower $3\sigma_{local}$ threshold will be one way to attempt to recover lost flux, although we will need to be careful of spurious detections. A 324 MHz image of COSMOS based on GMRT data is being produced by V. Balakrishnan using the same AIPS-based pipeline. Since we will be able to directly compare the fluxes of these sources to the Smolčić et al. (2014) ones,

[6]Previous GMRT 610 MHz surveys e.g Bondi et al. (2007); Ibar et al. (2009); Garn et al. (2008) lacked the ancillary information for such investigations.

[7]Same cataloging routine though

this will help control for instrumental issues and weaknesses in the AIPS-based pipeline.

This catalog is preliminary - we are currently working on correcting for the missing flux and on producing a ($3\,\mathrm{deg}^2$) mosaic centered on the COSMOS field. When this is completed we will have a deep, wide field survey with a large ancillary dataset, courtesy of the COSMOS collaboration, which will be of use for inital characterization of the low frequency radio population that LOFAR and SKA will detect at these wavelengths. In addition this band probes rest-frame 1.4 GHz emission at $z \sim 1.3$ and can be used to study the radio spectral energy distribution and evolution of the infrared radio correlation (Delhaize et al. subm.)

Chapter 5

Summary and Outlook

The aim of the thesis was to investigate the star-forming properties of the radio population in COSMOS. COSMOS (Scoville et al., 2007b) is a 2 deg^2 field containing 2×10^6 galaxies with extensive deep, high resolution panchromatic coverage, in addition to many high quality spectroscopic and photometric redshifts. It has also been surveyed in several radio bands by the VLA, making it ideal for studies of the evolution of the radio galaxy population.

In the early dusty universe, UV and optical emission is highly attenuated, meaning that to study high redshift samples of galaxies, IR and radio measurements are necessary. Although there are extensive IR measurements available they tend to be shallower and of lower resolution than radio ones, particularly in comparison to VLA surveys. Therefore the 1.4 GHz continuum is possibly our best bet to trace SFRs reliably in very distant galaxies. In addition, faint radio-loud (i.e not detected at any other wavelength) AGN seem to become increasingly common at sub-mJy fluxes. Future deep radio surveys such as SKA should detect many of these, as well as starburst galaxies at high redshifts, in addition to extending observations of the main sequence of star forming galaxies at radio wavelengths beyond z$\sim$0.5, which is all that current radio surveys manage with direct detections.

In this thesis we tested the reliability of radio SFR tracers on a sample of radio and IR selected starburst galaxies at high redshifts, as well as testing how well locally calibrated IR SED models of such galaxies represent their high redshift counterparts. These results are summarized in Section 5.1. In Section 5.2 we summarize our work towards a 610 MHz catalog of COSMOS as well as some early results regarding the properties of the detected sources. This catalog complements the

already available VLA 324 MHz, 1.4 GHz and 3 GHz surveys of COSMOS and will be of use for studies of the radio AGN population make-up and evolution, spectral index estimations and probing rest-frame 1.4 GHz emission to better understand the infared radio correlation. We conclude with a way forward in Section 5.3.

5.1 Dust Un-obscured SFR Tracers for High Redshift Starburst Galaxies

The cosmic SFRD is a key tool for astronomers attempting to understand the underlying processes governing galaxy formation and evolution and constrain cosmological models. Reliable SFR calibrations are essential to such studies. There is a host of different calibrations from UV and optical (e.g the Hα line) to IR and radio that are extensively used in the literature - see Calzetti et al. (2007); Kennicutt & Evans (2012) and references therein for an overview.

Many studies have been conducted into the consistency between different tracers (Calzetti, 2001; Hao et al., 2011; Murphy et al., 2011; Leroy et al., 2012; Davies et al., 2016). However most studies thus far have focused on samples of local galaxies, quite often UV/optical tracers[1] and main sequence galaxies (given that most cosmic stellar mass has been built up in galaxies on the main sequence). In the early 2020s the JWST and SKA will start detecting IR and radio galaxies at unprecedented depths and resolutions. Although starburst galaxies are very rare locally, we will expect significant numbers of them in the early universe, and cannot discount that they make a signifcant contribution to the SFRD beyond z$\sim$4. It is now timely to test dust-unbiased SFR tracers out to high redshifts, since these tracers are calibrated on local sample of galaxies, and the underlying physical processes may evolve with cosmic time.

We have tested the reliablilty of the 1.4 GHz radio continuum SFR tracer by comparing it to $\mathrm{SFR_{IR}}$ where the L_{TIR} has been extrapolated from a single MIR or FIR band and a wide variety of the currently available model SED templates. This work was performed on a sample of galaxies in COSMOS out to $z = 2.3$ with

[1] UV and optical surveys have detected some of the highest redshift galaxies to date (Oesch et al., 2016), but emission at those wavelengths is highly extincted in luminous high z galaxies. However, in local, relatively unobscured galaxies, tracers such as Hα are the most reliable since they directly tracer the light from young massive stars.

$>5\sigma$ 1.4GHz, MIPS 24 μm and PACS 100 μm detections and high quality photometric redshifts using the self-consistent calibrations of Murphy et al. (2011). We find that SFR_{IR} obtained by normalising SEDs with MIR or FIR measurements are very dependent on the choice of normalization band and template and evolving with redshift, with offsets of 2 even at $z = 0$ between the SFR_{IR} and the $SFR_{1.4GHz}$ (Section 2.4.1). We controlled for the effects of systematics such as AGN contamination (Section 2.4.2.4), issues with photometric redshifts (Section 2.4.2.3), spectral index (Section 2.4.2.1) and found they were not the main drivers of the disagreement.

Although Elbaz et al. (2011) have suggested that local and high z starbursts have similar IR SEDs (with the high z one merely being scaled up versions of the local), we see evidence that this does not hold true for more extreme radio-selected starbursts. Overall, our galaxies would seem to prefer the features of a local starburst galaxy (Rieke et al. (2009) $10^{12}\,L_{\odot}$) and the broad FIR peak (and cooler T_{dust}) of a main sequence galaxy (Elbaz et al. (2011) or Rieke et al. (2009) $10^{10}\,L_{\odot}$) - as is clear in Figures 2.4 and 2.5. If we select them by offset from the main sequence, those with $R_{SB} \leq 5$ have an IR SED that is well represented by the Elbaz et al. (2011) starburst template. The more extreme starbursts, which make up the majority of the sample would be better represented by a Rieke et al. (2009) $10^{12}\,L_{\odot}$ template. However, in this case, the $SFR_{1.4GHz}$ calibration is overestimated relative to the SFR_{IR}. Delhaize et al. (subm.), Magnelli et al. (2015) and Basu et al. (2015) have presented evidence for an IRRC that evolved with redshift towards lower values, which means that the true $SFR_{1.4GHz}$ for our galaxies would be lower. It seems that a best possible explanation is that, although local starbursts are observed to be compact major mergers (Elbaz et al., 2011), at higher z the population is more diverse, including starburst galaxies that are more extended (Lacki et al., 2010; Magnelli et al., 2015) 'puffy starbursts'. We would expect that such extreme starbursts still exhibit the weak PAH seen in local starburst galaxies, but perhaps have cooler bulk ISM temperatures and have lower values of the IRRC since the cosmic ray scale height is much larger (factor 10). Given the flux limited nature of our sample we are however more sensitive to changes of the IRRC with SFR rather than z.

Sub-mm detected galaxy (SMG) samples seems to contain a large number of puffy starbursts. Since SMGs have been observed to z$\sim$6.3 (Hodge et al., 2013), it is crucial to better characterize the IR SED for high z galaxies and the evolution

of the IRRC if we want to understand their contribution to the SFRD at those redshifts. On the radio side we need to probe the rest frame 1.4 GHz emission out to high z, as well as understand how the radio population make-up evolves, and the effects of selection biases on the results presented in studies conducted thus far. This leads us to our second project discussed in the following section.

5.2 610MHz Continuum Observations of COSMOS

Several 610 MHz surveys have been conducted with the GMRT; Bondi et al. (2007); Tasse et al. (2007); Garn et al. (2008); Ibar et al. (2009); Ainsworth et al. (2016). Ours is the first in the COSMOS field and, along with the Smolčić et al. (2014) 324 MHz surveys, bridges the gap between the higher frequency surveys of Schinnerer et al. (2004, 2007, 2010) and Smolčić et al. in press at 1.4 GHz and 3 GHz respectively and the lower frequency bands of LOFAR. Given that COSMOS has such excellent radio coverage as well as extensive photometry this makes it, in its current form, an ideal testing ground for the upcoming SKA instrument surveys, of which 610 MHz will be one of the main bands. The unique panchromatic coverage of COSMOS means we have z and ancillary photometry for our sample that the previous 610 MHz surveys lacked, which allows us to look at the redshift distribution, colors and SF/AGN population breakdowns.

The radio popluation is AGN dominated above (1.4 GHz) mJy flux levels (Smolčić et al., 2008; Wilman et al., 2008). At $<$1 mJy faint radio loud AGN contribute at significant levels, but below 0.1 mJy it seems radio quiet AGN take over (Padovani et al., 2015). Probing high redshift faint radio samples with low frequency bands, which are less affected by synchrotron losses, will help in understanding the evolving AGN population makeup, and hence the physical processes governing radio AGN activity. Having multiple radio band measurements allows one to study the spectral indices of the radio population as a function of z and flux. In particular authors such as De Breuck et al. (2000) find that ultra steep radio spectra (USS) $\alpha < -1.3$ can be used to identify radio galaxies lying at $z \sim 1$ and higher, which have not been detected at any other wavelengths and thus have no z measurements. Since radio galaxies tend to be massive red ellipticals, USS can be used to trace the large scale structure at z$\sim$1. The 610 MHz band will also be of use in

studies of the evolution of the spectral shape of the radio SED and probing the rest-frame 1.4 GHz emission (at z∼1.3 it shifts into the 610 MHz band) to better understand radio emission from star formation on cosmic timescales.

The observations of the COSMOS field presented here were taken as part of the projects 10HRK01 and 11HRK01 (PI H.R Klöckner) in 2007. The full COSMOS field was covered by 19 pointings (Figure 3.1), each being observed for a total of two hours except in the case of the centre-most pointing which was targeted for more than four hours over the course of eight days in February and March. An AIPS based pipeline, developed specifically to reduce GMRT data by Hans-Rainer Klöckner, was used to perform the calibration, imaging and cataloging (the cataloging routine was provided by Mauch et al., 2013). This is decribed in more detail in Sections 3.2.1, 3.2.2 and 3.3.1. We first perfomed a manual inspection of the data to remove dead antennas and baselines severely affected by RFI. After that we performed an antenna-based delay calibration, self calibration and baseline-based calibration, before imaging each pointing separately to a common resolution and mosaicing (first splitting the pointings into facets). The final mosaic is still under construction, but in Chapter 4 we presented the early results from an image of the central 1.4 $\deg^2$ pointing produced by Hans-Rainer Klöeckner. This image has rms of 45μJy/beam and a resolution of 8.8″×6.4″. 220 sources were detected, 18 of which are multiple component. We found that there was a significant issue with underestimated fluxes (Sections 3.3.2.2 and 4.2). It seems that resolution bias is our main problem, whereby sources are being smeared out, causing some S_{peak} to fall below the detection threshold of the cataloger and integrated fluxes of extended sources to be underestimated. We are currently attempting to understand how the pipeline can be adapted to properly correct for this. Nevertheless we see could explore some of the properties of the sources (Section 4.3) by performing a cross match with the 3 GHz catalog of Smolčić et al. (in press). We found that most our sources clustered at z ∼1, with a signifcant tail to z∼4 and that the sample was AGN dominated, in agreement with predictions for the radio galaxy population at those flux levels.

Our 610 MHz fluxes are not suffciently accurate to investigate spectral indices in detail, nor the radio source sounts at 610 MHz in COSMOS. Until the Square Kilometer Array (SKA Norris et al., 2015) comes online in 5 years, this is the best we have in this band for COSMOS. Our current recourse is to attempt to better understand the issues with the data and the instrument, as well as any

flaws in the AIPS-based pipeline that may be the root cause of these offsets. We are currently working on this for the full 3 deg^2 mosaic. In addition a 324 MHz image of COSMOS based on GMRT data is being produced by V. Balakrishnan using the same AIPS-based pipeline. Since we will be able to directly compare the fluxes of these sources to the Smolčić et al. (2014) ones, this will help control for instrumental issues and weaknesses in the AIPS-based pipeline. Failing that, new surveys with the upgraded GMRT can provide better fluxes between now and first light of SKA. Single dish measurement of some of the sources could help correct the fluxes. They will of cource be of much lower resolution but could aid efforts to understand instrumental effects in our higher resolution survey data[2]. Currently, the only single dish telescope operating at 610 MHz that we are aware of is the Five Hundred Meter Aperture Spherical Telescope (FAST) which saw first light recently. Failing that, the Westerbork synthesis radio telescope could be used.

5.3 Future Prospects for Studies of Radio Galaxy Populations

It is clear that many open questions remain about the properties of radio galaxies. The flux limited nature of most radio selected samples to date has made it difficult to disentangle the effects of luminosity evolution from cosmic evolution in radio galaxy populations.

The redshift evolution of the IRRC seen by Delhaize et al. (in prep.) and Magnelli et al. (2015) could be either a true redshift evolution, or simply an evolution with SFR (Tabatabaei et al. subm.). It will affect calibrations of radio SFRs and could indicate that high redshift starburst galaxy populations consist of a significant fraction of galaxies that are puffier, or more extended, than their local counterparts (which are observed to be almost exclusively compact major mergers). Thus their IR SEDs would not be well represented at all by the locally calibrated templates. The IR SEDs of galaxies offset from the main sequence and even of higher redshift main sequence galaxies are not fully understood. A dedicated effort is needed to model them. The James Webb Space Telescope (JWST Clampin, 2008), which will observe from 0.6-28 μm, and the Space Infrared Telescope for Cosmology and

[2]Higher survey resolution means we can better associate optical counterparts with our galaxies.

Astrophysics (SPICA Sibthorpe et al., 2016) covering 10-100μm, together will be able to characterize the IR SED of galaxies out to redshifts as high as 6. This will allow the development of new accurate IR SED libraries for high redshift galaxy populations.

On the radio side, the Square Kilometer Array (SKA Norris et al., 2015), and its precursors such as ASKAP, will reasonably reach flux levels a factor 10 deeper than current radio surveys, and increase the total number of radio sources detected to date by factors of 20 or more. So far, free-free radio emission has been impractical to observe at high z. The SKA will change that and allow for the first time to *directly*[3] trace star formation at radio wavelengths in high redshift galaxies (as will the upgraded VLA). We can expect many serendipitous discoveries of new radio galaxy populations, as well as the opportunity to study in depth the form and evolution of their radio SEDs. In the meantime, dedicated searches for high redshift submillimeter galaxies, e.g with the IRAM Plateau de Bure interferometer (PdBI) and ALMA would aid in understanding the contribution of starbursts to the SFRD as well as the possible evolution of the IRRC.

[3]Free-free emission is directly related to the ionizing radiation of young massive stars. Non-thermal emission indirectly traces star formation via synchrotron emission in the supernova shocks of these stars when they expire.

Appendix A

A comparison $\mathrm{SFR_{IR}}$ from Publically Available SEDs to $\mathrm{SFR_{1.4GHz}}$

In the main text (Chapter 2) we presented the results for a representative subset of SEDs. Here, we show the $\mathrm{SFR_{IR}}$ for the full set of templates described in Section 2.3.2.1 for the readers edification.

A.1 MIPS 24μm Extrapolated $\mathrm{SFR_{IR}}$

In the following figures, the colored lines represent the $\mathrm{SFR_{IR}}$ from the $24\,\mu m$ normalized SEDs and the gray points the $\mathrm{SFR_{1.4GHz}}$ (with the median in black). We present the plots as a ratio of the measured νL_ν at $24\,\mu m$, i.e $L(24\,\mu m)$, to the SFR to demonstrate how the PAH features shift into the MIPS filter.

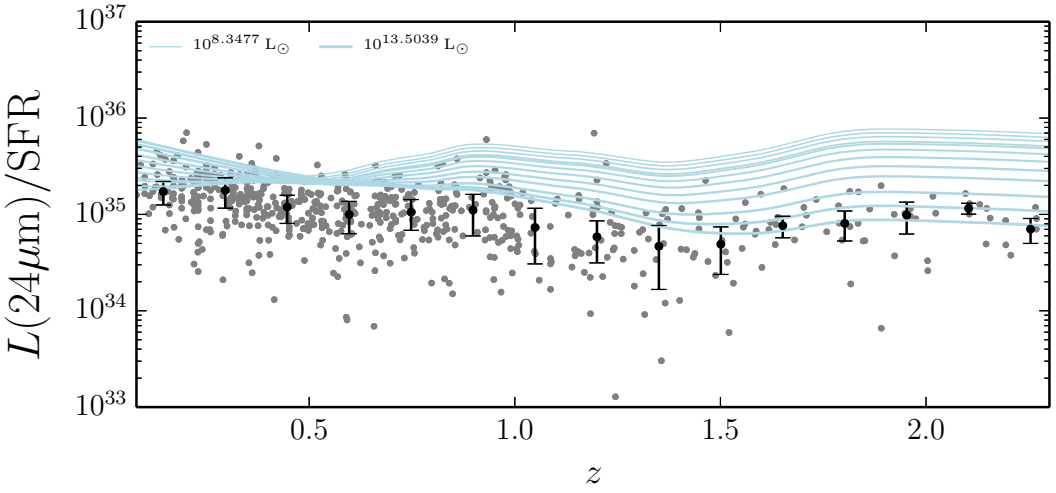

FIGURE A.1: $L(24\,\mu m)/\mathrm{SFR}$ for the Dale & Helou (2002) SED models. $L(24\,\mu m)$ is from the MIPS measurements and in the case of the pale blue lines the denominator is $\mathrm{SFR}_{24\mu\mathrm{m}}$ and for the gray points it's $\mathrm{SFR}_{1.4\mathrm{GHz}}$, with the median in black.

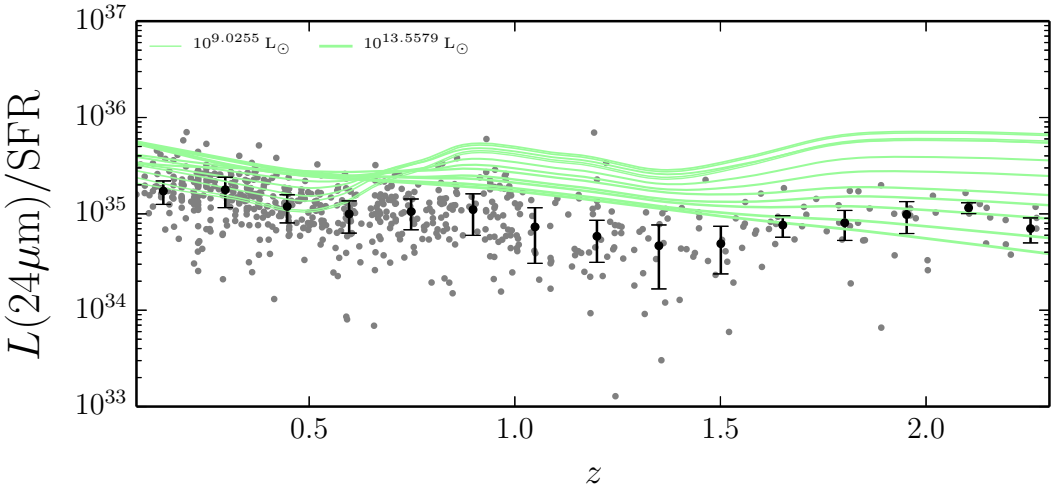

FIGURE A.2: $L(24\,\mu m)/\mathrm{SFR}$ for the Chary & Elbaz (2001) SED models. $L(24\,\mu m)$ is from the MIPS measurements and in the case of the green lines the denominator is $\mathrm{SFR}_{24\mu\mathrm{m}}$ and for the gray points it's $\mathrm{SFR}_{1.4\mathrm{GHz}}$, with the median in black.

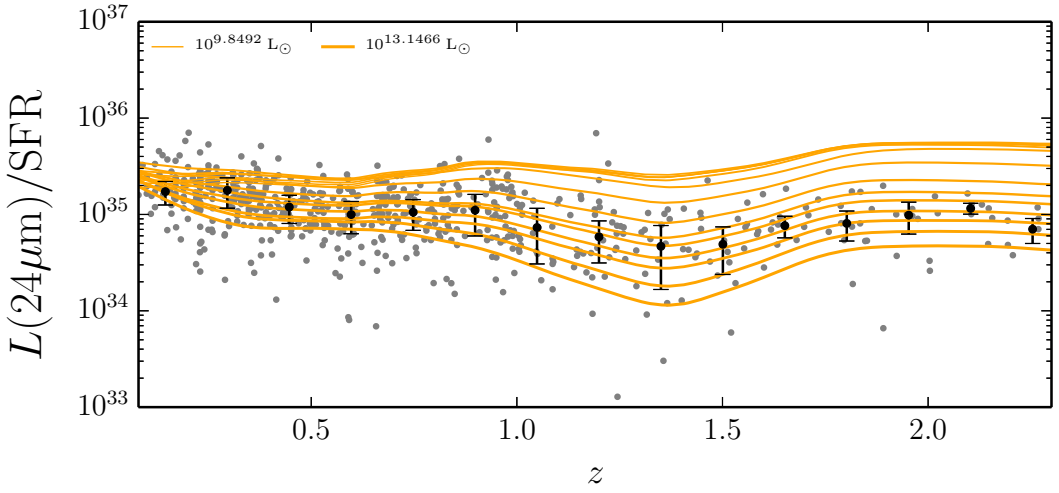

FIGURE A.3: $L(24\,\mu m)/\mathrm{SFR}$ for the Rieke et al. (2009) SED models. $L(24\,\mu m)$ is from the MIPS measurements and in the case of the orange lines the denominator is $\mathrm{SFR}_{24\mu\mathrm{m}}$ and for the gray points it's $\mathrm{SFR}_{1.4\mathrm{GHz}}$, with the median in black.

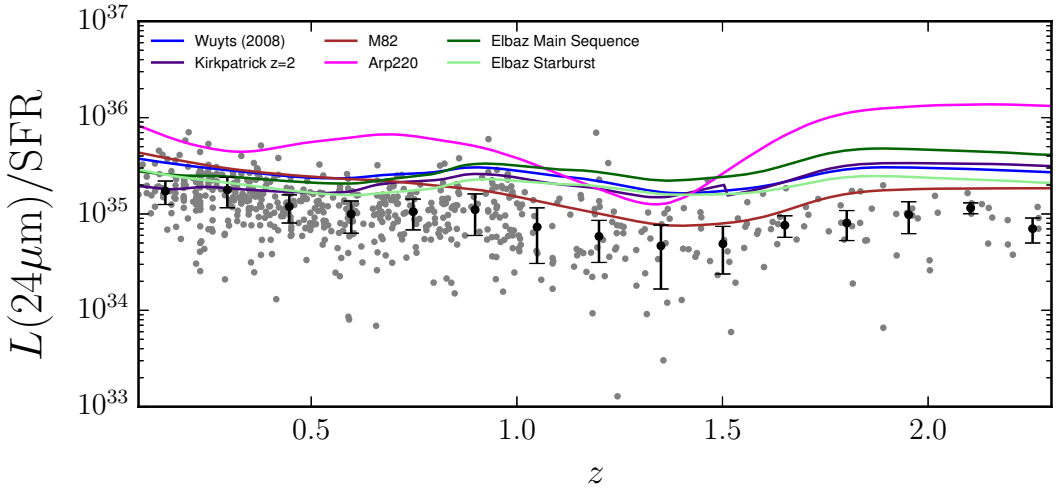

FIGURE A.4: $L(24\,\mu m)/\mathrm{SFR}$ for the universal SED models. $L(24\,\mu m)$ is from the MIPS measurements and in the case of the colored lines the denominator is $\mathrm{SFR}_{24\mu\mathrm{m}}$ and for the gray points it's $\mathrm{SFR}_{1.4\mathrm{GHz}}$, with the median in black.

A.2 PACS 100μm Extrapolated $\mathrm{SFR_{IR}}$

In the following figures, the colored lines represent the $\mathrm{SFR_{IR}}$ from the 100 μm normalized SEDs and the gray points the $\mathrm{SFR_{1.4GHz}}$ (with the median in black). We present the plots as a ratio of the measured νL_ν at 100μm, i.e $L(100\mu m)$.

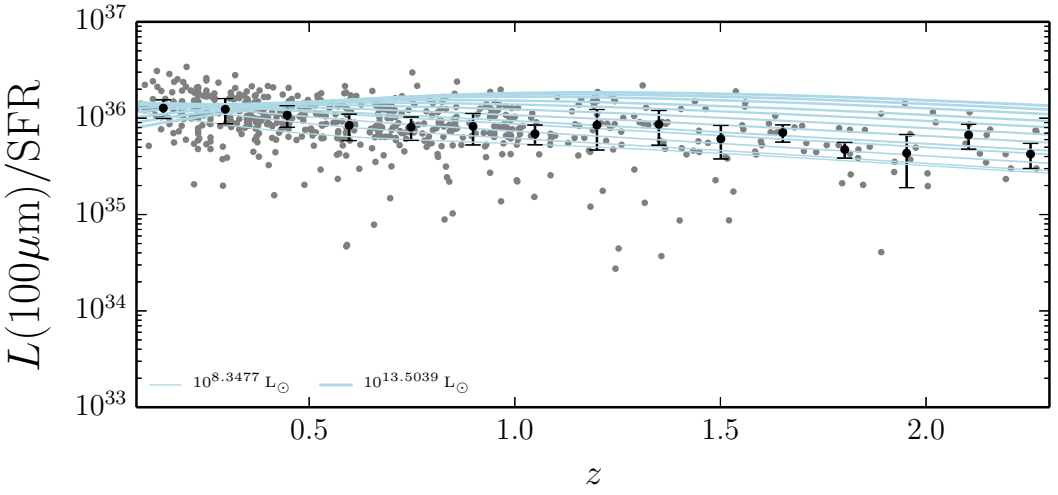

FIGURE A.5: $L(100\,\mu m)/\mathrm{SFR}$ for the Dale & Helou (2002) SED models. $L(100\,\mu m)$ is from the PACS measurements and in the case of the pale blue lines the denominator is $\mathrm{SFR_{100\mu m}}$ and for the gray points it's $\mathrm{SFR_{1.4GHz}}$, with the median in black.

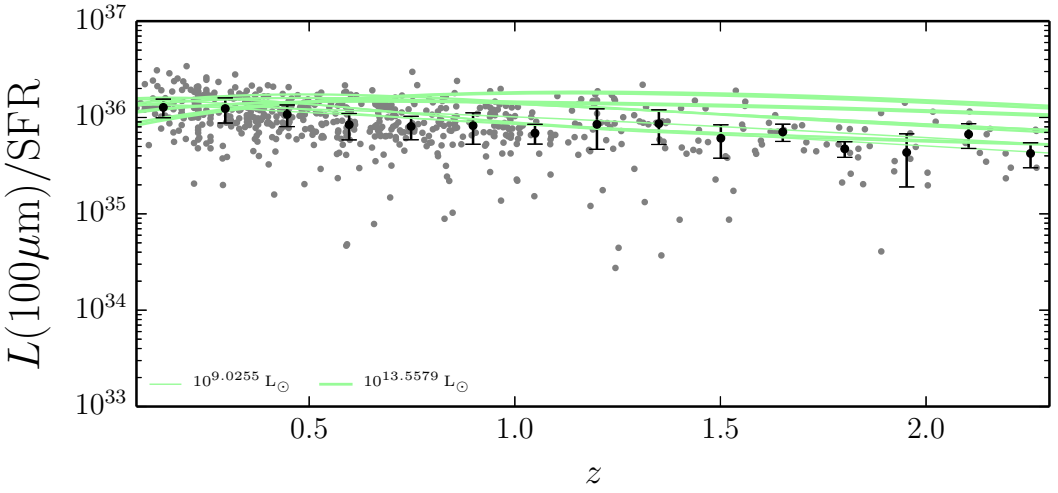

FIGURE A.6: $L(100\,\mu m)/\mathrm{SFR}$ for the Chary & Elbaz (2001) SED models. $L(100\,\mu m)$ is from the PACS measurements and in the case of the green lines the denominator is $\mathrm{SFR_{100\mu m}}$ and for the gray points it's $\mathrm{SFR_{1.4GHz}}$, with the median in black.

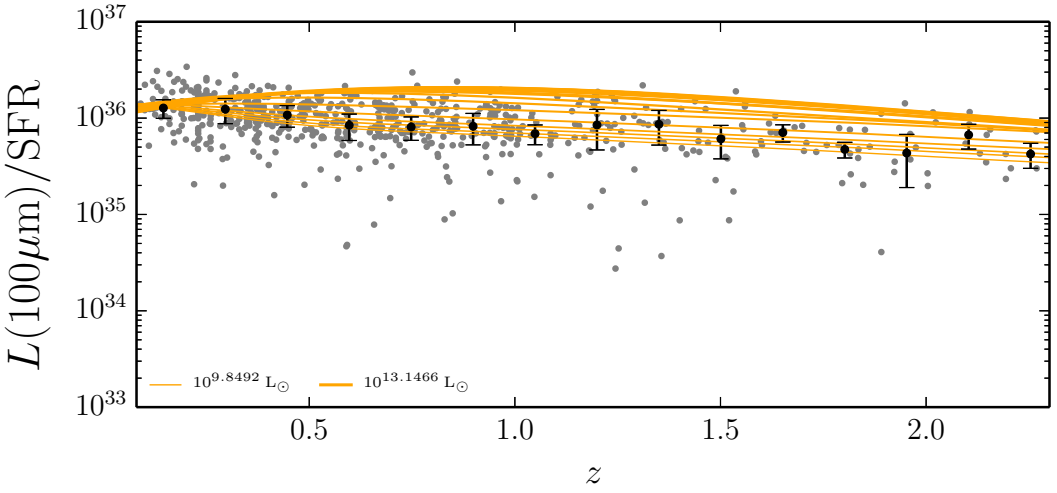

FIGURE A.7: $L(100\,\mu m)/\mathrm{SFR}$ for the Rieke et al. (2009) SED models. $L(100\,\mu m)$ is from the PACS measurements and in the case of the orange lines the denominator is $\mathrm{SFR}_{100\mu\mathrm{m}}$ and for the gray points it's $\mathrm{SFR}_{1.4\mathrm{GHz}}$, with the median in black.

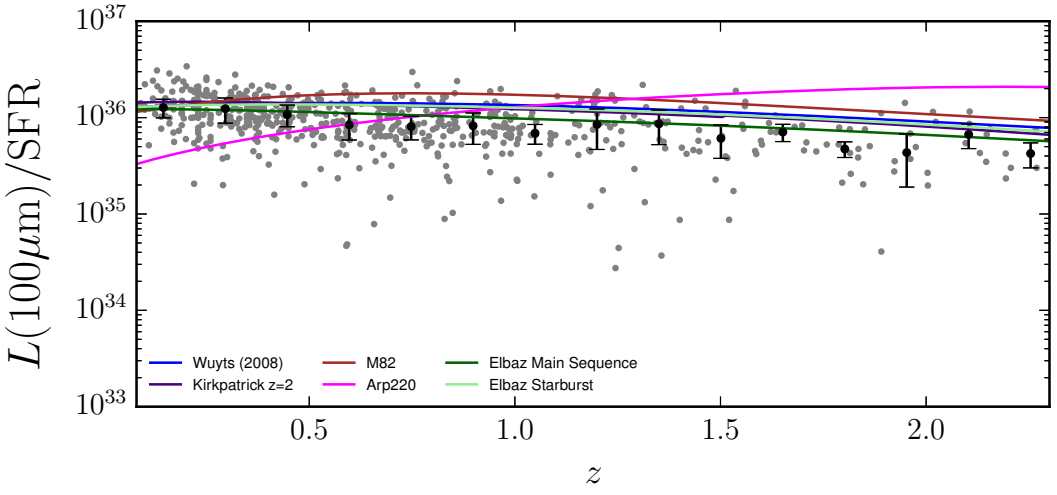

FIGURE A.8: $L(100\,\mu m)/\mathrm{SFR}$ for the universal SED models. $L(100\,\mu m)$ is from the PACS measurements and in the case of the colored lines the denominator is $\mathrm{SFR}_{100\mu\mathrm{m}}$ and for the gray points it's $\mathrm{SFR}_{1.4\mathrm{GHz}}$, with the median in black.

A.3 IR Colors

In the following figures, the colored lines represent the $L(24\mu m)/L(100\mu m)$ from the SEDs and the grey points the measured values, with the median in black.

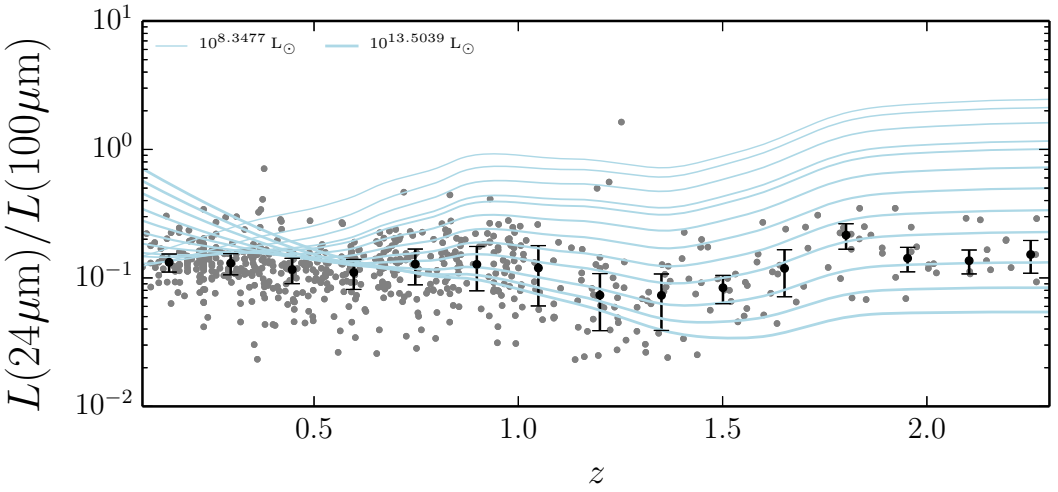

FIGURE A.9: $L(24\,\mu m)/L(100\,\mu m)$ for the Dale & Helou (2002) SED models. The colored lines represent the luminosity band ratio from the templates and the gray points the measurements, with the median in black.

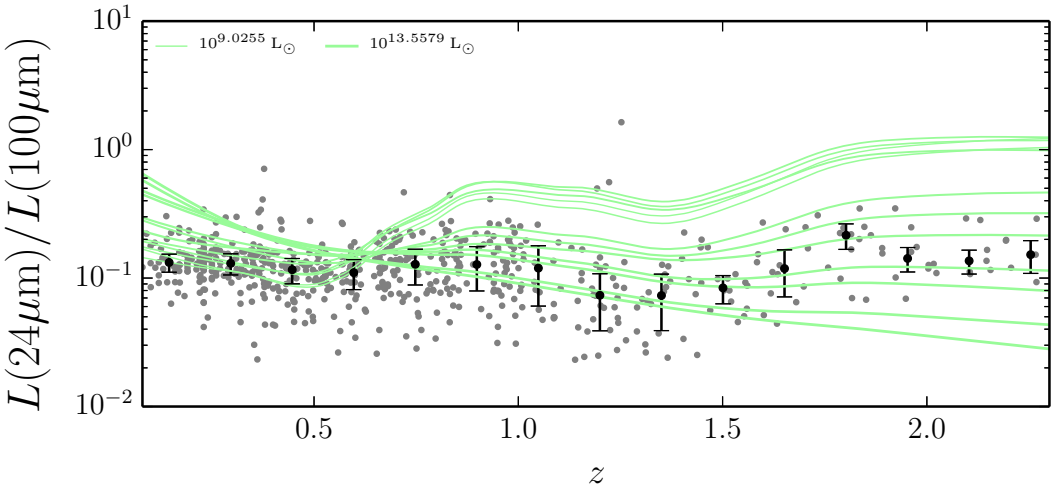

FIGURE A.10: $L(24\,\mu m)/L(100\mu m)$ for the Chary & Elbaz (2001) SED models. The colored lines represent the luminosity band ratio from the templates and the gray points the measurements, with the median in black.

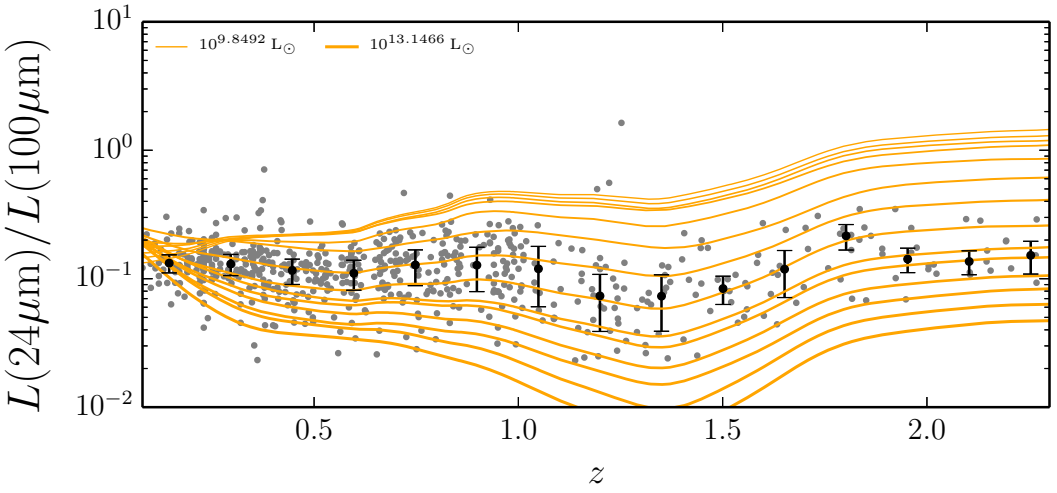

FIGURE A.11: $L(24\,\mu m)/L(100\mu m)$ for the Rieke et al. (2009) SED models. The colored lines represent the luminosity band ratio from the templates and the gray points the measurements, with the median in black.

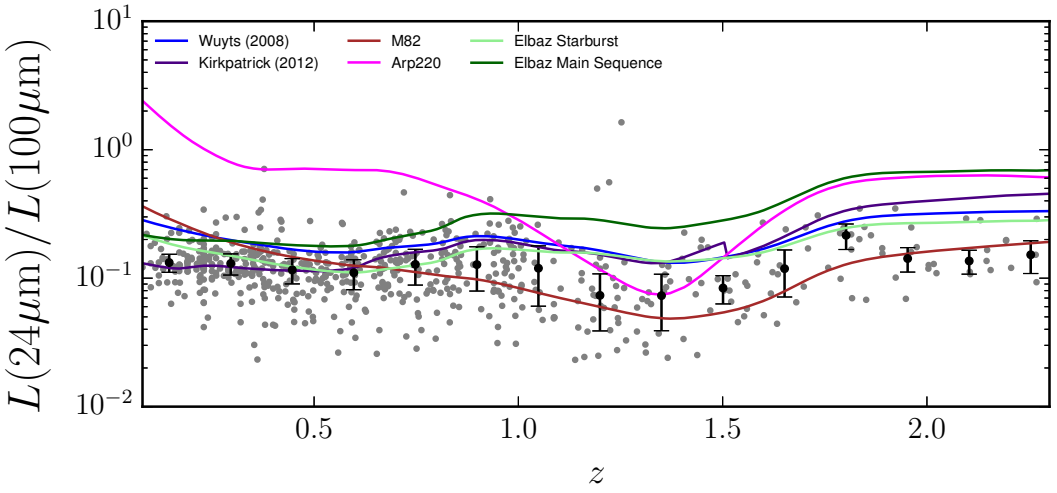

FIGURE A.12: $L(24\,\mu m)/L(100\mu m)$ for the universal SED models. The colored lines represent the luminosity band ratio from the templates and the gray points the measurements, with the median in black.

Bibliography

Ade, P. A. R., et al. 2015, Planck 2015 results. XIII. Cosmological parameters, arXiv:1502.01589

Ainsworth, R. E., Coughlan, C. P., Green, D. A., Scaife, A. M. M., & Ray, T. P. 2016, A GMRT survey of regions towards the Taurus molecular cloud at 323 and 608 MHz, MNRAS, 462, 2904

Arnouts, S., Moscardini, L., Vanzella, E., et al. 2002, Measuring the redshift evolution of clustering: the Hubble Deep Field South, MNRAS, 329, 355

Basu, A., Wadadekar, Y., Beelen, A., et al. 2015, Radio-Far-infrared Correlation in Blue Cloud Galaxies with $0 < z < 1.2$, ApJ, 803, 51

Becker, R. H., White, R. L., & Helfand, D. J. 1995, The FIRST Survey: Faint Images of the Radio Sky at Twenty Centimeters, ApJ, 450, 559

Bell, E. F. 2003, Estimating Star Formation Rates from Infrared and Radio Luminosities: The Origin of the Radio-Infrared Correlation, ApJ, 586, 794

Bertoldi, F., Carilli, C., Aravena, M., et al. 2007, COSBO: The MAMBO 1.2 Millimeter Imaging Survey of the COSMOS Field, ApJS, 172, 132

Bondi, M., Ciliegi, P., Venturi, T., et al. 2007, The VVDS-VLA deep field. III. GMRT observations at 610 MHz and the radio spectral index properties of the sub-mJy population, A&A, 463, 519

Bongiorno, A., Mignoli, M., Zamorani, G., et al. 2010, The [O iii] emission line luminosity function of optically selected type-2 AGN from zCOSMOS, A&A, 510, A56

Bourke, S., van Langevelde, H. J., Torstensson, K., & Golden, A. 2013, An AIPS-based, distributed processing method for large radio interferometric datasets, Experimental Astronomy, 36, 59

Brusa, M., Civano, F., Comastri, A., et al. 2010, The XMM-Newton Wide-field Survey in the Cosmos Field (XMM-COSMOS): Demography and Multiwavelength Properties of Obscured and Unobscured Luminous Active Galactic Nuclei, ApJ, 716, 348

Bruzual, G., & Charlot, S. 2003, Stellar population synthesis at the resolution of 2003, MNRAS, 344, 1000

Buat, V., Iglesias-Páramo, J., Seibert, M., et al. 2005, Dust Attenuation in the Nearby Universe: A Comparison between Galaxies Selected in the Ultraviolet and in the Far-Infrared, ApJ, 619, L51

Calzetti, D. 2001, The Dust Opacity of Star-forming Galaxies, PASP, 113, 1449

Calzetti, D., Kennicutt, R. C., Engelbracht, C. W., et al. 2007, The Calibration of Mid-Infrared Star Formation Rate Indicators, ApJ, 666, 870

Capak, P., Aussel, H., Ajiki, M., et al. 2007, The First Release COSMOS Optical and Near-IR Data and Catalog, ApJS, 172, 99

Caputi, K. I., Lagache, G., Yan, L., et al. 2007, The Infrared Luminosity Function of Galaxies at Redshifts z = 1 and z $\sim$ 2 in the GOODS Fields, ApJ, 660, 97

Chary, R., & Elbaz, D. 2001, Interpreting the Cosmic Infrared Background: Constraints on the Evolution of the Dust-enshrouded Star Formation Rate, ApJ, 556, 562

Chatzichristou, E. T., & Goods Team. 2004, Deep surveys of the obscured universe: GOODS, Advances in Space Research, 34, 661

Civano, F., Elvis, M., Brusa, M., et al. 2012, The Chandra COSMOS Survey. III. Optical and Infrared Identification of X-Ray Point Sources, ApJS, 201, 30

Civano, F., Marchesi, S., Comastri, A., et al. 2016, The Chandra Cosmos Legacy Survey: Overview and Point Source Catalog, ApJ, 819, 62

Clampin, M. 2008, The James Webb Space Telescope (JWST), Advances in Space Research, 41, 1983

Condon, J. J. 1992, Radio emission from normal galaxies, ARA&A, 30, 575

—. 1997, Errors in Elliptical Gaussian FITS, PASP, 109, 166

Condon, J. J., Cotton, W. D., Greisen, E. W., et al. 1998, The NRAO VLA Sky Survey, AJ, 115, 1693

da Cunha, E., Charmandaris, V., Díaz-Santos, T., et al. 2010, Exploring the physical properties of local star-forming ULIRGs from the ultraviolet to the infrared, A&A, 523, A78

Daddi, E., Dickinson, M., Chary, R., et al. 2005, The Population of BzK-selected ULIRGs at z $\sim$ 2, ApJ, 631, L13

Daddi, E., Dickinson, M., Morrison, G., et al. 2007, Multiwavelength Study of Massive Galaxies at z$\sim$2. I. Star Formation and Galaxy Growth, ApJ, 670, 156

Daddi, E., Bournaud, F., Walter, F., et al. 2010, Very High Gas Fractions and Extended Gas Reservoirs in z = 1.5 Disk Galaxies, ApJ, 713, 686

Dale, D. A., & Helou, G. 2002, The Infrared Spectral Energy Distribution of Normal Star-forming Galaxies: Calibration at Far-Infrared and Submillimeter Wavelengths, ApJ, 576, 159

Dale, D. A., Helou, G., Contursi, A., Silbermann, N. A., & Kolhatkar, S. 2001, The Infrared Spectral Energy Distribution of Normal Star-forming Galaxies, ApJ, 549, 215

Dale, D. A., Gil de Paz, A., Gordon, K. D., et al. 2007, An Ultraviolet-to-Radio Broadband Spectral Atlas of Nearby Galaxies, ApJ, 655, 863

Dale, D. A., Aniano, G., Engelbracht, C. W., et al. 2012, Herschel Far-infrared and Submillimeter Photometry for the KINGFISH Sample of nearby Galaxies, ApJ, 745, 95

Davies, L. J. M., Driver, S. P., Robotham, A. S. G., et al. 2016, GAMA/H-ATLAS: a meta-analysis of SFR indicators - comprehensive measures of the SFR-M_* relation and cosmic star formation history at z $<$ 0.4, MNRAS, 461, 458

De Breuck, C., van Breugel, W., Röttgering, H. J. A., & Miley, G. 2000, A sample of 669 ultra steep spectrum radio sources to find high redshift radio galaxies, A&AS, 143, 303

de Jong, T., Klein, U., Wielebinski, R., & Wunderlich, E. 1985, Radio continuum and far-infrared emission from spiral galaxies - A close correlation, A&A, 147, L6

de Zotti, G., Massardi, M., Negrello, M., & Wall, J. 2010, Radio and millimeter continuum surveys and their astrophysical implications, A$AR, 18, 1

Desai, V., Armus, L., Spoon, H. W. W., et al. 2007, PAH Emission from Ultraluminous Infrared Galaxies, ApJ, 669, 810

Donley, J. L., Koekemoer, A. M., Brusa, M., et al. 2012, Identifying Luminous Active Galactic Nuclei in Deep Surveys: Revised IRAC Selection Criteria, ApJ, 748, 142

Elbaz, D., Daddi, E., Le Borgne, D., et al. 2007, The reversal of the star formation-density relation in the distant universe, A&A, 468, 33

Elbaz, D., Hwang, H. S., Magnelli, B., et al. 2010, Herschel unveils a puzzling uniformity of distant dusty galaxies, A&A, 518, L29

Elbaz, D., Dickinson, M., Hwang, H. S., et al. 2011, GOODS-Herschel: an infrared main sequence for star-forming galaxies, A&A, 533, A119

Elvis, M., Civano, F., Vignali, C., et al. 2009, The Chandra COSMOS Survey. I. Overview and Point Source Catalog, ApJS, 184, 158

Faber, S. M., Willmer, C. N. A., Wolf, C., et al. 2007, Galaxy Luminosity Functions to z$\sim$1 from DEEP2 and COMBO-17: Implications for Red Galaxy Formation, ApJ, 665, 265

Garn, T., Green, D. A., Riley, J. M., & Alexander, P. 2008, A 610-MHz survey of the Lockman Hole with the Giant Metrewave Radio Telescope - I. Observations, data reduction and source catalogue for the central 5 deg^2, MNRAS, 387, 1037

Genzel, R., Tacconi, L. J., Gracia-Carpio, J., et al. 2010, A study of the gas-star formation relation over cosmic time, MNRAS, 407, 2091

González, V., Labbé, I., Bouwens, R. J., et al. 2010, The Stellar Mass Density and Specific Star Formation Rate of the Universe at z$\sim$7, ApJ, 713, 115

Greisen, E. W. 2003, AIPS, the VLA, and the VLBA, Information Handling in Astronomy - Historical Vistas, 285, 109

Groves, B., Krause, O., Sandstrom, K., et al. 2012, The heating of dust by old stellar populations in the bulge of M31, MNRAS, 426, 892

Gruppioni, C., Pozzi, F., Rodighiero, G., et al. 2013, The Herschel PEP/HerMES luminosity function - I. Probing the evolution of PACS selected Galaxies to z $\sim$ 4, MNRAS, 432, 23

Hao, C.-N., Kennicutt, R. C., Johnson, B. D., et al. 2011, Dust-corrected Star Formation Rates of Galaxies. II. Combinations of Ultraviolet and Infrared Tracers, ApJ, 741, 124

Hasinger, G., Cappelluti, N., Brunner, H., et al. 2007, The XMM-Newton Wide-Field Survey in the COSMOS Field. I. Survey Description, ApJS, 172, 29

Heckman, T. M., & Best, P. N. 2014, The Coevolution of Galaxies and Supermassive Black Holes: Insights from Surveys of the Contemporary Universe, ARA%A, 52, 589

Helou, G., Soifer, B. T., & Rowan-Robinson, M. 1985, Thermal infrared and nonthermal radio - Remarkable correlation in disks of galaxies, ApL, 298, L7

Hickox, R. C., Jones, C., Forman, W. R., et al. 2009, Host Galaxies, Clustering, Eddington Ratios, and Evolution of Radio, X-Ray, and Infrared-Selected AGNs, ApJ, 696, 891

Hodge, J. A., Karim, A., Smail, I., et al. 2013, An ALMA Survey of Submillimeter Galaxies in the Extended Chandra Deep Field South: Source Catalog and Multiplicity, AJ, 768, 91

Hsieh, B.-C., Wang, W.-H., Hsieh, C.-C., et al. 2012, The Taiwan ECDFS Near-Infrared Survey: Ultra-deep J and K_S Imaging in the Extended Chandra Deep Field-South, ApJS, 203, 23

Ibar, E., Ivison, R. J., Biggs, A. D., et al. 2009, Deep multi-frequency radio imaging in the Lockman Hole using the GMRT and VLA - I. The nature of the sub-mJy radio population, MNRAS, 397, 281

Ilbert, O., Capak, P., Salvato, M., et al. 2009, Cosmos Photometric Redshifts with 30-Bands for 2-deg^2, ApJ, 690, 1236

Ilbert, O., McCracken, H. J., Le Fèvre, O., et al. 2013, Mass assembly in quiescent and star-forming galaxies since z $\sim$ 4 from UltraVISTA, A&A, 556, A55

Ivezić, Ž., Menou, K., Knapp, G. R., et al. 2002, Optical and Radio Properties of Extragalactic Sources Observed by the FIRST Survey and the Sloan Digital Sky Survey, AJ, 124, 2364

Karim, A., Schinnerer, E., Martínez-Sansigre, A., et al. 2011, The Star Formation History of Mass-selected Galaxies in the COSMOS Field, ApJ, 730, 61

Kauffmann, G., Heckman, T. M., White, S. D. M., et al. 2003, Stellar masses and star formation histories for 10^5 galaxies from the Sloan Digital Sky Survey, MNRAS, 341, 33

Kennicutt, R. C., & Evans, N. J. 2012, Star Formation in the Milky Way and Nearby Galaxies, ARA&A, 50, 531

Kennicutt, Jr., R. C. 1998, The Global Schmidt Law in Star-forming Galaxies, ApJ, 498, 541

Kennicutt, Jr., R. C., Hao, C.-N., Calzetti, D., et al. 2009, Dust-corrected Star Formation Rates of Galaxies. I. Combinations of Hα and Infrared Tracers, ApJ, 703, 1672

Kettenis, M., & Sipior, M. 2012, ParselTongue: AIPS Python Interface, Astrophysics Source Code Library, ascl:1208.020

Kirkpatrick, A., Pope, A., Alexander, D. M., et al. 2012, GOODS-Herschel: Impact of Active Galactic Nuclei and Star Formation Activity on Infrared Spectral Energy Distributions at High Redshift, ApJ, 759, 139

Koekemoer, A. M., Aussel, H., Calzetti, D., et al. 2007, The COSMOS Survey: Hubble Space Telescope Advanced Camera for Surveys Observations and Data Processing, ApJS, 172, 196

Krolik, J. H., & Chen, W. 1991, Steep radio spectra in high-redshift radio galaxies, AJ, 102, 1659

Kroupa, P. 2001, On the variation of the initial mass function, MNRAS, 322, 231

Lacki, B. C., & Thompson, T. A. 2010, The Physics of the Far-infrared-Radio Correlation. II. Synchrotron Emission as a Star Formation Tracer in High-redshift Galaxies, ApJ, 717, 196

Lacki, B. C., Thompson, T. A., & Quataert, E. 2010, The Physics of the Far-infrared-Radio Correlation. I. Calorimetry, Conspiracy, and Implications, ApJ, 717, 1

Laigle, C., McCracken, H. J., Ilbert, O., et al. 2016, The COSMOS2015 Catalog: Exploring the $1 < z < 6$ Universe with Half a Million Galaxies, ApJS, 224, 24

Le Floc'h, E., Papovich, C., Dole, H., et al. 2005, Infrared Luminosity Functions from the Chandra Deep Field-South: The Spitzer View on the History of Dusty Star Formation at $0 < z < 1$, ApJ, 632, 169

Le Floc'h, E., Aussel, H., Ilbert, O., et al. 2009, Deep Spitzer 24 μm COSMOS Imaging. I. The Evolution of Luminous Dusty Galaxies - Confronting the Models, ApJ, 703, 222

Leitherer, C., Schaerer, D., Goldader, J. D., et al. 1999, Starburst99: Synthesis Models for Galaxies with Active Star Formation, ApJS, 123, 3

Leroy, A. K., Bigiel, F., de Blok, W. J. G., et al. 2012, Estimating the Star Formation Rate at 1 kpc Scales in nearby Galaxies, AJ, 144, 3

Lilly, S. J., Le Fevre, O., Hammer, F., & Crampton, D. 1996, The Canada-France Redshift Survey: The Luminosity Density and Star Formation History of the Universe to Z approximately 1, ApJ, 460, L1

Lilly, S. J., Le Fèvre, O., Renzini, A., et al. 2007, zCOSMOS: A Large VLT/VIMOS Redshift Survey Covering $0 < z < 3$ in the COSMOS Field, ApJS, 172, 70

Lutz, D., Poglitsch, A., Altieri, B., et al. 2011, PACS Evolutionary Probe (PEP) - A Herschel key program, A&A, 532, A90

Madau, P., & Dickinson, M. 2014, Cosmic Star-Formation History, ARA&A, 52, 415

Magdis, G. E., Rigopoulou, D., Huang, J.-S., & Fazio, G. G. 2010, On the stellar masses of IRAC detected Lyman Break Galaxies at z$\sim$3, MNRAS, 401, 1521

Magdis, G. E., Daddi, E., Béthermin, M., et al. 2012, The Evolving Interstellar Medium of Star-forming Galaxies since $z = 2$ as Probed by Their Infrared Spectral Energy Distributions, ApJ, 760, 6

Magnelli, B., Elbaz, D., Chary, R. R., et al. 2011, Evolution of the dusty infrared luminosity function from $z = 0$ to $z = 2.3$ using observations from Spitzer, A&A, 528, A35

Magnelli, B., Popesso, P., Berta, S., et al. 2013, The deepest Herschel-PACS far-infrared survey: number counts and infrared luminosity functions from combined PEP/GOODS-H observations, A&A, 553, A132

Magnelli, B., Lutz, D., Saintonge, A., et al. 2014, The evolution of the dust temperatures of galaxies in the SFR-M plane up to z $\sim$ 2, A&A, 561, A86

Magnelli, B., Ivison, R. J., Lutz, D., et al. 2015, The far-infrared/radio correlation and radio spectral index of galaxies in the SFR-M plane up to z$\sim$2, A&A, 573, A45

Mauch, T., Klöckner, H.-R., Rawlings, S., et al. 2013, A 325-MHz GMRT survey of the Herschel-ATLAS/GAMA fields, MNRAS, 435, 650

McCracken, H. J., Milvang-Jensen, B., Dunlop, J., et al. 2012, UltraVISTA: a new ultra-deep near-infrared survey in COSMOS, A&A, 544, A156

Moustakas, J., Kennicutt, Jr., R. C., & Tremonti, C. A. 2006, Optical Star Formation Rate Indicators, ApJ, 642, 775

Murphy, E. J. 2009, The Far-Infrared-Radio Correlation at High Redshifts: Physical Considerations and Prospects for the Square Kilometer Array, ApJ, 706, 482

Murphy, E. J., Chary, R.-R., Alexander, D. M., et al. 2009, Balancing the Energy Budget Between Star Formation and Active Galactic Nuclei in High-Redshift Infrared Luminous Galaxies, ApJ, 698, 1380

Murphy, E. J., Helou, G., Kenney, J. D. P., Armus, L., & Braun, R. 2008, Connecting Far-Infrared and Radio Morphologies of Disk Galaxies: Cosmic-Ray Electron Diffusion After Star Formation Episodes, ApJ, 678, 828

Murphy, E. J., Condon, J. J., Schinnerer, E., et al. 2011, Calibrating Extinction-free Star Formation Rate Diagnostics with 33 GHz Free-free Emission in NGC 6946, ApJ, 737, 67

Murphy, E. J., Baum, S. A., Brandt, W. N., et al. 2015, in American Astronomical Society Meeting Abstracts, Vol. 225, American Astronomical Society Meeting Abstracts, 113.03

Noeske, K. G., Weiner, B. J., Faber, S. M., et al. 2007, Star Formation in AEGIS Field Galaxies since z=1.1: The Dominance of Gradually Declining Star Formation, and the Main Sequence of Star-forming Galaxies, ApJ, 660, L43

Norris, R., Basu, K., Brown, M., et al. 2015, The SKA Mid-frequency All-sky Continuum Survey: Discovering the unexpected and transforming radio-astronomy, Advancing Astrophysics with the Square Kilometre Array (AASKA14), 86

Oesch, P. A., Brammer, G., van Dokkum, P. G., et al. 2016, A Remarkably Luminous Galaxy at z=11.1 Measured with Hubble Space Telescope Grism Spectroscopy, ApJ, 819, 129

Oke, J. B. 1974, Absolute Spectral Energy Distributions for White Dwarfs, ApJS, 27, 21

Padovani, P., Bonzini, M., Kellermann, K. I., et al. 2015, Radio-faint AGN: a tale of two populations, MNRAS, 452, 1263

Pannella, M., Elbaz, D., Daddi, E., et al. 2015, GOODS-Herschel: Star Formation, Dust Attenuation, and the FIR-radio Correlation on the Main Sequence of Star-forming Galaxies up to z∼4, ApJ, 807, 141

Papovich, C., Rudnick, G., Le Floc'h, E., et al. 2007, Spitzer Mid- to Far-Infrared Flux Densities of Distant Galaxies, ApJ, 668, 45

Peacock, J. A. 1999, Cosmological Physics, 704

Peebles, P. J. E., & Turner, E. C. 1992, Big Bang contd.. ., Nature, 357, 288

Polletta, M., Tajer, M., Maraschi, L., et al. 2007, Spectral Energy Distributions of Hard X-Ray Selected Active Galactic Nuclei in the XMM-Newton Medium Deep Survey, ApJ, 663, 81

Reddy, N. A., Kriek, M., Shapley, A. E., et al. 2015, The MOSDEF Survey: Measurements of Balmer Decrements and the Dust Attenuation Curve at Redshifts z $\sim$ 1.4-2.6, ApJ, 806, 259

Rieke, G. H., Alonso-Herrero, A., Weiner, B. J., et al. 2009, Determining Star Formation Rates for Infrared Galaxies, ApJ, 692, 556

Rodighiero, G., Daddi, E., Baronchelli, I., et al. 2011, The Lesser Role of Starbursts in Star Formation at z = 2, ApJ, 739, L40

Sanders, D. B., Salvato, M., Aussel, H., et al. 2007, S-COSMOS: The Spitzer Legacy Survey of the Hubble Space Telescope ACS 2 deg^2 COSMOS Field I: Survey Strategy and First Analysis, ApJS, 172, 86

Sargent, M. T., Schinnerer, E., Murphy, E., et al. 2010, The VLA-COSMOS Perspective on the Infrared-Radio Relation. I. New Constraints on Selection Biases and the Non-Evolution of the Infrared/Radio Properties of Star-Forming and Active Galactic Nucleus Galaxies at Intermediate and High Redshift, ApJS, 186, 341

Schawinski, K., Urry, C. M., Simmons, B. D., et al. 2014, The green valley is a red herring: Galaxy Zoo reveals two evolutionary pathways towards quenching of star formation in early- and late-type galaxies, MNRAS, 440, 889

Schinnerer, E., Carilli, C. L., Scoville, N. Z., et al. 2004, The VLA-COSMOS Survey. I. Radio Identifications from the Pilot Project, AJ, 128, 1974

Schinnerer, E., Smolčić, V., Carilli, C. L., et al. 2007, The VLA-COSMOS Survey. II. Source Catalog of the Large Project, ApJS, 172, 46

Schinnerer, E., Sargent, M. T., Bondi, M., et al. 2010, The VLA-COSMOS Survey. IV. Deep Data and Joint Catalog, ApJS, 188, 384

Scott, K. S., Austermann, J. E., Perera, T. A., et al. 2008, AzTEC millimetre survey of the COSMOS field - I. Data reduction and source catalogue, MNRAS, 385, 2225

Scoville, N., Abraham, R. G., Aussel, H., et al. 2007a, COSMOS: Hubble Space Telescope Observations, ApJS, 172, 38

Scoville, N., Aussel, H., Brusa, M., et al. 2007b, The Cosmic Evolution Survey (COSMOS): Overview, ApJS, 172, 1

Sibthorpe, B., Helmich, F., Roelfsema, P., Kaneda, H., & Shibai, H. 2016, in EAS Publications Series, Vol. 75, EAS Publications Series, 411–417

Smith, J. D. T., Draine, B. T., Dale, D. A., et al. 2007, The Mid-Infrared Spectrum of Star-forming Galaxies: Global Properties of Polycyclic Aromatic Hydrocarbon Emission, ApJ, 656, 770

Smolčić, V., Schinnerer, E., Scodeggio, M., et al. 2008, A New Method to Separate Star-forming from AGN Galaxies at Intermediate Redshift: The Submillijansky Radio Population in the VLA-COSMOS Survey, ApJS, 177, 14

Smolčić, V., Ciliegi, P., Jelić, V., et al. 2014, The VLA-COSMOS Survey - V. 324 MHz continuum observations, MNRAS, 443, 2590

Springel, V., Frenk, C. S., & White, S. D. M. 2006, The large-scale structure of the Universe, Nature, 440, 1137

Springel, V., White, S. D. M., Jenkins, A., et al. 2005, Simulations of the formation, evolution and clustering of galaxies and quasars, Nature, 435, 629

Stark, D. P., Ellis, R. S., Bunker, A., et al. 2009, The Evolutionary History of Lyman Break Galaxies Between Redshift 4 and 6: Observing Successive Generations of Massive Galaxies in Formation, ApJ, 697, 1493

Swarup, G., Ananthakrishnan, S., Kapahi, V. K., et al. 1991, The Giant Metre-Wave Radio Telescope, Current Science, Vol. 60, NO.2/JAN25, P. 95, 1991, 60, 95

Tabatabaei, F. S., Schinnerer, E., Murphy, E. J., et al. 2013, A detailed study of the radio-FIR correlation in NGC 6946 with Herschel-PACS/SPIRE from KINGFISH, A&A, 552, A19

Taniguchi, Y., Scoville, N., Murayama, T., et al. 2007, The Cosmic Evolution Survey (COSMOS): Subaru Observations of the HST Cosmos Field, ApJS, 172, 9

Tasse, C., Röttgering, H. J. A., Best, P. N., et al. 2007, GMRT observations of the XMM large scale structure survey field, A&A, 471, 1105

Trump, J. R., Impey, C. D., McCarthy, P. J., et al. 2007, Magellan Spectroscopy of AGN Candidates in the COSMOS Field, ApJS, 172, 383

Urry, C. M., & Padovani, P. 1995, Unified Schemes for Radio-Loud Active Galactic Nuclei, PASP, 107, 803

Whitaker, K. E., van Dokkum, P. G., Brammer, G., & Franx, M. 2012, The Star Formation Mass Sequence Out to z = 2.5, ApJ, 754, L29

White, S. D. M., & Rees, M. J. 1978, Core condensation in heavy halos - A two-stage theory for galaxy formation and clustering, MNRAS, 183, 341

Wilman, R. J., Miller, L., Jarvis, M. J., et al. 2008, A semi-empirical simulation of the extragalactic radio continuum sky for next generation radio telescopes, MNRAS, 388, 1335

Wuyts, S., Labbé, I., Förster Schreiber, N. M., et al. 2008, FIREWORKS U_{38}-to-24 μm Photometry of the GOODS Chandra Deep Field-South: Multiwavelength Catalog and Total Infrared Properties of Distant K_s-selected Galaxies, ApJ, 682, 985

York, D. G., Adelman, J., Anderson, Jr., J. E., et al. 2000, The Sloan Digital Sky Survey: Technical Summary, AJ, 120, 1579

Yun, M. S., Reddy, N. A., & Condon, J. J. 2001, Radio Properties of Infrared-selected Galaxies in the IRAS 2 Jy Sample, ApJ, 554, 803

Zamojski, M. A., Schiminovich, D., Rich, R. M., et al. 2007, Deep GALEX Imaging of the COSMOS HST Field: A First Look at the Morphology of z $\sim$ 0.7 Star-forming Galaxies, ApJS, 172, 468

Acknowledgements

This thesis would not have been possible without the support and supervision of Eva Schinnerer and Brent Groves - thank you for all your time and patience over the last three years! I also would like to thank Hans-Walter Rix and Simon Glover for agreeing to referee this thesis and Eva Grebel and Luca Amendola for making the time to join the doctoral exam committee.

Many others contributed to the work presented here; in particular thanks must go to Hans-Rainer Kloeckner for sharing his GMRT calibration pipeline with me and answering all my many data calibration questions. Thanks to Alex Karim, Vernesa Smolčić, Mark Sargent and Ben Magnelli for many fruitful discussions. I'm also grateful for Mladen Novak, Vernesa Smolčić and Nikolai Baran's sharing of early data and results relating to the 3 GHz COSMOS catalogue, as well as for Marco Bondi for providing flux measurements for some of my sources. Thank you also to the many members of the COSMOS collaboration whose contributions, particularly regarding data products, made this thesis possible.

To my friends in Heidelberg for making this place feel more like home and putting up with me these last few months: Anders, Caroline, Taisiya, Paolo, Julia, Sasa, Rich, Melanie, Christina, Ilya, Miguel, Michael, Sarah, Simon.....There are too many people to name here - I hope everyone else can forgive me the omission!

I'm forever grateful for the support of my family, I could not possibly have gotten this far without them.